REDOX-ACTIVE POLYMERS AS CATHODE MATERIALS FOR ENERGY STORAGE APPLICATIONS

A Dissertation

Presented to the Faculty of the Graduate School

of Cornell University

In Partial Fulfillment of the Requirements for the Degree of

Doctor of Philosophy

by

Luxi Shen

August 2018

REDOX-ACTIVE ORGANIC AND POLYMERIC CATHODES MATERIALS AS CATHODES FOR ELECTRICAL ENERGY STORAGE (EES) APPLICATIONS

Luxi Shen, Ph. D.

Cornell University 2018

Organic and polymeric electrodes have great properties and tenability enabling them to become high-energy and high-power cathode materials for electrical energy storage(EES) applications. Two main classes of polymeric materials were explored, investigated, and evaluated as promising electrodes for EES applications: thin-film and bulk polymers. In the first half of this dissertation, I studied, in detail, the electrosynthesis of a library of polypyrrole anchored redox-active pendant decorated thin-film polymers. The polymer architecture was designed to boost electronic conductivity of the polymer by installing a conducting polymer as backbone, and energy density was maximized by employing highly reversible redox-active moieties including 1,4-dimethoxybenzene (DMB), *N,N,N',N'*-tetramethylphenylenediaine (TMPD). By having two stable redox couples at high potentials, PPy-5C-TMPD was shown to have the most promising electrochemical properties, amongst the molecules studied. However, this thin-film polymer exhibited severe charge trapping behavior, in which half of the capacity was missing during reduction of the polymer, as if anions (or charges) were "trapped" inside the polymer film. This so-called "charge trapping" phenomenon was studied in detail to unravel its origin, and results indicated that the phenomenon appears to be specific to TMPD as a redox-active pendant. Substitution of the redox-active pendant to equally high-energy 5,5'-bis(methylthio)-2,2'-bithiophene (BMTbT) resulted in no signs of charge trapping.

I then explored bulk polymer materials, by coupling redox-active moieties in alternating fashion by Buchwald-Hartwig coupling to form main-chain redox-active polymers. By coupling phenothiazine with *N,N'*-dimethylphenylenediamine (PT-DMPD), the resulting polymers showed three main redox couples. EQCM and other mechanistic studies suggested that the redox activities of PT-DMPD involved the exchange of three electrons. As battery material, two of the redox processes could be accessed. Initial cycling performance of PT-DMPD showed capacity fade likely due to polymer dissolution. Cross-linking of PT units by a butyl alkyl linker enabled different degrees of cross-linked polymers to be prepared. Upon optimization, 10%CL PT-DMPD showed the best performance, reaching close to 100 % of its theoretical capacity. An impressive rate performance was also achieved with this material, reaching 120 C with 82 % capacity retention, an unprecedented rate performance among organic materials. These studies on organic electrode materials have demonstrated promising electrochemical properties of these materials for EES applications, and device level testing suggested potentials for practical application. Using these results as a part of motivation, future researchers should focus on better design while maintaining chemical stability of the polymers, and perhaps aided by our studies, find better performing organic materials for EES application.

BIOGRAPHICAL SKETCH

Luxi Shen was born in the city of Guangzhou, Guangdong, China, where she spent the first fifteen years of her life. After middle school, she then followed her father to Jakarta, Indonesia in 2005, where she went to high school at Jakarta International school. Luxi continued her higher education at the University of Rochester from 2009 to 2013, and studied chemistry and brain and cognitive sciences in her undergraduate studies. During that time, she studied inorganic synthetic chemistry with Dr. Zhiji Han under the supervision of Prof. Richard Eisenberg for two years. A class of ten nickel thiolato complexes were synthesized, characterized, and evaluated as catalysts for photocatalytic proton reduction.

After a dab at synthetic inorganic chemistry, Luxi continued to pursue chemistry in her graduate career two hours away from Rochester at Cornell University in 2013. Coming from a relatively synthetic background, she made the switch to electrochemistry in the Abruña group and spent the next five years studying organic electrode materials for EES applications.

This work is, above all, dedicated to my origins.

ACKNOWLEDGMENTS

At each finish line, we always celebrate the people that we encountered throughout the journey. To my parents, you have always been my biggest cheerleaders in every sense of the word, and you will always be there for me at every finish line. Everything I do is to make you proud, and I hope that you are. Often standing in for my parents is my second biggest cheerleader, Kenny. You often praise that I am good at this I am good at that, and that is what I have been trying to achieve. Better.

Such a daunting journey needs coaches to guide us along the way, and I have been fortunate to have them to steer me through thick and thin. To Prof. Héctor Abruña, you put me onto tasks that I was not sure if I could complete and succeed; then times and times again, it has proven that even when I was not sure, you were. Call it "unconditional trust". My deepest gratitude for all of your patience and trust over the past five enduring years. To my committee members, Prof. Geoffrey Coates, Prof. Brett Fors and Prof. William Dichtel (Northwestern University), it was my greatest honor to have worked with you and your talented groups. Never will I forgive a faulty reference or a misaligned figure in the future. To my undergraduate advisor, Prof. Richard Eisenberg, you opened my eyes to the reality and wonders of chemistry and for giving me an opportunity, when no one else did.

No quest is completed without the teammates, and throughout my graduate career, I have had many great teammates. To Dr. Masato Mizutani, you are my first collaborator and one of my best polymer suppliers; there was so much that I learned from our interactions. To Dr. Catherine Mulzer, the most impatient "customer" and the one who would never take no for an answer; you kept me on my toes about my progress. And it turns out, it only takes two chemists to turn on a light bulb. To Brian Peterson, my longest polymer supplier, thank you for your patience; as you learned over the years, we work slowly, but hopefully, we compensate in quality. Finally, to

my longest collaborator, friend, and classmate during this race, Dr. Dong Ren. Our collaborations have gone well over the years, and let us continue working together to achieve greater goals.

For the people whom I have the pleasure of encountering and accompanying, my fellow classmates, my lab-mates, my bench-mates, my office-mates, time passes just a tad faster with a dash of sunshine in the physical sciences building because of all of you. Working is not just tedious work and chores because of your presence, and I wish that the sunshine in the physical sciences building will continue to accompany your work in the future.

The conclusion of a five-year journey implies the start of my adult life journey, which is a transition that I did not expect to be as significant as it turned out to be. For some, this transition is as natural as graduation and going into the next level of study. For some, it is the liberation of all of their potential and ambition. And for some, it tested our profession, belief, and personality in us, and coming out of this transition, we shed a layer of skin and emerge with a deepened personal perspective. A difficult transition it may be, but a difficult time is always accompanied with eventual lift, and that it is a coat of gold that we emerge with and start to shine.

TABLE OF CONTENTS

LIST OF FIGURES

LIST OF TABLES

LIST OF SCHEMES

PREFACE

Five years is not a long time; it is only half a decade and a small fraction of our expected life. But at the same time, five years is not a short time; it is enough time to build our customized scientific foundation, structure, and personality to our professional future. At the intersection of student and adult, we have passed beyond the years of searching for who we are, and the purpose of these five years are particularly special and precious; we know who we are, and this is the time to make ourselves really good at it. At the top of each graduate student's career, we start the countdown of ten thousand hours[i] to become the expert in an area in chemistry.

This is, regardless, an enduring journey, and I find this journey divided itself into legs much like the way a triathlon race would. We first dabble and most likely struggle in the first leg of the race, swimming, because no matter how well prepared we thought we were, it would never prepare us for the initial shock. As we struggle and catch the rhythm of the waves and research, the second leg of the race, cycling, is the most important one, where lots of advantages can be gained or lost during this time. It is supposed to be our strongest leg because it is also the longest leg in the journey; as a scientist, this is research – what we are trained to do. The best case scenario is that if we can be keep a consistent pace for the duration, continuing to learn while doing research, and keeping pace at getting results. As we hit the last leg of the race, most of us are bound to be tired, because we have been pushing hard for a while, but here is the real test of the race: focus. During the last leg, focus of mind, strong will, and diligent planning are all required, in addition to endurance. Much of the same case, other tasks start to set in at the end of our five-year journey, e.g. job search, relocation, degree completion. A successful completion of the Ph.D. degree parallels

[i] A sample calculation by Prof. Brad Nilsson at the University of Rochester; assume 8 working hours a day, 250 days a year, it takes about 5 year (10,000 hrs) to get a Ph.D., a.k.a., become the expert in something.

the completion of such a race, as it requires *a stoic mind*, *a strong body*, and *a strategic plan*. Such, is a small piece of advice, if I may so humbly give to anyone who is about to embark on this unpredictable yet tremendously rewarding experience.

May 12th, 2018

CHAPTER 1

INTRODUCTION TO ORGANIC AND POLYMERIC ELECTRODES FOR ELECTROCHEMICAL ENERGY STORAGE SYSTEMS

1-1. Global Shift in Energy Paradigm

The moment we entered the 21st century, we were confronted with an exciting yet challenging situation; world economies are enjoying the prosperity of technological and industrial development but at the same time, are putting more demands and strains on energy. Global energy demands are expected to rise by 28 % from 575 to 736 quadrillion British Thermal Units (Btu) from year the 2015 to 2040 (Figure 1-1a), with the growing/developing economies accounting for the majority and the faster growing party, compared to the developed economies.[1, 2] Confronted with a fast growing population, developing industry and innovating transportation (Figure 1-1b), the international community is faced with one of the biggest challenges of its time: how to meet this energy demand sustainably. Over the past two decades, we, as a global community, have been striving to reduce our carbon footprint by gradually phasing out carbon-intensive energy sources such as coal and oil while drastically propelling the development and implementation of less carbon-intensive sources, such as natural gas, and carbon-neutral, renewable sources. As a result, total energy consumption has been experiencing a steady increase over all energy sources, with a spur in renewable energy sources and with natural gas taking an increasingly larger role in helping to meet energy needs in an environmentally sustainable way (Figure 1-1c).

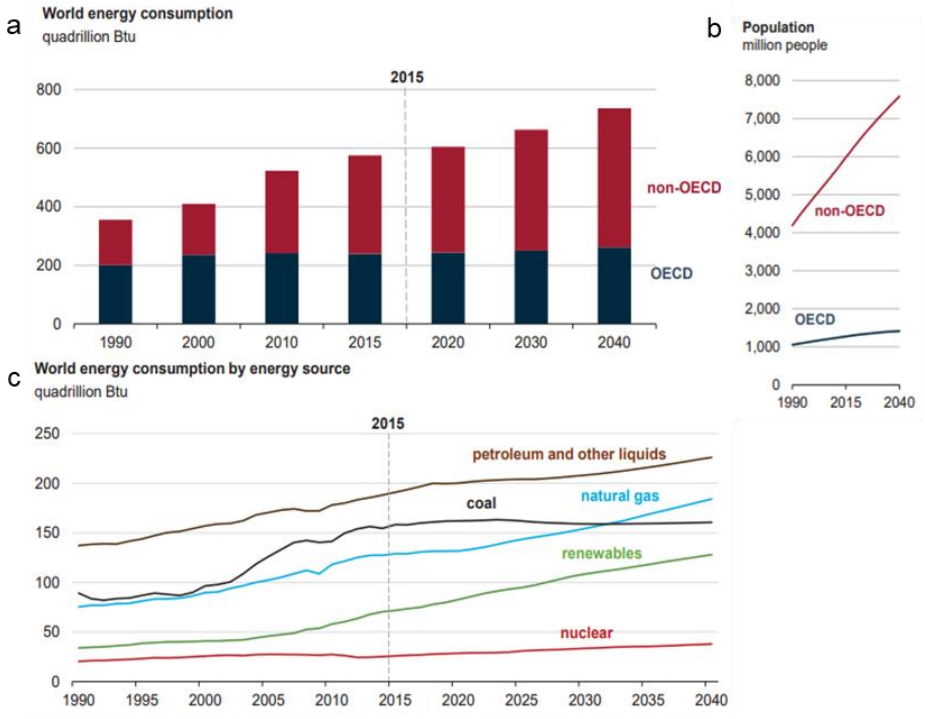

Figure 1-1. a) World energy consumption record and projection from 1990 to 2040. OECD: organization for economic cooperation and development (OECD) and nonmembers (non-OECD). b) World population record and projection from 1990 to 2040. c) World energy consumption record and projection by energy source from 1990 to 2040. Figures copied from U.S. Energy Information Administration from reference 1 and 2.

A key strategy to further the agenda of global sustainability is electrification: replacing power driven from carbon-intensive energy sources with electricity. In addition, currently, natural gas and coal account for close to 60 % of the total electricity generation globally, and to further reduce their contribution, renewable energy sources have to grow significantly (Figure 1-2).[1] Among renewable sources, solar and wind will likely grow significantly over the next twenty-five years to undertake hydropower as the primary renewable sources for electricity generation (Figure 1-2b).[1] To be able to support renewable sources, through the transition from carbon-intensive period into a sustainable future, robust energy storage system and materials will play an instrumental role in this transition and well into the future.

For different scales sizes of applications, electrical/electrochemical energy storage systems (EESS) are being developed for maximum benefit (Figure 1-3).[3] For example, at the largest scale, EESS can significantly improve the electrical grid system by decoupling energy production from consumption, leading to the fulfillment of peak and low demands by simply powering on and off the energy storage systems.[3] Redox-flow batteries and lithium-ion batteries have been recognized as some of the most promising EESS for grid-leveling applications, and many commercial systems are near production and implementation.[4, 5] Much effort has also been focus on at medium scale applications; the transportation sector is rapidly innovating hybrid power and all electrical power vehicles (EV) to greatly reduce petroleum as the sole fuel to realize this global effort. Compact energy conversion systems like fuel cells (as an energy conversion device) and rechargeable battery technologies are quickly becoming the favorites for this application, as they have high volumetric and

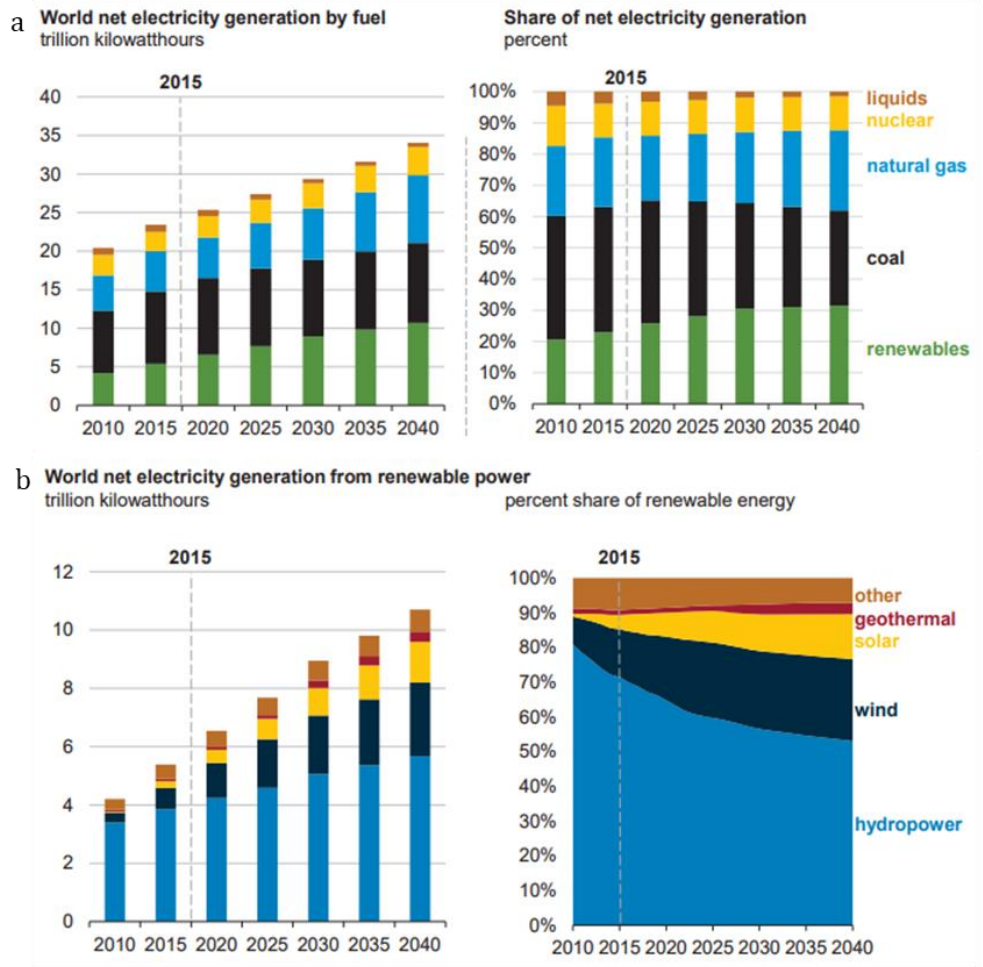

Figure 1-2. a) World net electricity generation and share of by fuel sources. b) World net electricity generation and share of by renewable power. Figures copied from U.S. Energy Information Administration from reference 1 and 2.

gravimetric energy densities, two of the most important criteria for transportation.[6] These EESS are also being applied to smaller, but equally energy-intensive, systems such as laptops, mobile phones and fitness trackers/watches, with some powered by electrochemical capacitors.[7]

1-2. Compact Lithium-ion Batteries and Inorganic Cathodes

Compact rechargeable energy storage systems are under intense development due to the high demand for stable EESS and their environmental friendliness. Older EESS such as lead-acid batteries, nickel-cadmium and nickel-metal hydride systems have been studied, developed and commercialized into mature technologies (Figure 1-4).[3] However, to further increase their energy densities, lithium and especially lithium-ion batteries were developed in the 70s through the 90s and showed great promise for high-energy density portable applications.[8-11] Amongst these devices, lithium-ion batteries are the most popular choice for these applications (Figure 1-4) as they currently have the highest volumetric and gravimetric energy densities amongst the commercial rechargeable electrical energy storage devices.[3] Although initially they were costly, as the technology developed, the cost of lithium-ion battery has dropped to less than $268/kWh in 2015, on track to reach the goal of $125/kWh by 2020, based on current projections.[12-14] As a result, lithium-ion batteries have ample momentum to maximize development and reach proposed goals.

During the development of lithium-ion batteries, advances in inorganic cathode materials for improving their overall performance deserve recognition. Commercial lithium-ion battery cathode materials have evolved from the benchmark lithium cobalt

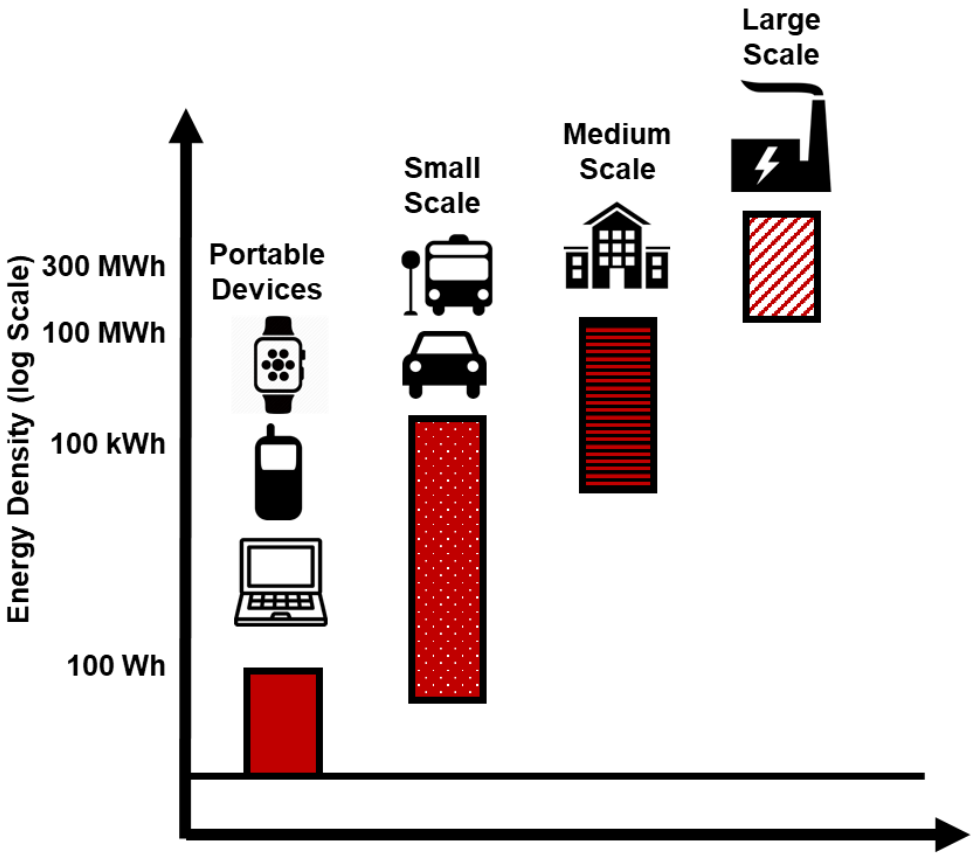

Figure 1-3. Energy densities of energy storage devices at various scales. Data taken from reference 3 and symbols taken from google.com.

oxide ($LiCoO_2$) and lithium iron phosphate ($LiFePO_4$) to mixed metal materials such as lithium nickel manganese cobalt oxide ($LiNi_{0.33}Mn_{0.33}Co_{0.33}O_2$, NMC) and lithium nickel cobalt aluminum oxide ($LiNi_{0.8}Co_{0.15}Al_{0.05}O_2$, NCA) to enhance their capacity.[15] From $LiCoO_2$ to NMC and NCA materials, we witnessed improvements from 150 mAh/g to 200 mAh/g with a 0.3 V voltage improvement (Figure 1-5).[15] These commercial materials with excellent electrochemical properties have provided great advantages as lithium-ion battery cathodes.

However, lithium-ion batteries still face significant challenges. First, cost is a major component and limitation preventing the grid-scale implementation of lithium-ion batteries. Based on cost analysis,[13] out of a $249/kWh lithium-ion cell, the cathode component is still the biggest component, accounting for $82 out of the total cost. The cost of the metals used in the cathode material, mainly cobalt, is the main source of the high costs, and based on current trends, the price of cobalt could continue to surge.[13] To be able to widely implement lithium-ion batteries, especially for grid-scale or EV applications, cost remains an important hurdle.

Secondly, commercial lithium-ion batteries generally operate at charge rates of 0.5 – 1 C. [16, 17] For EV and other future developments, a faster charging rate would represent an enabling advantage. This limitation in charging rates is mostly due to the intercalation process in both cathode and anodes, as solid-state diffusion coefficients are typically in the 10^{-10} – 10^{-12} cm^2/s regime. Slow lithium insertion and desertion processes represent one of the main limitations.

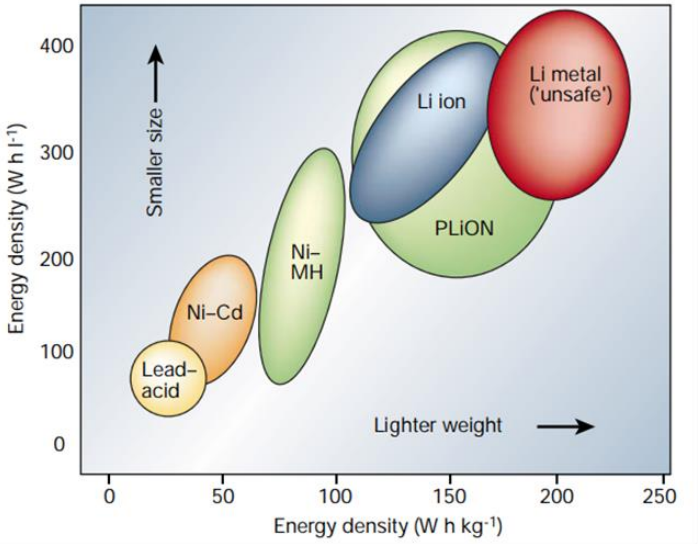

Figure 1-4. Volumetric and gravimetric comparison of the different battery technologies. Reproduced from reference 8, reprinted with permission, copyright 2001, Spring Nature.

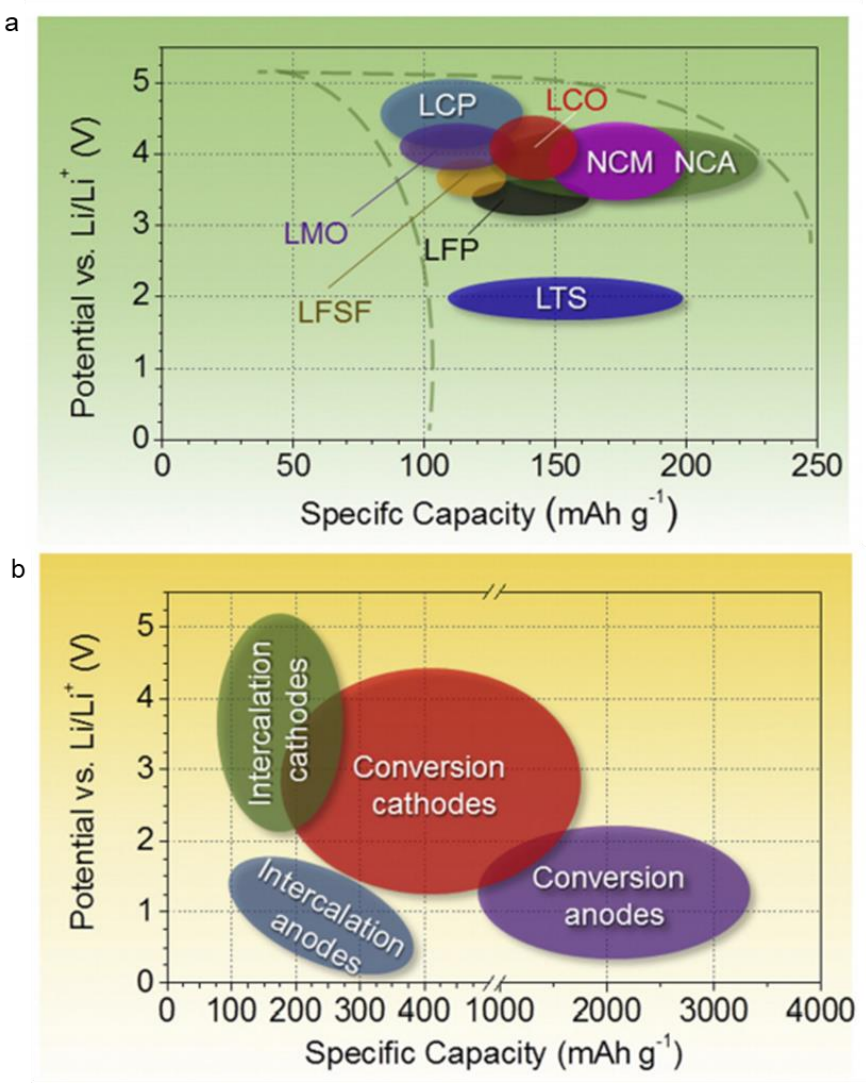

Figure 1-5. a) Comparison of intercalation cathodes in terms of working potentials and specific capacities. b) Comparison of working potentials and specific capacities for intercalation and conversion materials. Reproduced from reference 14, reprinted with permission, copyright 2015, Elsevier Ltd.

Finally, some of the most promising current commercial lithium-ion battery cathodes are NMC and NCA materials. However, their capacities caps at ca. 200 mAh/g, and they are reaching their limit in terms of energy density. High working voltages generally cause problems with solvents and electrolytes, and higher capacities imply the synthesis of less chemically stable oxides, that might lead to a higher degree of degradation (Figure 1-5).

Based on the limitation exhibited by inorganic materials, there is a need to develop materials that can: 1) exhibit high capacities (> 200 mAh/g); 2) operate at higher C-rates, and 3) compose of earth abundant elements. While we acknowledge that sulfur is be a great cathode candidate and that lithium-sulfur batteries have great promise for high-energy applications.[18-20] They do not satisfy our high-rate performance needs. We then turned our attention to organic and polymeric materials to identify promising candidates that can overcome of inorganic cathodes.

1-3. Organic and Polymeric Materials for Energy Storage Systems and Benchmarks

Organic and polymeric materials[ii] have been studied as electrode materials for various EESS. Organic materials are inherently lightweight, leading to high gravimetric densities, which is a valuable attribute for an electrode material. However, the significantly lower volumetric densities of organic materials represent an unfavorable aspect, as high gravimetric and volumetric densities are essential for compact energy storage systems. In addition, organic materials are generally more prone to chemical degradation when subject to long cycling, making them less stable

[ii] "Organic and polymeric materials" will be termed as "organic materials" from here on; for the context of this dissertation, the term "organic" will automatically include "polymeric" for the sake of simplicity.

than inorganic oxides. These disadvantages have made organic materials less attractive as electrode for EESS applications. [iii]

While there are fundamental physical properties that are intrinsic to nonmetals, organic and polymeric materials excel in the three areas where inorganic materials for EESS applications prove inadequate. For example, cost is not an issue for organic materials, as they are composed of earth-abundant elements such as carbon, oxygen, nitrogen, hydrogen and sulfur. Even with the additional processing cost, organic materials still have a cost advantage over inorganic materials, while lowering their environmental impact. Another advantage of organic polymeric materials is their broad tunability enabled by the use of different functional groups in the backbone or the repeating motive. This allows us to maximize the number of electrons exchanged and tune the theoretical capacity. Finally, most organic materials are generally amorphous so that ion diffusion is generally facile.[21] As a result, very high power densities can be obtained in organic materials, as in one of the materials discussed in Chapter 5 of this dissertation.

These unique properties provide organic materials with their own set of advantages over inorganic materials, and have spurred research and development over the past few decades. One of the early organic materials for EESS was dichloroisocyanuric acid (DCA) was employed as a cathode in lithium batteries.[22] A solid-state electrode of DCA exhibited an open-circuit voltage (OCV) of 4.0 V vs. Li/Li^{+}, a highly promising working voltage for a cathode in lithium batteries.

[iii] In this dissertation, we do not explicitly compare the energy and power densities of battery devices using inorganic and organic electrodes due to the different methods and standards for testing these materials in devices.

Quinones were found to be suitable for cathode applications as early as 1972,[23] in acidic conditions. The authors showed well-defined charge/discharge plateaus and behaviors for a series of benzoquinone species, demonstrating their applicability as battery cathodes. In 1982, capitalizing on their layered crystalline structure, phthalocyanines were studied as possible intercalation organometallic compounds for lithium-ion batteries, exhibitng high discharge capacities, despite low working voltages.[24] These studies raised the importance and interest in using organic materials as electrodes for EESS.

The discovery of electronically conductng polymers (CPs) in 1977[25] and their subsequent development, indicated the great promise of CPs as electrode materials for EESS (Scheme 1-1). Being electronically conducting, one of the biggest advantages of CPs for EESS is to decrease and potentially eliminate the need for of conducting additives in electrode fabrication, as is often the case when electronically conducting polymers are used as electrode materials.[26] They often exhibit electronic conductivities ranging from 0.10 mS/cm up to 1000 S/cm. For example, as electrode materials, they exhibit discharge capacities between 100 – 200 mAh/g with favorable OCVs (open circuit voltage) often above 3.0 V, and their cyclability generally reaches of cycles. However, despite these promising properties, CPs also have their limitations. The doping process that elicits the dramatic increase in electronic conductivity in CPs is generally low, usually less than 0.2, meaning less than 20 % of the repeating units are oxidized/reduced.[27, 28] The direct consequence of low doping levels is low theoretical and practical capacities. Their unique physical and electrochemical properties have revived the study of CPs in recent years for use in flexible devices, as thin-film and

flexible materials for powering many body-monitoring devices. [29] Scheme 1 shows the redox mechanism and examples of CPs.[30-35]

Many promising organic redox-active materials have been studied over the years.[28, 29, 36, 37] Organo-sulfur materials can exhibit capacities of up to 400 mAh/g. [38-40] By undergoing reduction of sulfur to form polysulfides and eventually to lithium sulfides, the more polysulfide groups that can be incorporated, the higher the theoretical capacity. As a result, given the low molecular weights of organic functionalities, ultra-high capacities can be achieved. However, these materials also exhibit the drawbacks of polysulfides, especially high solubility in organic solvents, resulting in rapid capacity fade during cycling. In addition, they also generally exhibit the poor charge kinetics typical of sulfur materials, significantly lowering working voltages. Scheme 1-2 shows the redox mechanism and a list of examples of some organosulfur compounds studied.[41-45]

Another interesting organic redox-active group is the carbonyl/quinone moiety, which remain as one of the most popular ones in EESS applications. Quinones (Q) differ from many redox-active moieties such as 2,2,6,6-Tetramethyl piperidinyl-1-oxy TEMPO and ferrocene (Fc) in terms of their redox chemistry. While TEMPO and Fc undergo oxidation and are considered "*p-type"* or oxidative, Qs and anthraquinones (AQs) undergo reduction and are called "*n-type"* or reductive materials. [36, 37] Two direct consequences of this difference are: 1) lower working voltages as they undergo reductions rather than oxidations, and 2) involvement of lithium ion (Li^+) intercalation. However, as each Q can accommodate two Li^+ per formula unit, Qs and AQs generally have very high capacities, ranging from 200 to up to 600 mAh/g with

acceptable cyclability. The main efforts have gone into raising their working voltages by various methods, while maintaining high capacity and stable cyclability. [46-49] Scheme 1-3 shows the redox mechanism and some of examples of quinone- and anthraquinone-based compounds that have been studied.[47, 50-54]

Organosulfur and quinone moieties are two classes of functionalities that undergo reduction, and as mentioned before, this results in inherently low voltages. Most of the examples shown exhibit working voltages below 3.0 V vs. Li/Li^+, and as energy density scales linearly with working voltages, these materials will have relatively low energy densities. On the other hand, *p-type* organics are redox-active functionalities that inherently undergo oxidations, and as a result, many of *p-type* materials exhibit working voltages above 3.0 V, up to 4.5 – 5.0 V. One of the most studied examples of *p-type* organics is the TEMPO radical, as it is one of the most chemically stable in organic electrodes. However, the low capacity, due to the fact that it can only exchange one electron has limited its development. Other *p-type* functionalities, such as phenylenediamine, carbazole and phenothiazine, have also been studied. These materials generally have working voltages above 3.5 V, and show promising discharge capacities. However, due to the high voltages in their redox process, they suffer from chemical instability and are often limited to 1 – 2 electrons per formula unit. Scheme 1-4 shows the redox mechanism and a list of examples of some of the *p-type* materials studied.[55-59]

More recently, as electrode development for EESS is moving towards materials engineering, many different molecular and material architectures have been adopted for organic redox-active moieties as proof-of-concept. For example, TEMPO

and anthraquinone redox moieties have been incorporated into covalent organic frameworks (COF) to demonstrate EES promise for COF materials.[60] With the ionic channels that porous and crystalline COFs provide, COFs with incorporated quinones have reached a specific capacity of 200 mAh/g and up to 1800 cycles of testing. To address the electronic conductivity indeficiency of COFs, studies have incorporated electronically conducting polymers into the framework to "wire" the redox-active moieties, improving accessibility of COF by 40-fold.[61] These studies demonstrated the importance of materials engineering in enhancing device performance. Scheme 1-5 shows a list of COF materials incorporated with redox-active functionalities.[60, 62, 63]

While these studies have demonstrated great progress and showed that organic materials are promising candidates to have breakthrough improvements on the three deficiencies of inorganic materials, organic materials have rarely demonstrated both high energy density and power density. Many examples and materials were designed to have high capacities by maximizing the number of electrons exchanged, for example high capacity has been demonstrated in many AQ materials and they have shown tremendous chemical stability over extended cycling. On the other hand, electronically conducting polymers are electronically conducting materials, appropriate for high-rate applications.

Scheme 1-1. Redox mechanism of CPs using polypyrrole as an example, and other examples of CPs.

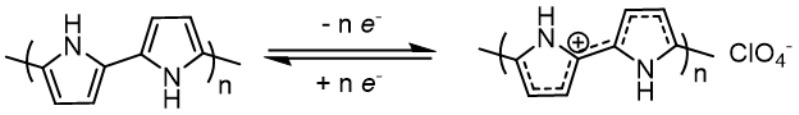

List of Examples of CPs

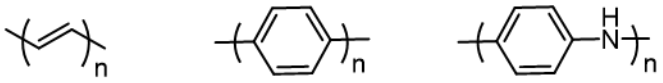

Polyacetylene Poly-*p*-phenylene Polyaniline

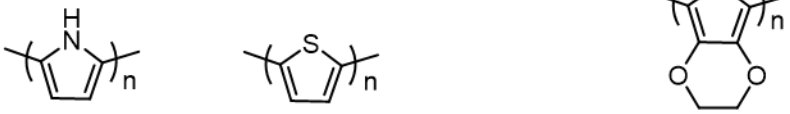

Polypyrrole Polythiophene Poly(3,4-ethylenedioxythiophene)

Scheme 1-2. Redox mechanism of organosulfur compounds using DMcT as an example, and other examples of organosulfur compounds.

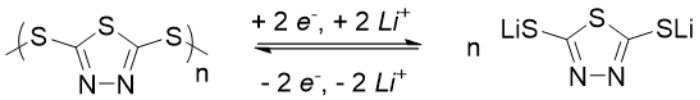

List of Examples of Organosulfur Compounds

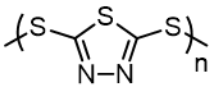

PDMcT

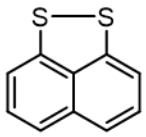

Naphtho[1,8-cd][1,2]dithiol

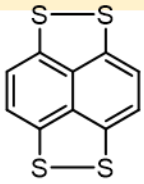

naptho[1,8-cd:4,5-c'd']bis[1,2]dithiol

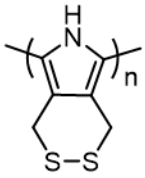

Poly(MPY)

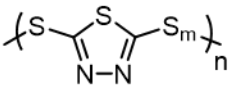

PDMcTS

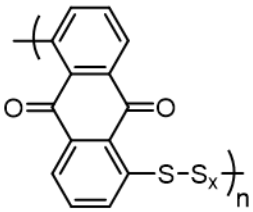

PAQS

Scheme 1-3. Redox mechanism of quinone-moeity compounds using benzoquinone as an example, and other examples of quinone compounds.

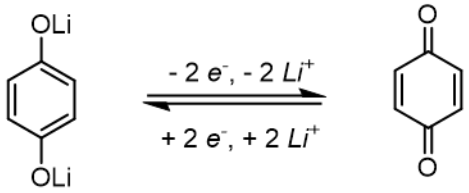

List of Examples of Quinone Compounds

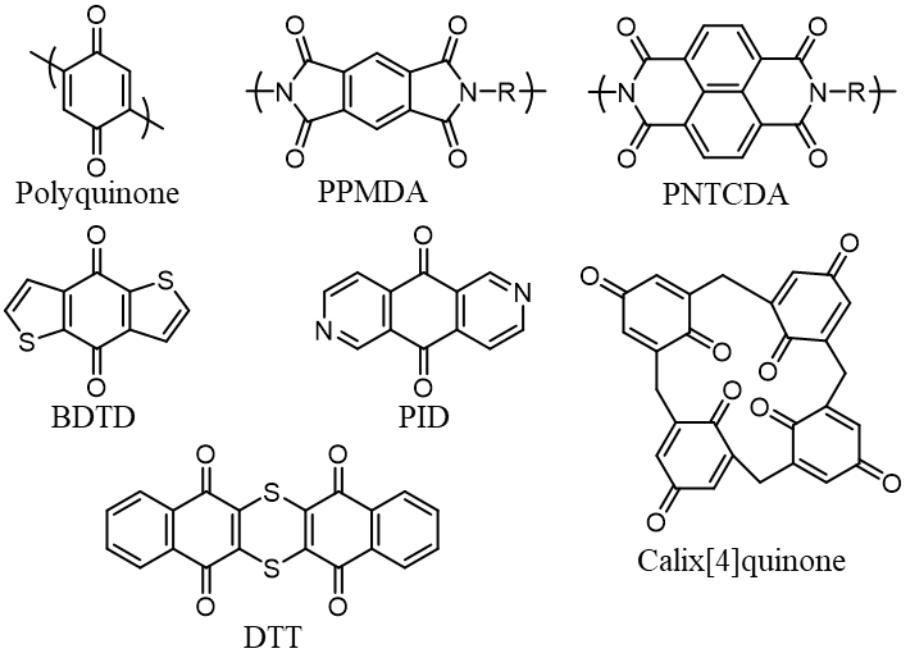

Scheme 1-4. Redox mechanism of *p-type*/oxidative compounds using *N,N,N',N'*-tetramethylphenylenediamine (TMPD) as an example, and other examples of *p-type* compounds.

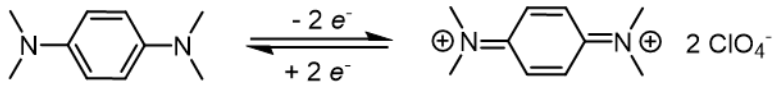

List of Examples of Quinone Compounds

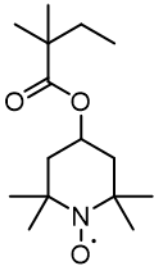

PTMA

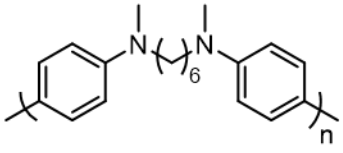

PDA-6

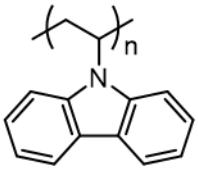

PVK

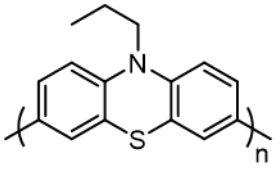

Poly-*N*-propylphenothiazine

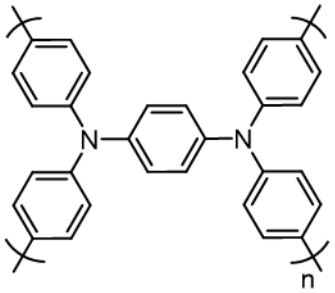

PDDP

Scheme 1-5. List of COFs molecules used for EESS

List of Examples of COFs used for EESS

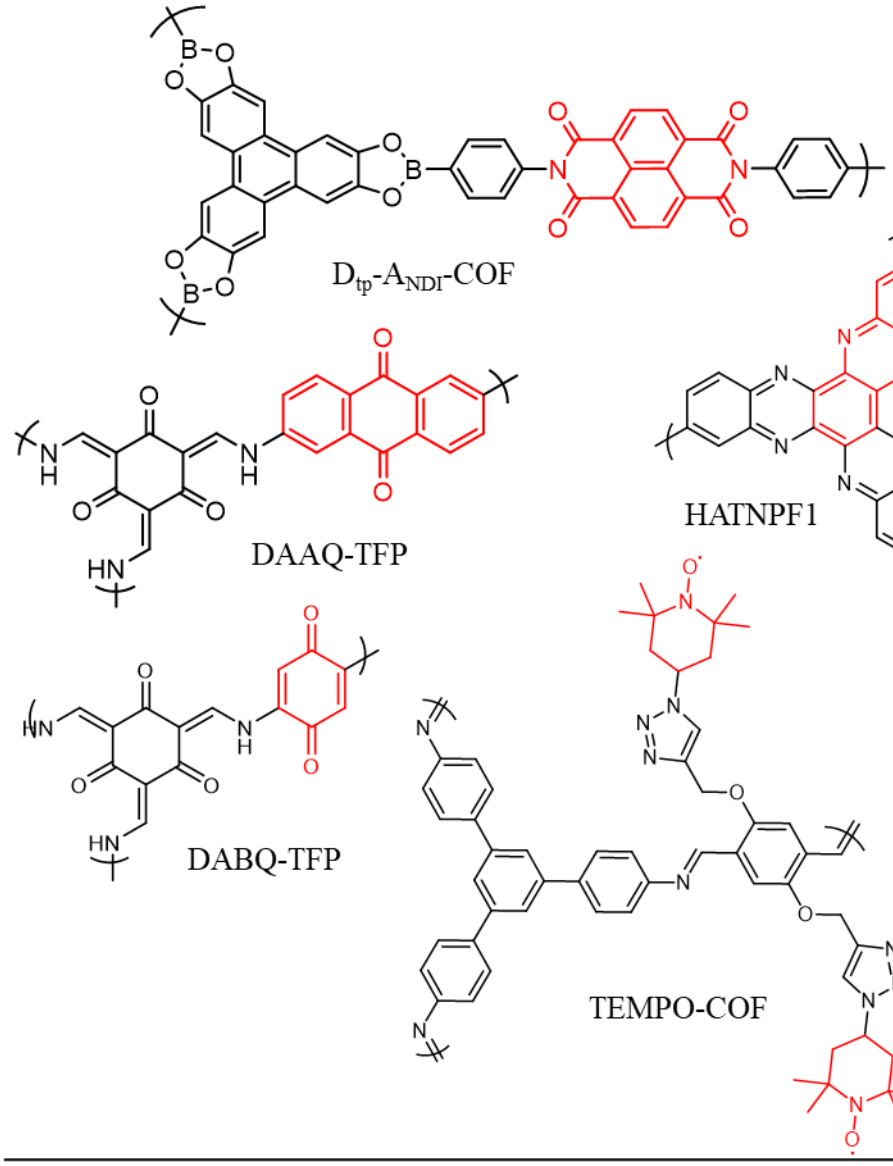

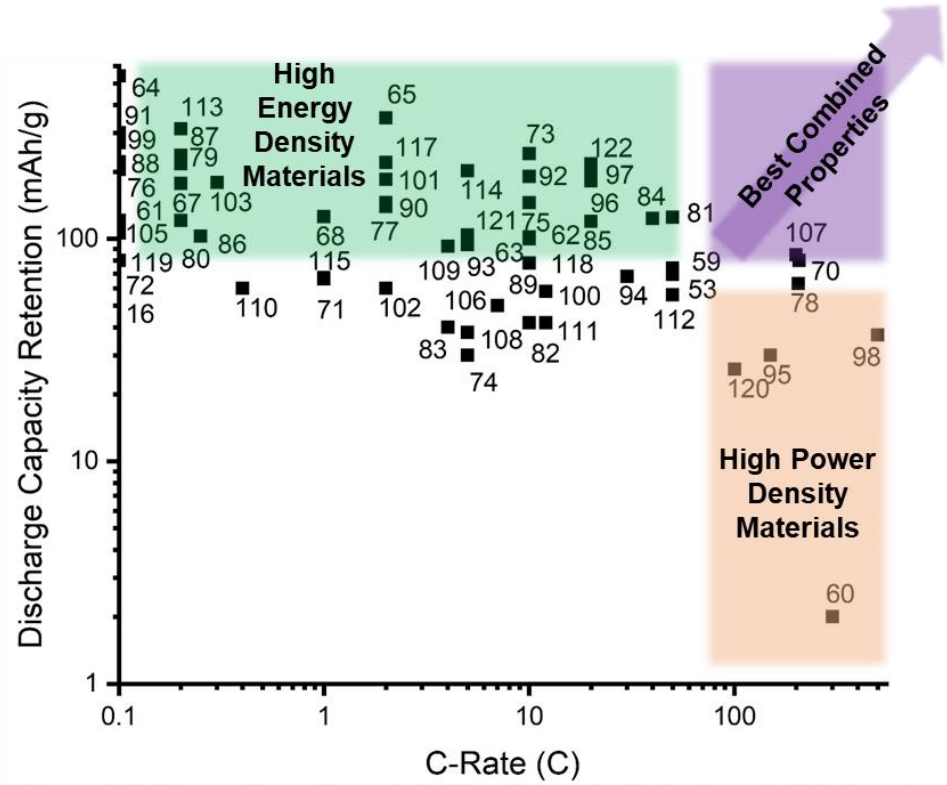

Figure 1-6. Comparison of recent studies of organic electrode materials in terms of energy density and power density. Data taken from reference 53, 59 to 122.

1-4. Focus and Purpose of the Current Study

The current landscape of organic electrodes still promises much exploration and possibilities. Based on the brief survey of the various types of organic materials for EESS, there is ample room for performance improvement (Figure 1-6[58, 64-127]). We can see that while there are a number of materials with high capacity, such as organosulfur and quinone compounds, they lack in working voltages and power density. When we look at *p-type* materials and electronically conducting polymers, they have reasonably good power, but they lack in energy density. With the versatility of organic materials, there still exists a gap between energy and power density. In my graduate work I have sought to explore the broad possibilities that organic materials bring as electrode materials for EESS applications, and focus on improving their *combined performance* by designing novel redox-active moieties and adopting various polymer architectures. The first half of this dissertation focuses on designing flexible materials for battery applications. I will explore the design criteria, electrosynthesis and subsequent redox properties of these thin-film materials in detail. In the second half, I will delve into bulk polymeric materials for batteries By synthesizing the polymers in bulk, I was able to obtain relevant and representative electrochemical performance of polymers at device level, demonstrating practicality of polymers studied.

The focus of this dissertation will be on these compact energy storage systems, namely lithium-ion batteries, and the development of a variety of organic and polymeric electrode materials as cathodes for these systems. In Chapter 3, I will discuss the design, synthesis and characterization of a class of polypyrrole (PPy)

anchored thin-film redox-active polymers as cathodes for lithium-ion batteries. Subsequently in Chapter 4, I will deconvolute the electrochemical responses exhibited by one such thin-film polymer, in detail. In Chapter 5, I will discuss a class of phenothiazine-derivatized redox-active polymers that exhibited promising electrochemical properties for electrochemical energy storage (EES) applications. Subsequently in Chapter 6, I will discuss the electrochemical performance of such polymers in batteries, as they showed unprecedented rate capabilities, one of the highest capacity retention at a given C-rate so far. In Chapter 7, I will briefly discuss the efforts put in to improve the electronic conductivity of covalent organic framework (COF) materials as electrodes for EES application.

REFERENCES

1. U. S. E. I. Administration, *International Energy Outlook 2017*, U.S. Energy Information Administration, www.eia.gov/ieo, 2017.
2. U. S. E. I. Administration, *Annual Energy Outlet 2018 with Projections to 2050*, 2018.
3. S. Sabihuddin, E. A. Kiprakis and M. Mueller, *Energies*, 2015, **8**.
4. Primus Power, http://www.primuspower.com/en/, (accessed March 22, 2018, 2018).
5. Lockheed Martin Energy, https://www.lockheedmartin.com/us/what-we-do/energy/mfc-energy-storage.html#downloads, (accessed March 22, 2018, 2018).
6. M. Winter and R. J. Brodd, *Chemical Reviews*, 2004, **104**, 4245-4270.
7. H. D. Abruña, Y. Kiya and J. C. Henderson, *Phys. Today*, 2008, **61**, 43-47.
8. J. M. Tarascon and M. Armand, *Nature*, 2001, **414**, 359.
9. S. Fletcher, *Bottled lightning: superbatteries, electric cars, and the new lithium economy*, Hill and Wang, 2011.
10. M. S. Whittingham, *Chemical Reviews*, 2004, **104**, 4271-4302.
11. J. Janek and W. G. Zeier, *Nature Energy*, 2016, **1**, 16141.
12. D. Howell, B. Cunningham, T. Duong and P. Faguy, *Journal*, 2016.
13. D. L. Wood, J. Li and C. Daniel, *Journal of Power Sources*, 2015, **275**, 234-242.
14. B. Nykvist and M. Nilsson, *Nature Climate Change*, 2015, **5**, 329.
15. N. Nitta, F. Wu, J. T. Lee and G. Yushin, *Materials Today*, 2015, **18**, 252-264.
16. BU-409: Charging Lithium-ion, http://batteryuniversity.com/learn/article/charging_lithium_ion_batteries, (accessed March 22, 2018, 2018).
17. pinomelean, Lithium-ion battery charging, http://www.instructables.com/id/Li-ion-battery-charging/, (accessed March 22, 2018, 2018).

18. A. Manthiram, Y. Fu, S.-H. Chung, C. Zu and Y.-S. Su, *Chemical Reviews*, 2014, **114**, 11751-11787.
19. S. S. Zhang, *Journal of Power Sources*, 2013, **231**, 153-162.
20. Y. X. Yin, S. Xin, Y. G. Guo and L. J. Wan, *Angewandte Chemie International Edition*, 2013, **52**, 13186-13200.
21. K. Hernández-Burgos, Z. J. Barton and J. Rodríguez-López, *Chemistry of Materials*, 2017, **29**, 8918-8931.
22. D. L. Williams, J. J. Byrne and J. S. Driscoll, *Journal of The Electrochemical Society*, 1969, **116**, 2-4.
23. H. Alt, H. Binder, A. Köhling and G. Sandstede, *Electrochimica Acta*, 1972, **17**, 873-887.
24. J. i. Yamaki and A. Yamaji, *Journal of The Electrochemical Society*, 1982, **129**, 5-9.
25. H. Shirakawa, E. J. Louis, A. G. MacDiarmid, C. K. Chiang and A. J. Heeger, *Journal of the Chemical Society, Chemical Communications*, 1977, 578-580.
26. P. Novák, K. Müller, K. S. V. Santhanam and O. Haas, *Chemical Reviews*, 1997, **97**, 207-282.
27. G. MacDiarmid Alan, *Angewandte Chemie International Edition*, 2001, **40**, 2581-2590.
28. A. M. Bryan, L. M. Santino, Y. Lu, S. Acharya and J. M. D'Arcy, *Chemistry of Materials*, 2016, **28**, 5989-5998.
29. L. Nyholm, G. Nyström, A. Mihranyan and M. Strømme, *Advanced Materials*, 2011, **23**, 3751-3769.
30. N. Kenji Shinozaki and Yukio Tomizuka and Akio, *Japanese Journal of Applied Physics*, 1984, **23**, L892.
31. L. W. Shacklette, N. S. Murthy and R. H. Baughman, *Molecular Crystals and Liquid Crystals*, 1985, **121**, 201-209.
32. S. Taguchi and T. Tanaka, *Journal of Power Sources*, 1987, **20**, 249-252.
33. R. Bittihn, G. Ely, F. Woeffler, H. Münstedt, H. Naarmann and D. Naegele, 1987.

34. I. Keiichi Kaneto and Katsumi Yoshino and Yoshio, *Japanese Journal of Applied Physics*, 1983, **22**, L567.
35. J. Simons Tristan, M. Salsamendi, C. Howlett Patrick, M. Forsyth, R. MacFarlane Douglas and C. Pozo-Gonzalo, *ChemElectroChem*, 2015, **2**, 2071-2078.
36. Y. Liang, Z. Tao and J. Chen, *Advanced Energy Materials*, 2012, **2**, 742-769.
37. T. B. Schon, B. T. McAllister, P.-F. Li and D. S. Seferos, *Chemical Society Reviews*, 2016, **45**, 6345-6404.
38. S. J. Visco, C. C. Mailhe, L. C. De Jonghe and M. B. Armand, *Journal of The Electrochemical Society*, 1989, **136**, 661-664.
39. S. J. Visco, M. Liu and L. C. De Jonghe, *Journal of The Electrochemical Society*, 1990, **137**, 1191-1192.
40. S. J. Visco and L. C. DeJonghe, *Journal of The Electrochemical Society*, 1988, **135**, 2905-2909.
41. N. Oyama, T. Tatsuma, T. Sato and T. Sotomura, *Nature*, 1995, **373**, 598.
42. T. Inamasu, D. Yoshitoku, Y. Sumi-otorii, H. Tani and N. Ono, *Journal of The Electrochemical Society*, 2003, **150**, A128-A132.
43. M. Amaike and T. Iihama, *Synthetic Metals*, 2006, **156**, 239-243.
44. K. Naoi, K. i. Kawase and Y. Inoue, *Journal of The Electrochemical Society*, 1997, **144**, L170-L172.
45. I. Gomez, O. Leonet, J. Alberto Blazquez, H.-J. Grande and D. Mecerreyes, *ACS Macro Letters*, 2018, 419-424.
46. K. Zhang, C. Guo, Q. Zhao, Z. Niu and J. Chen, *Advanced Science*, 2015, **2**, 1500018.
47. Y. Liang, P. Zhang, S. Yang, Z. Tao and J. Chen, *Advanced Energy Materials*, 2013, **3**, 600-605.
48. K. Hernández-Burgos, G. G. Rodríguez-Calero, W. Zhou, S. E. Burkhardt and H. D. Abruña, *Journal of the American Chemical Society*, 2013, **135**, 14532-14535.

49. K. Hernández-Burgos, S. E. Burkhardt, G. G. Rodríguez-Calero, R. G. Hennig and H. D. Abruña, *The Journal of Physical Chemistry C*, 2014, **118**, 6046-6051.
50. J. S. Foos, S. M. Erker and L. M. Rembetsy, *Journal of The Electrochemical Society*, 1986, **133**, 836-841.
51. Z. Song, H. Zhan and Y. Zhou, *Angewandte Chemie International Edition*, 2010, **49**, 8444-8448.
52. T. Ma, Q. Zhao, J. Wang, Z. Pan and J. Chen, *Angewandte Chemie International Edition*, 2016, **55**, 6428-6432.
53. W. Huang, Z. Zhu, L. Wang, S. Wang, H. Li, Z. Tao, J. Shi, L. Guan and J. Chen, *Angewandte Chemie International Edition*, 2013, **52**, 9162-9166.
54. Z. Zhu, M. Hong, D. Guo, J. Shi, Z. Tao and J. Chen, *Journal of the American Chemical Society*, 2014, **136**, 16461-16464.
55. K. Koshika, N. Chikushi, N. Sano, K. Oyaizu and H. Nishide, *Green Chemistry*, 2010, **12**, 1573-1575.
56. T.-T. Truong, G. W. Coates and H. D. Abruna, *Chemical Communications*, 2015, **51**, 14674-14677.
57. J. Kim, H.-S. Park, T.-H. Kim, S. Yeol Kim and H.-K. Song, *Physical Chemistry Chemical Physics*, 2014, **16**, 5295-5300.
58. A. A. Golriz, T. Suga, H. Nishide, R. Berger and J. S. Gutmann, *RSC Advances*, 2015, **5**, 22947-22950.
59. G.-S. Liou and C.-W. Chang, *Macromolecules*, 2008, **41**, 1667-1674.
60. S. Wang, Q. Wang, P. Shao, Y. Han, X. Gao, L. Ma, S. Yuan, X. Ma, J. Zhou, X. Feng and B. Wang, *Journal of the American Chemical Society*, 2017, **139**, 4258-4261.
61. C. R. Mulzer, L. Shen, R. P. Bisbey, J. R. McKone, N. Zhang, H. D. Abruña and W. R. Dichtel, *ACS Central Science*, 2016, **2**, 667-673.
62. F. Xu, S. Jin, H. Zhong, D. Wu, X. Yang, X. Chen, H. Wei, R. Fu and D. Jiang, *Scientific Reports*, 2015, **5**, 8225.

63. J. Wang, C. S. Chen and Y. Zhang, *ACS Sustainable Chemistry & Engineering*, 2018, **6**, 1772-1779.
64. H.-C. Lin, C.-C. Li and J.-T. Lee, *Journal of Power Sources*, 2011, **196**, 8098-8103.
65. Y. H. Wang, M. K. Hung, C. H. Lin, H. C. Lin and J. T. Lee, *Chem Commun (Camb)*, 2011, **47**, 1249-1251.
66. W. Choi, S. Ohtani, K. Oyaizu, H. Nishide and K. E. Geckeler, *Adv Mater*, 2011, **23**, 4440-4443.
67. Y. Kiya, A. Iwata, T. Sarukawa, J. C. Henderson and H. D. Abruña, *Journal of Power Sources*, 2007, **173**, 522-530.
68. R. A. Davoglio, S. R. Biaggio, R. C. Rocha-Filho and N. Bocchi, *Journal of Power Sources*, 2010, **195**, 2924-2927.
69. T. Sarukawa and N. Oyama, *Journal of The Electrochemical Society*, 2010, **157**, F23.
70. J. Fanous, M. Wegner, J. Grimminger, Ä. Andresen and M. R. Buchmeiser, *Chemistry of Materials*, 2011, **23**, 5024-5028.
71. A. G. Simmonds, J. J. Griebel, J. Park, K. R. Kim, W. J. Chung, V. P. Oleshko, J. Kim, E. T. Kim, R. S. Glass, C. L. Soles, Y.-E. Sung, K. Char and J. Pyun, *ACS Macro Letters*, 2014, **3**, 229-232.
72. J. Geng, J.-P. Bonnet, S. Renault, F. Dolhem and P. Poizot, *Energy & Environmental Science*, 2010, **3**, 1929.
73. Z. Song, H. Zhan and Y. Zhou, *Angew Chem Int Ed Engl*, 2010, **49**, 8444-8448.
74. R.-h. Zeng, X.-p. Li, Y.-c. Qiu, W.-s. Li, J. Yi, D.-s. Lu, C.-l. Tan and M.-q. Xu, *Electrochemistry Communications*, 2010, **12**, 1253-1256.
75. S. Renault, J. Geng, F. Dolhem and P. Poizot, *Chem Commun (Camb)*, 2011, **47**, 2414-2416.
76. Z. Lei, W. Wei-kun, W. An-bang, Y. Zhong-bao, C. Shi and Y. Yu-sheng, *Journal of The Electrochemical Society*, 2011, **158**, A991.

77. K. Pirnat, R. Dominko, R. Cerc-Korosec, G. Mali, B. Genorio and M. Gaberscek, *Journal of Power Sources*, 2012, **199**, 308-314.
78. M. Lee, J. Hong, D. H. Seo, D. H. Nam, K. T. Nam, K. Kang and C. B. Park, *Angew Chem Int Ed Engl*, 2013, **52**, 8322-8328.
79. M. Lee, J. Hong, H. Kim, H. D. Lim, S. B. Cho, K. Kang and C. B. Park, *Adv Mater*, 2014, **26**, 2558-2565.
80. W. Wan, H. Lee, X. Yu, C. Wang, K.-W. Nam, X.-Q. Yang and H. Zhou, *RSC Adv.*, 2014, **4**, 19878-19882.
81. H. Li, W. Duan, Q. Zhao, F. Cheng, J. Liang and J. Chen, *Inorg. Chem. Front.*, 2014, **1**, 193-199.
82. A. Iordache, V. Maurel, J.-M. Mouesca, J. Pécaut, L. Dubois and T. Gutel, *Journal of Power Sources*, 2014, **267**, 553-559.
83. H. Kim, D. H. Seo, G. Yoon, W. A. Goddard, 3rd, Y. S. Lee, W. S. Yoon and K. Kang, *J Phys Chem Lett*, 2014, **5**, 3086-3092.
84. S. Gottis, A. L. Barres, F. Dolhem and P. Poizot, *ACS Appl Mater Interfaces*, 2014, **6**, 10870-10876.
85. A. Shimizu, H. Kuramoto, Y. Tsujii, T. Nokami, Y. Inatomi, N. Hojo, H. Suzuki and J.-i. Yoshida, *Journal of Power Sources*, 2014, **260**, 211-217.
86. G. S. Vadehra, R. P. Maloney, M. A. Garcia-Garibay and B. Dunn, *Chemistry of Materials*, 2014, **26**, 7151-7157.
87. Y. Liang, P. Zhang, S. Yang, Z. Tao and J. Chen, *Advanced Energy Materials*, 2013, **3**, 600-605.
88. J. Kim, J. Kim, J. Lee, H.-K. Song and C. Yang, *ChemElectroChem*, 2014, **1**, 1618-1622.
89. Y. F. Shen, D. D. Yuan, X. P. Ai, H. X. Yang and M. Zhou, *Electrochemistry Communications*, 2014, **49**, 5-8.
90. Z. Song, Y. Qian, X. Liu, T. Zhang, Y. Zhu, H. Yu, M. Otani and H. Zhou, *Energy Environ. Sci.*, 2014, **7**, 4077-4086.
91. H. Wu, S. A. Shevlin, Q. Meng, W. Guo, Y. Meng, K. Lu, Z. Wei and Z. Guo, *Adv Mater*, 2014, **26**, 3338-3343.

92. D. Tian, H.-Z. Zhang, D.-S. Zhang, Z. Chang, J. Han, X.-P. Gao and X.-H. Bu, *RSC Advances*, 2014, **4**, 7506.
93. A. Shimizu, Y. Tsujii, H. Kuramoto, T. Nokami, Y. Inatomi, N. Hojo and J.-i. Yoshida, *Energy Technology*, 2014, **2**, 155-158.
94. L. Fédèle, F. Sauvage and M. Bécuwe, *J. Mater. Chem. A*, 2014, **2**, 18225-18228.
95. H. Wu, Q. Meng, Q. Yang, M. Zhang, K. Lu and Z. Wei, *Adv Mater*, 2015, **27**, 6504-6510.
96. K. Zhang, C. Guo, Q. Zhao, Z. Niu and J. Chen, *Adv Sci (Weinh)*, 2015, **2**, 1500018.
97. G. Hernández, N. Casado, R. Coste, D. Shanmukaraj, L. Rubatat, M. Armand and D. Mecerreyes, *RSC Advances*, 2015, **5**, 17096-17103.
98. B. Haupler, T. Hagemann, C. Friebe, A. Wild and U. S. Schubert, *ACS Appl Mater Interfaces*, 2015, **7**, 3473-3479.
99. D. Schmidt, B. Häupler, C. Stolze, M. D. Hager and U. S. Schubert, *Journal of Polymer Science Part A: Polymer Chemistry*, 2015, **53**, 2517-2523.
100. M. E. Bhosale and K. Krishnamoorthy, *Chemistry of Materials*, 2015, **27**, 2121-2126.
101. D. Chen, A. J. Avestro, Z. Chen, J. Sun, S. Wang, M. Xiao, Z. Erno, M. M. Algaradah, M. S. Nassar, K. Amine, Y. Meng and J. F. Stoddart, *Adv Mater*, 2015, **27**, 2907-2912.
102. Z. Song, Y. Qian, M. L. Gordin, D. Tang, T. Xu, M. Otani, H. Zhan, H. Zhou and D. Wang, *Angew Chem Int Ed Engl*, 2015, **54**, 13947-13951.
103. Z. Song, Y. Qian, T. Zhang, M. Otani and H. Zhou, *Adv Sci (Weinh)*, 2015, **2**, 1500124.
104. Y. Liang, Z. Chen, Y. Jing, Y. Rong, A. Facchetti and Y. Yao, *J Am Chem Soc*, 2015, **137**, 4956-4959.
105. A. Vlad, K. Arnould, B. Ernould, L. Sieuw, J. Rolland and J.-F. Gohy, *Journal of Materials Chemistry A*, 2015, **3**, 11189-11193.

106. F. Xu, S. Jin, H. Zhong, D. Wu, X. Yang, X. Chen, H. Wei, R. Fu and D. Jiang, *Sci Rep*, 2015, **5**, 8225.
107. J. Wu, X. Rui, C. Wang, W.-B. Pei, R. Lau, Q. Yan and Q. Zhang, *Advanced Energy Materials*, 2015, **5**, 1402189.
108. V. A. Oltean, S. Renault and D. Brandell, *Electrochemistry Communications*, 2016, **68**, 45-48.
109. F. Xu, J. Xia and W. Shi, *Electrochemistry Communications*, 2015, **60**, 117-120.
110. A. E. Lakraychi, F. Dolhem, F. Djedaïni-Pilard, A. Thiam, C. Frayret and M. Becuwe, *Journal of Power Sources*, 2017, **359**, 198-204.
111. S. Wang, Q. Wang, P. Shao, Y. Han, X. Gao, L. Ma, S. Yuan, X. Ma, J. Zhou, X. Feng and B. Wang, *J Am Chem Soc*, 2017, **139**, 4258-4261.
112. F. Xu, X. Chen, Z. Tang, D. Wu, R. Fu and D. Jiang, *Chem Commun (Camb)*, 2014, **50**, 4788-4790.
113. J. Kim, H. S. Park, T. H. Kim, S. Y. Kim and H. K. Song, *Phys Chem Chem Phys*, 2014, **16**, 5295-5300.
114. B. Haupler, R. Burges, C. Friebe, T. Janoschka, D. Schmidt, A. Wild and U. S. Schubert, *Macromol Rapid Commun*, 2014, **35**, 1367-1371.
115. C. Su, F. Yang, L. Ji, L. Xu and C. Zhang, *J. Mater. Chem. A*, 2014, **2**, 20083-20088.
116. H. Zhu, J. Yin, X. Zhao, C. Wang and X. Yang, *Chem Commun (Camb)*, 2015, **51**, 14708-14711.
117. Y. Imada, H. Nakano, K. Furukawa, R. Kishi, M. Nakano, H. Maruyama, M. Nakamoto, A. Sekiguchi, M. Ogawa, T. Ohta and Y. Yamamoto, *J Am Chem Soc*, 2016, **138**, 479-482.
118. S. Zhang, W. Huang, P. Hu, C. Huang, C. Shang, C. Zhang, R. Yang and G. Cui, *Journal of Materials Chemistry A*, 2015, **3**, 1896-1901.
119. J. Wu, X. Rui, G. Long, W. Chen, Q. Yan and Q. Zhang, *Angewandte Chemie International Edition*, 2015, **54**, 7354-7358.

120. M. E. Speer, M. Kolek, J. J. Jassoy, J. Heine, M. Winter, P. M. Bieker and B. Esser, *Chem Commun (Camb)*, 2015, **51**, 15261-15264.
121. T. Godet-Bar, J. C. Lepretre, O. Le Bacq, J. Y. Sanchez, A. Deronzier and A. Pasturel, *Phys Chem Chem Phys*, 2015, **17**, 25283-25296.
122. J. Bitenc, K. Pirnat, G. Mali, B. Novosel, A. Randon Vitanova and R. Dominko, *Electrochemistry Communications*, 2016, **69**, 1-5.
123. J. Xiang, K. Sato, H. Tokue, K. Oyaizu, C.-L. Ho, H. Nishide, W.-Y. Wong and M. Wei, *European Journal of Inorganic Chemistry*, 2016, **2016**, 1030-1035.
124. É. Deunf, P. Jiménez, D. Guyomard, F. Dolhem and P. Poizot, *Electrochemistry Communications*, 2016, **72**, 64-68.
125. M. Kolek, F. Otteny, P. Schmidt, C. Mück-Lichtenfeld, C. Einholz, J. Becking, E. Schleicher, M. Winter, P. Bieker and B. Esser, *Energy & Environmental Science*, 2017, **10**, 2334-2341.
126. A. Wild, M. Strumpf, B. Häupler, M. D. Hager and U. S. Schubert, *Advanced Energy Materials*, 2017, **7**, 1601415.
127. C. Peng, G.-H. Ning, J. Su, G. Zhong, W. Tang, B. Tian, C. Su, D. Yu, L. Zu, J. Yang, M.-F. Ng, Y.-S. Hu, Y. Yang, M. Armand and K. P. Loh, *Nature Energy*, 2017, **2**, 17074.

CHAPTER 2

EXPERIMENTAL METHODS AND METRICS

2-1. Introduction

A number of electrochemical methods were routinely used in the chapters followed, and will be generalized in this section of Chapter 2.

2-2. Cyclic voltammetry (CV)

CV is one of the most commonly used electrochemical techniques to conveniently probe the electro-activity of species in question.[1, 2] In most instances, two aspects/metrics are of potential interest: the formal potential (E_0) and the chemical and electrochemical reversibility of the redox process. CV then becomes a very simple yet powerful method to answer these questions.

CV is a potentiodynamic technique used to monitor the change in current, a kinetic measure, as a function of the applied potential[iv], a thermodynamic measure. Two aspects are crucial for describing the electrochemical behavior of a species: kinetics and thermodynamics, and both are involved in cyclic voltammetry. In CV, potential is the thermodynamic measure and current is the kinetic measure of the corresponding redox process. In other words, in a CV we measure the kinetics of a redox process as a potential function is varied linearly. In electrochemistry, the Butler-Volmer (Figure 2-2, Equation (1)), where i is the measured current, i_o is the exchange current, α describes the symmetry between oxidation and reduction transfer coefficient, n is the number of electrons transfer, η is overpotential, F is Faraday's

[iv] In from this chapter on, "voltage" and "potential" will be used interchangeably, as "potential" is the electrochemical term for "voltage".

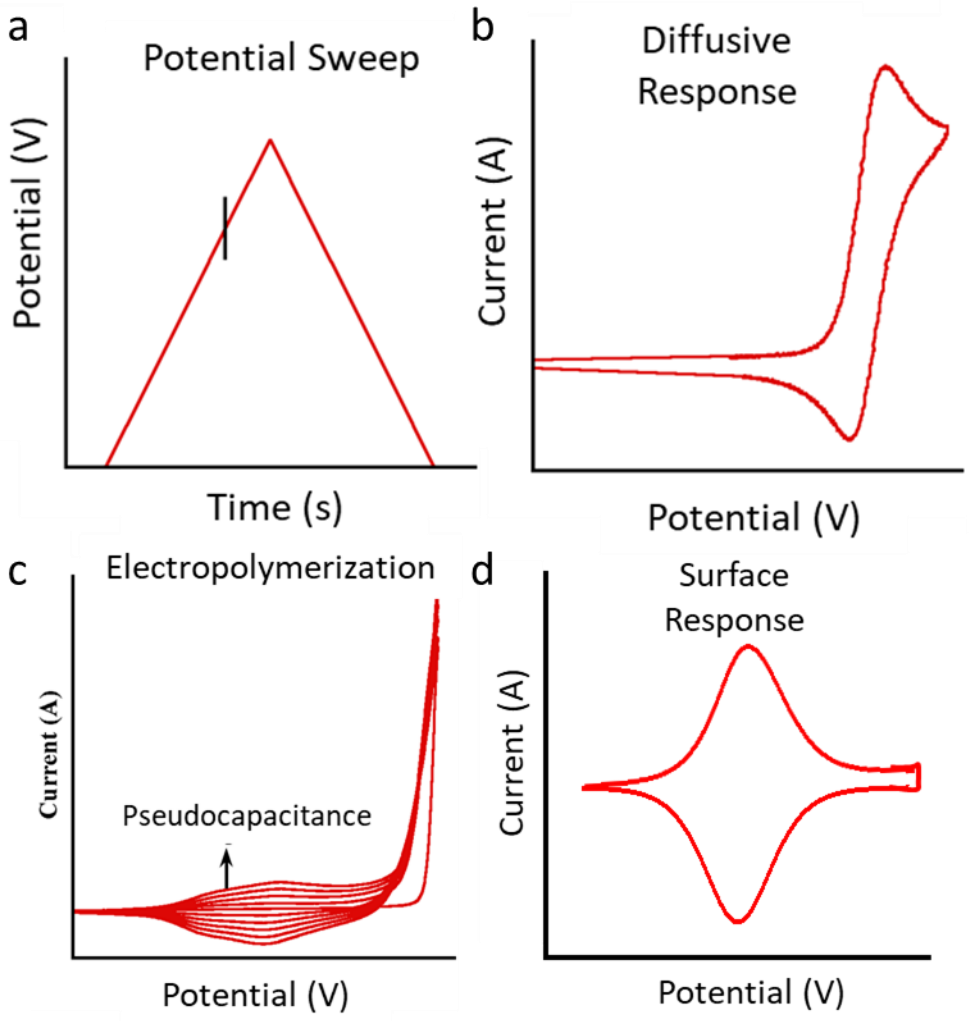

Figure 2-1. a) The potential sweep of a CV experiment. b) A typical CV response for a redox species in solution. c) A typical response of electropolymerization, using pyrrole as an example. d) A typical surface immobilized redox-active layer response; computer generated response.

constant, R is the gas constant 8.31 J/mol/K, and T is temperature in K. This equation basically states that the net current, i, is the combined response of oxidation and reduction as an exponential function of the overpotential. On the other hand, the thermodynamic behavior is related to the equilibrium between the oxidized and reduced species in solution, and is described by the Nernst equation (Figure 2-2, Equation (2)), where E is a given potential, E^o is the formal potential, R is the gas constant of 8.31, F is the Faraday constant, C_O is the concentration of the oxidized species and C_R is that of the reduced species. Here, the equilibrium between the oxidized and the reduced species is described by an exponential function of the formal potential of the redox process. By combining these two fundamental equations taking into account Fick's Laws of diffusion (Figure 2-2, Equation (3)) and assuming semi-infinite linear diffusion, CV is described by the Randles-Sevcik Equation (Figure 2-2, Equation (4)), where i_p is the peak current, A is the area of the electrode, υ is scan rate in V/s and D is the diffusion coefficient in cm^2/s.

Based on this fundamental description of CV, we can extract important electrochemical information from a set of simple CV experiments. For a reversible process[v], the formal potential (E^o) is one the most important values as it describes the potential at which the redox process occurs. We are also interested in assessing the reversibility of these processes, both chemically and electrochemically. Chemical reversibility can be assessed by simply looking at the ratio of $i_{p,c}$ and $i_{p,a}$, cathodic and anodic peak currents, respectively, and a ratio away from unity indicates various degrees of chemical irreversibility. Electrochemical reversibility in cyclic voltammetry

[v] This reversibility refers to general chemical reversibility, as described in a later paragraph.

can be assessed from the peak-to-peak separation (ΔE_p). For a reversible systems, this separation should be 59/n mV, and for a quasireversible system, at least 70/n mV. Reactants with a peak-to-peak separation larger than 90/n mV are generally considered electrochemically irreversible. For EESS applications, both chemical and electrochemical reversibilities are essential for the electrode candidate.

Finally, from CV, one can also determine the diffusion coefficient of the dissolved species in solution using the Randles-Sevcik equation. Between different species, one could compare the different diffusion coefficients of various species and determine the best material for their specific application.

CV can also be used in electropolymerizations. Different from chemical polymerization, electropolymerization is a process in which polymerization processes are initiated without the use of any chemical species, and instead, electrochemical processes (electrons or holes) are used as initiators. While both potential and current could be used as the initiators, for the vast portion of this dissertation, electropolymerization processes were initiated by controlling the applied potential, either statically or dynamically.

Using CV as the electropolymerization method, the main electropolymerization mechanism is described as ECE. The monomer first undergoes an electrochemical step, oxidation or reduction, which causes the subsequent chemical step, the polymerization step, and once a chemical bond is formed, a renewed electrochemical response will be shown as the polymer/oligomer is reduced, and the cycle continues. Since multiple electrochemical and chemical steps are involved in the electropolymerization process, the voltammograms are complex and often times not as

(1) *Butler-Volmer Equation*

$$i = i_o[e^{-\frac{\alpha nF}{RT}\eta} - e^{-\frac{(1-\alpha)nF}{RT}\eta}]$$

(2) *Nernst Equation*

$$E = E^o + \frac{RT}{nF} ln \frac{C_o}{C_R}$$

(3) *Fick's Law of Diffusion*

$$i = nFAD \left(\frac{\partial C}{\partial x}\right)_{x\,=\,0}$$

(4) *Randles-Sevcik Equation*

$$i_p = 2.69 \times 10^5\, n^{2/3} A\, C_{Ox}^b\, D_{Ox}^{1/2}\, \nu^{1/2}$$

(5) *Surface Coverage of Immobilized Layer*

$$i_p = \frac{n^2F^2}{4RT}\, \upsilon A\Gamma$$

(6) *Sand Equation*

$$i\tau^{1/2} = \frac{nFAD_O^{1/2} C_O^* \pi^{1/2}}{2}$$

(7) *Theoretical Capacity* (in mAh/g)

$$C_{Theo} = \frac{nF}{MW} \times \frac{1\ hr}{3600\ s}$$

(8) *Frequency of Acoustic Wave*

$$f_o = \frac{\nu_{tr}}{2t_q} = \left(\frac{\mu_q^{\frac{1}{2}}}{\rho_q^{\frac{1}{2}}}\right)/2t_q$$

(9) *Frequency to Thickness Substitution*

$$\frac{\Delta f}{f_o} = -\frac{\Delta t}{t_q} = -2f_o \Delta t/\upsilon_{tr}$$

(10) *The Sauerbrey Equation*

$$\Delta f = -\frac{2f_u^2}{(\rho_q \mu_q)^{1/2}} \cdot \frac{\Delta m}{A} = -\,C_f \cdot \frac{\Delta m}{A}$$

Figure 2-2. List of equations included in Chapter 2.

reversible as expected for a simple redox reaction in monomer solution. Nonetheless, electropolymerization voltammograms should be relatively well-defined, meaning that there should be trends that can be followed to monitor the progress of the electropolymerization process.

The progress of the electropolymerization process can be followed by monitoring any growth in the double-layer capacitance in the voltammograms. As the polymer film is deposited onto the electrode surface, depending on the electronic conductivity of the resulting polymer film, there should be either a growth in the double-layer capacitance, if high conductivity is expected for the deposition, and a decrease of double-layer capacitance, if low or no conductivity is expected. As a result, a limit of film thickness, i.e. electropolymerization cycles, can be determined should a film become too thick and insulating in nature.

The growing layer on the electrode surface becomes an immobilized material with very interesting electrochemical properties. First of all, for films in the 100 – 200 nm range, they generally exhibit fast charge behavior with no counter-ion transport limitations. Since the redox-active species is anchored onto the electrode surface, and exhibits fast charge, the peak-to-peak is often close to the theoretical value of 0 mV.

Secondly, because the redox active component is immobilized on the electrode surface, one can calculate their concentration on the electrode surface and hence, their surface coverage. Their surface coverage can be determined using Equation (5) (Figure 2-2). Based on the scale factor that one monolayer is of the order of 10^{-10} mol/cm^2, we can determine the approximate number of monolayers deposited onto the electrode surface and can provide information regarding the density of the deposit.

While one can carry out a more detailed analysis of the electrochemical responses, for the purpose of this dissertation, I will only focus on the properties mentioned above. For detailed experimental setups, the reader is referred to specific experiments in the corresponding chapters.

2-3. Battery Metrics, Assembly and Testing

In this chapter, we will introduce and present the working of coin cells as the primary device-level characterization of battery materials in this dissertation.[3]

The fundamental electrochemical basis for battery testing is based on galvanostatic (controlled current) chronopotentiometric methods, in which a constant current is applied to a system and the potential is monitored as a function of time. This method is analogous to chronoamperometric measurements where constant potential is applied and current is monitored as a function of time.

The electrochemical behavior of a redox species can be described by Butler-Volmer kinetics and the Sand equation.[2, 3] When a constant current is applied to a system, oxidized (*O*) species on the electrode surface will become reduced in order to sustain the applied current and the potential of the system will be changed to maintain that condition. At the potential where a redox process is expected, the system will adjust the potential in order to sustain the applied current, generating a voltage plateau. During this time where a plateau is sustained, *O* at the electrode surface will continue to be reduced and diffuse away, until such a time (transition time τ) is reached that there is no more *O* on the electrode surface to be reduced. At this time, the potential of the system will re-adjust itself to a new value in order to sustain the applied current, forming another plateau.

Quantitatively speaking, chronopotentiometric behavior is described by the Sand (Figure 2-2, Equation (6)). Here, τ is described as Sand's transition time, and it

expresses the amount of time for all the surface O to be reduced to R, and the higher the applied current, the shorter the τ. Therefore, the term $i\tau^{1/2}$ in the equation is constant.

A coin cell is the smallest practical device characterization for batteries (lithium, lithium-ion batteries) and is the standard device-level characterization for research laboratory settings. In our laboratory, most device-level characterization is performed using "half-cell" lithium coin cells, using lithium foil as the anode, and are assembled and tested in CR2032 type coin cells. Detailed electrode fabrication processes and cell assembly can be found in the experimental sections of the respective chapters.

The following is a list of common terms used when evaluating the performance of an electrode material in device-level battery characterization. These metrics will provide full evaluation examining the material's strength and weaknesses in terms of capacity, stability and rate capability of an electrode material for battery applications

Theoretical capacity: charges gained/released based on the redox behavior of the given materials. It is defined in Equation (7) (Figure 2-2) for well-defined redox processes in electrode materials, and is usually expressed in terms of gravimetric capacity (mAh/g). For example, $LiCoO_2$ has a theoretical capacity of 272 mAh/g, while its reversible/practical capacity is limited to about 140 mAh/g.

Gravimetric energy density: is defined as the gravimetric capacity multiplied by the working voltage of the given material; usually expressed as Wh/g or Wh/kg. However, practically speaking, energy density refers to a device, in contrast to individual electrode materials. In that sense, the energy (Wh) comes from the total capacity of the cathode and anode, and the working voltage is the voltage difference between the cathode and the anode (instead of theoretical working voltages). In addition, mass (g)

should be taken as the mass of the device as a whole including cell casings, spacer, spring, separator, current collector, electrolyte, etc. For example, a state-of-the-art lithium-ion battery in a 18650 cell has an average voltage of 3.65 V and a gravimetric energy density approaching 270 Wh/kg.

Volumetric energy density: see explanation for ***gravimetric energy density***; energy density given per volume, usually expressed as Wh/L. For example, a state-of-the-art lithium-ion battery in an 18650 cell format has an average voltage V have volumetric energy density of about 770 Wh/L.

Power density: the power density of a device is defined as the energy released in a given time. The simplest way to calculate power density is to divide the energy density by time (see C-rate). It is usually expressed in terms of W/kg or W/L.

Working voltage: there are numerous terms in the battery field describing the "voltage plateaus" of a device, and the working voltage is arguably among the most important ones as it is the most representative value describing the operating voltage of a device under operating conditions. As there is generally sloping in the charge and discharge profiles, the working voltage is given by the measuring device and is carefully calibrated based on the conditions tested. For example, a typical lithium-ion battery using a $LiCoO_2$ cathode has a working voltage of 3.6 – 3.7 V, in most cases.

C-rate: this term describes the rate at which the device is charged/discharged, and C-rate is short for "current rate". 1 C means that the device can be charged or discharged in 1 hour. Thus, ½ (0.5) C means that the device can be charged or discharged in 2 hours. The higher the C-rate, the faster the charging and discharging rates. When current rate is described as A/g or mA/g, divide the total capacity (mAh/g) by the current rate (mA/g), then the inverse of the resulting h (hour) will be the corresponding C-rate.

Capacity retention: it refers the percentage of the capacity remaining after prolonged

cycling.

2-4. Electrochemical Quartz Crystal Microbalance (EQCM)

EQCM is a powerful technique that enables the measurement of mass changes occurring from redox processes of electroactive films on electrodes.[4] This is achieved by the piezoelectric properties of a quartz crystal electrode used in *EQCM*. This technique is based on the converse piezoelectric effect, which states that a strain is sensed by a piezoelectric material when a voltage is applied. This piezoelectric property existing in quartz crystals originates from its non-centrosymmetric crystalline structure. Because these crystalline materials are acentric, under stress, charges are generated due to the displacement in the atoms, which causes a dipole shift. Figures 2-3a and b show a QCM electrode, where the yellow region shows the electrodes under an applied potential. As indicated in Figure 2-3c and d, the positive and negative dipoles are presents in the quartz crystal, and when a potential is applied, the ions in the crystal will move in shear mode to cause a vibration, and the frequency is detected.

The frequency results in the vibrational motion of a quartz crystal, establishing a transverse acoustic wave across the crystal. Moreover, this acoustic wave relates to the thickness of the quartz crystal (t_q) and a standing wave condition can be established for acoustic wavelengths at $2t_q$. Similarly, if a foreign layer is deposited onto the quartz surface, the acoustic wave will propagate through both the quartz and the foreign layer. If one assumes that the foreign layer has similar properties to the quartz crystal (details discussed next), this layer and the quartz can be considered a "composite resonator", and this layer contributes to the overall vibrational motion of the composite resonator. As frequency of the quartz is directly related to thickness,

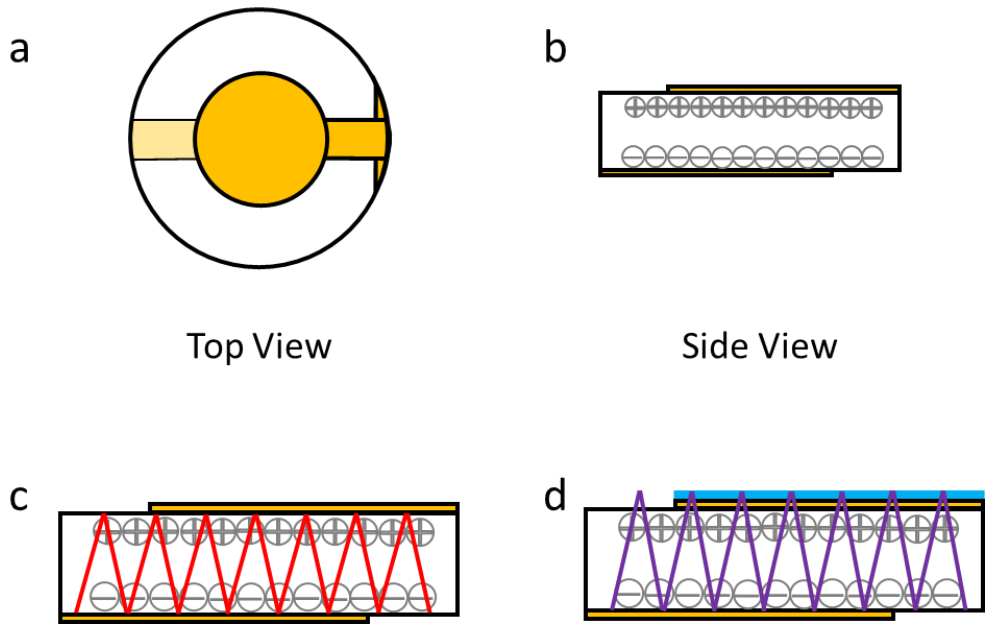

Figure 2-3. a) Top view of a Au-coated QCM electrode. b) Side view of a Au-coated QCM electrode. c) Vibration mode of a bare QCM electrode; yellow layer indicated the Au electrode. d) Vibration mode of a QCM electrode with a rigid film deposited; blue layer indicating a layer of foreign film deposited on Au electrode.

then a small change in thickness corresponds to a small change in frequency (Equation 8-9), which can then be correlated to a small change to mass, as expressed in the Sauerbrey Equation (10) (Figure 2-2). In these relations, the frequency of the quartz crystal, f_o, is correlated with the traverse velocity of the acoustic wave, υ_{tr}, which is also correlated with the density, ρ_q, and shear modulus, μ_q, of the quartz. They are collectively expressed as the acoustic impedance of the quartz, $z = \rho_q \upsilon_{tr} = (\rho_q \mu_q)^{1/2}$, which under the condition of the Sauerbrey Equation, is assumed to be the same for the quartz and the foreign layer.

As previously discussed, the foreign layer needs to have similar properties to the quartz crystal for the direct applicability of the Sauerbrey Equation. We will first briefly discuss the case when the foreign layer is dissimilar to the quartz. In those cases, because we cannot directly apply the Sauerbrey Equation to correlate frequency dynamics to mass dynamics, we need to invoke the electro-mechanical model to describe the *EQCM* to gain a better understanding. A QCM is a harmonic oscillator (Figure 2-4a). For the mechanical model, it is a pendulum that oscillates at a frequency, and hence the behavior of a QCM is described as a pendulum with a spring constant (k) and the length of the string. As a result, the QCM oscillator can be dampened by air (r) or other mechanisms that cause it to dissipate energy, and mass loadings (M) give rises to a drop in frequency and *vice versa*. In the electrical model, an LCR circuit, which consists of a circuit with an inductor, capacitor, and resistor connected in series, behaves like a harmonic oscillator. The inductor and the capacitor connecting in series induce oscillation in the circuit, and the resistor dampens the oscillation. To account other effects, a capacitor is added in parallel to the LCR circuit,

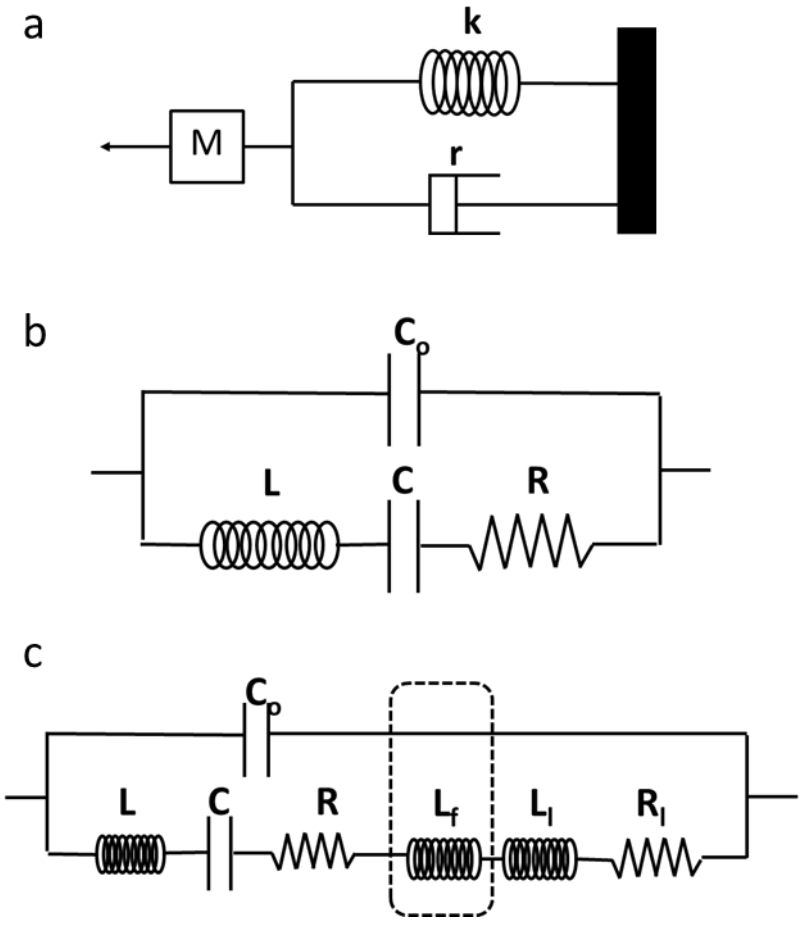

Figure 2-4. a) Harmonic oscillator model for the QCM setup. b) Basic electro-mechanical model for the bare QCM circuit. c) Electro-mechanical model for QCM circuit with a rigid film deposition, including solvent (l) components.

yielding an electrical model for the QCM in vacuum systems (Figure 2-4b). However, when a foreign layer is deposited onto the electrode and in liquid media, the overall system becomes more complicated (Figure 2-4c). Even though it is not always used for quantitative *EQCM* measurement, the electro-mechanical modeling is essential in accurately predicting the behavior of a composite QCM electrode and calibration of the system.

When the foreign layer is similar to the QCM electrode, the Sauerbrey Equation can be applied directly to correlate frequency changes to mass changes of a system. Three conditions have to be met for the foreign layer to be considered similar to QCM and allow for the direct application of the Sauerbrey Equation: 1) the foreign layer has to be a rigid film; 2) the layer is of uniform thickness; and 3) the layer has to be of low mass loading compared to the mass of the QCM. Firstly, a film is considered rigid if it vibrates in phase with the QCM electrode without significant lag, which becomes problematic when a soft film or a very thick film is deposited. In those cases, various additional factors are convoluted, including mass loading, thickness, and rheology, making the behavior of the composite resonator much less predictable. Secondly, a uniform thickness of the foreign layer is required for the direct application of the Sauerbrey Equation as the differential sensitivity constant of the quartz, *Cf*, is not uniform radially. Studies have shown that *Cf*, expressed as $2f_o^2/(\mu_q\rho_q)^{1/2}$, is highest at the center of the quartz electrode, then the electrode would be less sensitive to changes to a foreign layer with much thicker radial edges. Finally, the foreign film has to be of low mass loading to allow for the direct application of the Sauerbrey Equation. A high mass loading implies a decrease of sensitivity of the quartz from

inspection of the Sauerbrey Equation, and could induce dampening effects onto the quartz as a result. In most cases, mass of the foreign film should not exceed 2% of the mass of the QCM. While some methods can tolerate mass loading up to 10%, the QCM system is the best behaved at low mass loadings.

For the purpose of this dissertation, our systems were well behaved polymer thin-film systems that comply with all the criteria described above. With no significant rheological changes, thicknesses between 40 – 100 nm and mass loadings under 7.0 μg, the viscoelastic properties of these polymer films allow the direct application of the Sauerbrey Equation.

REFERENCES

1. Elgrishi, N.; Rountree, K. J.; McCarthy, B. D.; Rountree, E. S.; Eisenhart, T. T.; Dempsey, J. L. *Journal of Chemical Education* **2018,** *95* (2), 197-206.

2. Bard, A.; Faulkner, L., *Electrochemical Methods: Fundamentals and Applications*. John Wiley & Sons, Inc: 2001.

3. Linden, D.; Reddy, T., *Handbook of Batteries*. McGraw-Hill Education: 2001.

4. Buttry, D. A.; Ward, M. D., Measurement of interfacial processes at electrode surfaces with the electrochemical quartz crystal microbalance. *Chemical Reviews* **1992,** *92* (6), 1355-1379.

CHAPTER 3

HYBRID ORGANIC ELECTRODES: THE RATIONAL DESIGN AND SYNTHESIS OF HIGH-ENERGY REDOX-ACTIVE PENDANT FUNCTIONALIZED POLYPYRROLES FOR ELECTROCHEMICAL ENERGY STORAGE[vi]

3-1. Introduction

Among organic electrodes studied for electrical energy storage applications, one division is to categorize them into redox-active and conducting polymers.[1] Macromolecules with discrete redox-active units tethered to discrete polymer backbones generate an enormous library of organic materials capable of exchanging one or more electrons while limiting mass per repeating unit. Utilizing redox-active units such as TEMPO, phenothiazine, anthraquinone,[2-4] polymers with this tethering architecture can reach capacities of up to 210 mAh/g with up to 2000 cycles of cycling stability, owing to the high-energy redox-active pendant and the inert polymer backbone support.[5,6] However, as most inert polymer backbones involve electronically insulting architectures (i.e. polyethylene, polypropylene, polystyrene), such polymer materials are frequently "redox conducting" rather than "electronically conducting" materials. Thus, often more than 50 weight % (wt%) of conducting additive is required during electrode fabrication for device testing, and in some cases up to 80 wt % of conductive carbon is used.[2, 6-10] This detrimental lack of electronic

[vi] This chapter was reproduced in part with permission from *J. Electrochem. Soc.,* **2017**, *164* (9), A1946-A1951.

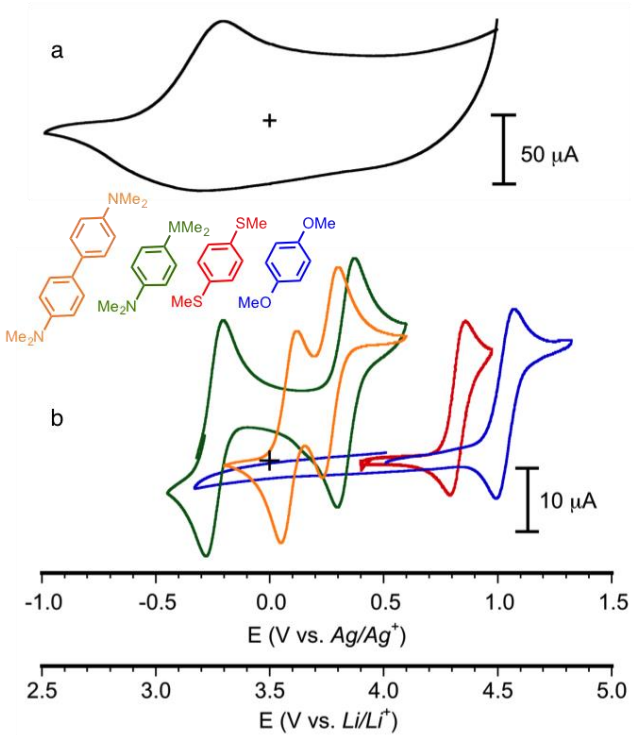

Figure 3-1. Cyclic voltammograms of polypyrrole (PPy) (a, black), TMPD (b, green), BMTB (b, red), DMB (b, blue) and TMB (b, yellow). CV were taken in 0.1 M TBAP/MeCN solution at 50 mV/s in a and 1 mM of monomers in the same electrolyte solution at 20 mV/s for b

conductivity greatly hinders the use of polymer tethered redox-active organic materials as viable electrode materials.

In contrast, electronically conducting polymer (CPs) is a class of organic polymers exhibiting relatively high electronic conductivities. The effective conjugation of the extended π-system enables conducting polymers to exhibit conductivities of up to 1000 S/cm, potentially aiding charge-transfer kinetics.[11-13] Often being used in thin-film devices for (super)capacitor applications, conducting polymers are often cycled at high rates with cyclability of 20,000 cycles or higher.[14, 15] While the rate performance and cycling stability of CPs are impressive, their limited ability to exchange discrete electrons undermines much of their potentials as battery electrodes. While redox polymers can exchange one or more electrons per repeating units, conducting polymers undergo "doping" processes. Instead of a Faradaic process of electron transfer, conducting polymers are continuously oxidized/reduced over a wide potential window (non-faradaic), resulting in less than one electron per unit (generally 0.3 – 0.5 electron per repeating unit).[16]

Our group has previously reported architectures that combine the best features of both redox-active polymers and electronically conducting polymers. The goal is to achieve high-energy using redox-active units and high-power properties by using a conducting polymer backbone.[17, 18] A poly(3,4-ethylenedioxythiophene) (PEDOT) tethered 5,5′-bis(methylthio)-2,2′-bithiophene (bmtbt) polymer was successfully electropolymerized to achieve a high-capacity polymer with improved electronic conductivity. Subsequently, tetraalkylphenylenediamine (TAPD), a much-studied redox-active unit, was paired with a PEDOT backbone to produce a thin-film polymer

with two discrete redox couples at close to 4.0 V vs. *Li/Li+*.

In addition, the synthesis and polymerization process of these polymers are interesting because electropolymerization is used as the main method to thin-film fabrication. As anticipated, multiply charged monomers were involved in the electropolymerization process and a number of important factors emerged as important in governing the stability and behavior, such as the redox potentials of the redox-active units and the monomer unit, as well as the distance between the two.[17]

In this chapter, I will initially discuss, in detail, the rational design of a library of redox-active pendants tethered to polypyrrole separated by a varied length alkyl chain in 3.2. Their electropolymerization behaviors were studied and elucidated in 3.3. The subsequent films were characterized in 3.4, revealing that while some redox-active units are prone to chemical degradation upon redox activity, PPy-nC-TMPD films turned out to have very favorable combined electrochemical properties and this represents an attractive energy storage electrode material.

3-2. Design Criteria

The design of hybrid materials for EES applications consists of a CP backbone and a redox-active pendant (RAP). The multifunctional CP backbone increases electronic conductivity and provides a backbone structure to mitigate/prevent dissolution of the polymer material. PPy was chosen as the CP backbone because of its high conductivity and insolubility as well as its electrochemical compatibility with the selected RAPs. PPy will have a wide window of conductivity between -0.7 - 1.0 V that overlaps with the redox potentials of the RAPs (Figure 3-1). The overlap of the redox processes of the RAPs and the PPy conductivity window are essential in the effective shuttling of charge carriers and electron propagation during the advent of redox processes.

Four redox-active small molecules were chosen as RAPs to be tethered onto a PPy backbone: 1.4-dimethoxybenzene (DMB), bis(methylthio)benzene (BMTB), *N,N,N',N'*-tetramethylphenylenediamine (TMPD) and *N,N,N',N'*-tetramethylbenzidine (TMB). The high capacities and working voltages stem from the low molecular mass and reversible exchange of at least one electron at high potentials. DMB and BMTB (Figure 3-1b) are redox-active organic molecules that can exchange one electron performula unit and, as organic cathodes, they yield theoretical capacities that are comparable to the practical capacities of commercial battery cathodes (~150 mAh/g) (DMB, 194 mAh.g; BMTB, 157 mAh/g).[7, 19] Moreover, due to their high formal potentials E^o (4.4 – 4.6 V vs. Li/Li^+), compared to current commercial materials, these molecules have theoretical energy densities approaching 800 Wh/kg, which are exceptional values among organic cathode materials.

TMPD and TMB, two chemically stable molecules capable of reversibly exchanging two electrons, are very competitive cathode materials when compared to the benchmark TEMPO-polymer based electrode materials mentioned above.[7] The quinone diimine resonance states provide the cation radical and dication species, respectively, great chemical stability.[20] As a result, the calculated theoretical capacities and energy densities of TMPD and TMB (326 mAh/g and 1338 Wh/kg, 223 mAh/g and 914 Wh/kg, respectively) approach the high end of energy densities for organic materials. Electrochemically, the peak-to-peak separation (ΔE_p) in the cyclic voltammogram, at a scan rate of 20 mV/s, for the two redox processes for both molecules is ca. 70 mV for all redox couples (Figure 3-1b), indicating facile charge transfer kinetics under these conditions. (It should be pointed that a sweep rate of 20

mV/s, in cyclic voltammetry, translates into a "C" rate in excess of 100C.) An additional attractive feature of TMB (relative to TMPD) is a decrease in the separation between the two redox processes (ΔE^o) from 580 mV in TMPD to 150 mV in TMB. This diminution in the "voltage penalty" is advantageous as it lowers the capacity loss as a result of voltage difference between the two processes. With all of these attractive features combined, TMPD and TMB represent the most promising RAPs in this family of molecules.

The CP and the RAPs are connected by alkyl chains of varying length (Scheme 3.1). In the course of our experiments, N-methylpyrrole (NMP) was used as a control monomer for RAP-functionalized pyrroles. As shown in Figure 3-3, since the onset potential of NMP oxidation (E_{onset}) (and thus, electropolymerization) is about +0.6 V, the pyrrole moieties of monomers **1** and **2** are predicted to oxidize and polymerize before their respective pendants undergo redox processes, and as a result, the alkyl spacer should not (or minimally) affect the process. However, monomers **3** and **4** are expected to undergo redox processes before the oxidation of NMP. We previously studied PEDOT-TAPD (equivalent to Py-2C-TMPD, in this work)[17] and were unable to electropolymerize this monomer with such a short alkyl linker. The separation of the RAP and the Py by the alkyl linker is intended to decrease charge localization (electrostatic repulsion) and improve stability as the monomers become triply and quadruply charged for monomers **3** and **4**, respectively, during the electropolymerization process. The alkyl linkers were varied from two to five

Table 3-1 Theoretical capacities and expected energy densities of the electropolymerized Py-C_n-RASs.

	Monomer	Theoretical Capacity ($mAh \cdot g^{-1}$)	Expected Number of e^- Exchanged	E vs. Li/Li^+ (V)	Expected Energy Density ($W \cdot h \cdot kg^{-1}$)
Py-C_n-DMB	**1a**	185.0	1.5	4.8	888
	1b	173.8	1.5	4.8	834
	1c	163.9	1.5	4.8	787
	1d	155.0	1.5	4.8	744
Py-C_n-BMTB	**2a**	152.6	1.5	4.6	702
	2b	144.9	1.5	4.6	667
	2c	137.9	1.5	4.6	634
Py-C_n-TMPD	**3a**	246.9	2.5	3.8, 4.3	1060
	3b	234.8	2.5	3.8, 4.3	1010
	3c	223.7	2.5	3.8, 4.3	962
$(Py\text{-}C_n)_2$-TMB	**4a**	188.5	3.0	4.0, 4.2	791
	4b	166.6	3.0	4.0, 4.2	700

a. Synthesis of bromopyrrole derivatives.

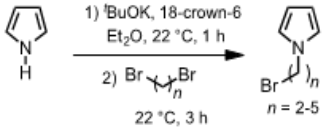

b. Synthesis of pyrrole monomers with pendant DMB, BMTB and TMPD groups.

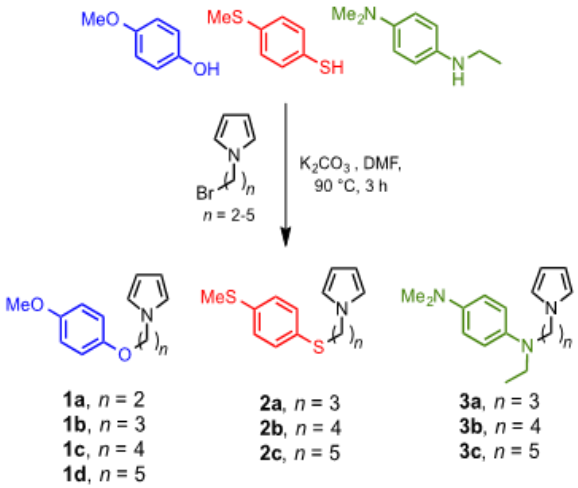

1a, n = 2
1b, n = 3
1c, n = 4
1d, n = 5

2a, n = 3
2b, n = 4
2c, n = 5

3a, n = 3
3b, n = 4
3c, n = 5

c. Synthesis of pyrrole monomers with pendant TMB.

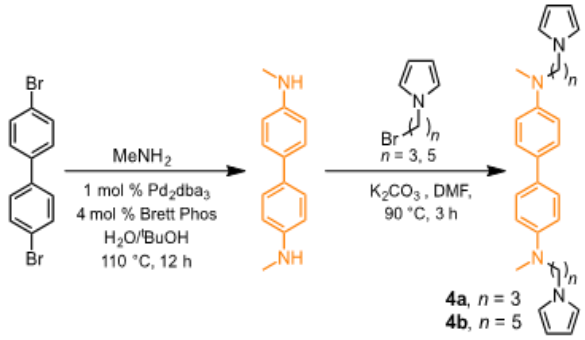

4a, n = 3
4b, n = 5

Scheme 3-1 Synthesis of (a) bromopyrrole derivatives, (b) 1a-d, 2a-c, 3a-c and (c) 4a-b.

methylene units in monomers **1** and three to five methylene units in monomers **2-4** in order to determine the shortest possible alkyl linker, and therefore the highest theoretical capacity material, while still maintaining a well-behaved electropolymerization processes.

Combining a PPy backbone with a RAP resulted in a new family of high energy density PPy-anchored redox active materials. Assuming a doping level of PPy of ca. 0.5, the calculated theoretical capacities of **1a-d, 2a-c, 3a-c** and **4a-b** approach 247 mAh/g, while their energy densities are predicted to be up to 1060 Wh/kg (Table 3.1). These values are three times higher than the energy densities typically observed for organic radical materials and are among the highest for organic materials.

3.3 Chemiscal Synthesis and Electropolymerization of Monomers

A series of monomers was synthesized based on literature precedent[17] (Scheme 3.1). The alkyl linkers were installed via a substitution reaction with dibromoalkyls (Scheme 3.1a), and the redox-active precursors were attached onto the pyrrole alkyls via substitution (Scheme 3.1b). The difunctional monomers **4a-b** were obtained by a two-step reaction (Scheme 3.1c).[21, 22] First, *N*, *N*'-dimethylbenzidine was synthesized by a Buchwald-Hartwig coupling with 1 mol % of $Pd_2(dba)_3$ as catalyst and 4 mol % of a ligand with dimethoxy substitution on the bicyclohexyl phosphine-containing arene. This ligand allows Pd-catalyzed amidation reactions of primary amines in high yield.[22] After 3 hours, the NMR spectrum showed resonances corresponding to the precursor as well as to the expected amine product. However, after 12 hours, the resonances corresponding to the precursor disappeared and the reaction afforded a quantitative yield. The crude amine could be easily purified via flash chromatography

on silica gel to yield the pure compound as a white solid. The structure was confirmed by ^{1}H and ^{13}C NMR (refer to supplemental information of manuscript). Subsequently, the pyrrole alkyl and redox-active moieties were reacted by a substitution reaction at the alkyl linkage, yielding the difunctionalized monomers **4a** and **4b,** which were expected to form cross-linked polymers when electropolymerized.

We chose cyclic voltammetry (CV) as the electropolymerization method because of the facile PPy electropolymerization under those conditions and direct deposition of polymer films onto substrates, which in a battery context, would serve as current collectors. Additionally, CV has many parameters that can be used to modulate and optimize the electropolymerization process, including potential range, scan rate and number of electropolymerization cycles.[15] For monomers **1a-d**, the oxidation of Py precedes that of the RAP, and the electropolymerization was stable. In fact, the voltammograms of the electropolymerization resembled those of NMP polymerization (Figure 3-2a and Figure 3-3). Initial scans only showed double layer capacitance current until a potential of +0.60 V, (E_{onset}), was reached, where a rapid increase in current was observed, indicative of rapid oxidation of Py and subsequent polymerization. Hysteresis was observed, as is common in these processes, reflecting the autocatalytic nature of the electropolymerization reaction. Deposition of a conducting species onto the GC electrode was evident from the shallow shoulders at +0.15 V (Figure 3-2a), indicative of the doping process of the PPy films. As the number of polymerization cycles increased, a negative shift of E_{onset} was observed, consistent with the conducting nature of the polymer film. At the same time, an

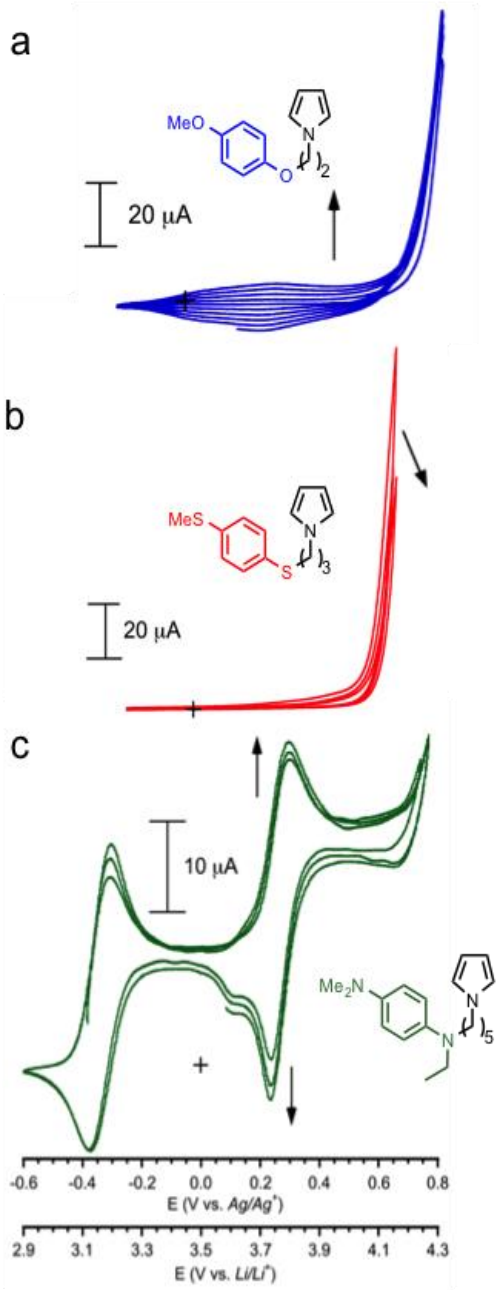

Figure 3-2. (a) Electropolymerization CV of 1a at 20 mV/s. (b) Attempt to electropolymerize 2a at a 20 mM monomer concentration in 0.1 M TBAP of MeCN at 20 mV/s. (c) Electropolymerization CV of 3c. 1a and 3c were polymerized from a 10 mM solution of monomer in 0.1 M TBAP in MeCN at 20 mV/s for various cycles.

increase in the double layer capacitance, between 0.0 and +0.2 V, was also evident as the doping level increased.

The electropolymerization of **3a-c** exhibited a different behavior as the polymerization process occurs after the oxidation of the RAP. The electropolymerization scan of **3c** (Figure 3-2c**)**, exhibits two redox peaks at -0.36 V and +0.23 V, respectively, which occurred before the oxidation of the Py backbone. Monomer **3c**, the heaviest monomer among **3a-c**, was predicted to be the most stable monomer towards electropolymerization because it had the lowest local charge density as a triply charged cation. The abrupt rise in current at +0.70 V was a clear indication of the stable oxidation of **3c** and its subsequent electropolymerization. Such a sharp rise in current was not observed for **3a** or **3b** with trimethylene- and tetramethylene-chains (Figure 3-4), respectively, ostensibly due to the high charge localization of these multiply charged radicals. Nevertheless, deposition of **3a** and **3b** on the glassy carbon (GC) electrode surface was evident from the increase in double layer capacitance and by the coating of a shiny blue film on the GC surface. CV characterization indicated the presence of ca. 10–20 monolayers of polymers (estimated from the charge of the first redox in the first cycles in Figure 3-5).

In fact, the effect of varying the length of the alkyl linkers in stabilizing the polymerization process was also evident in scan rate and solvent-dependent studies of the electropolymerizations of **3a-c**. While **3c** could be electropolymerized at 20 mV/s, **3b** required a sweep rate of 50 mV/s to achieve film deposition. In addition to the faster sweep rate, **3a** required use of the stabilizing, non-nucleophilic solvent, $PhNO_2$, in order to stabilize the triply charged species (Figure 3-4). While

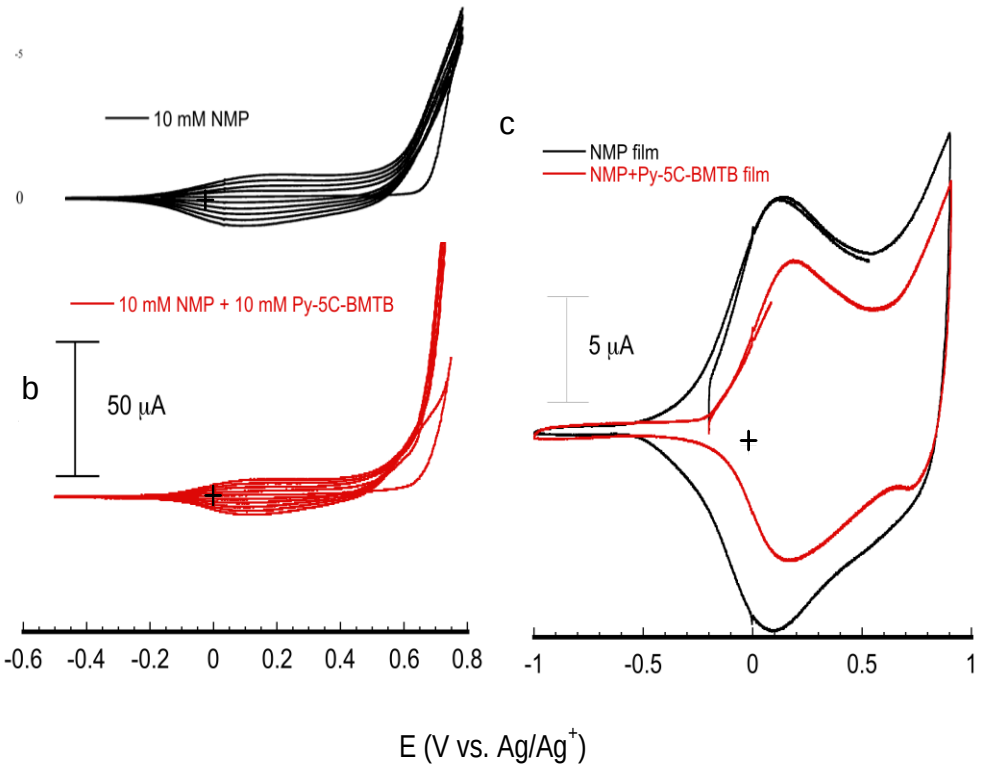

Figure 3-3. Comparison of electropolymerization of Py alone and in the presence of an equimolar concentration of **2c**. a) and b) show the electropolymerization of N-methylpyrrole (NMP) alone and in the presence of **2c**, respectively, and c) shows the CV of the resulting composites with background taken into account. Supporting electrolyte is 0.1 M TBAP/MeCN and scan rate is 20 mV/s for a, b and c. In the presence of **2c**, NMP retains its ability to electropolymerize. This behavior is opposite to that of monomers **2a-c** which exhibited a complete shut down of the electropolymerization. The resulting films exhibitedd very similar CV profiles, and the difference in the resulting films can be ascribed to variations in electropolymerization conditions from film to film.

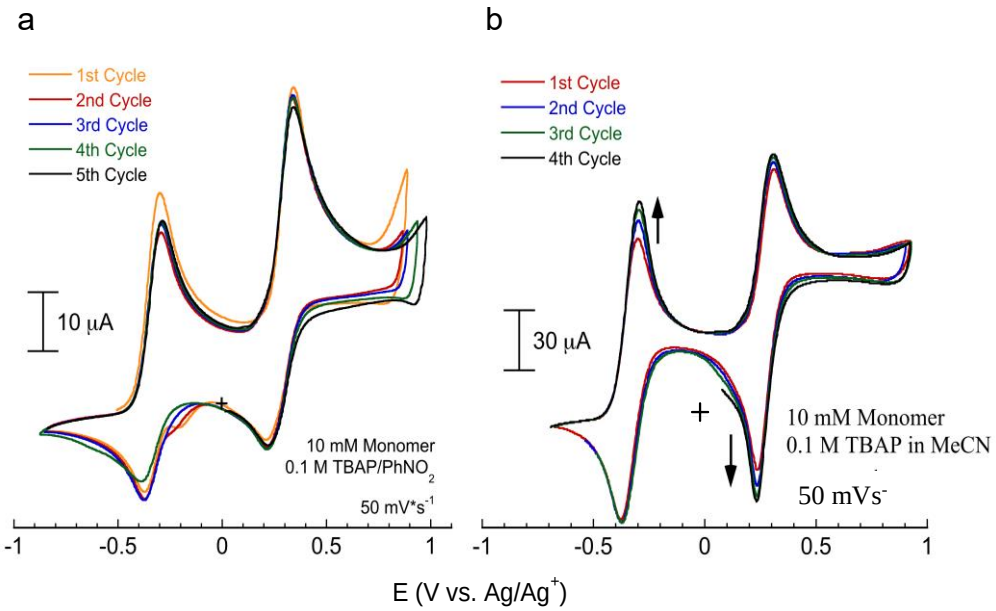

Figure 3-4. Electropolymerization of **3a** (a) and **3b** (b). As the alkyl chain becomes shorter (3C in **3a** and 4C in **3b**), the electropolymerization conditions become more demanding. **3b** was electropolymerized at 50 mV/s, a faster scan rate than for **3c**, and **3a** was electropolymerized at 50 mV/s in $PhNO_2$, a stabilizing and non-nucleophilic solvent.

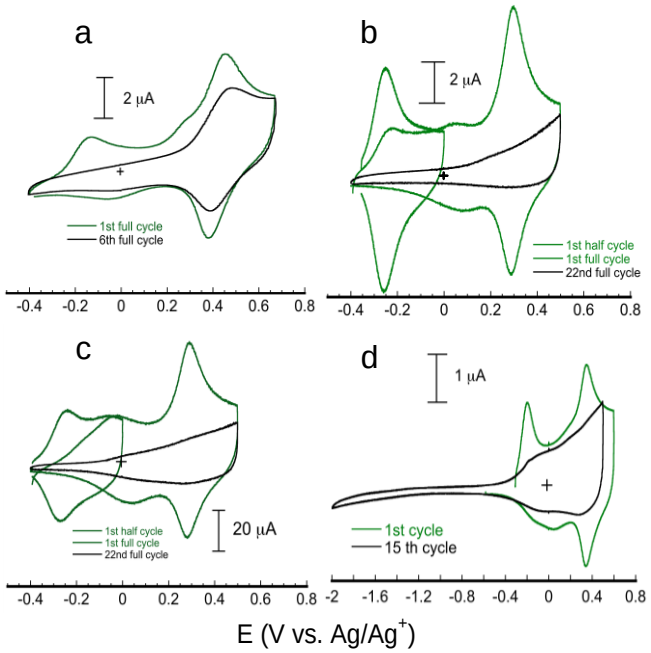

Figure 3-5. Cyclic voltammetric sweeps of electrochemically synthesized films, **3a-c** (a, b and c, respectively). The figure shows the first half and full cycles, and the 22nd full cycle for **3b** and **c** (b and c); and the first and the 6th full cycles of **3a** (a). d) Extended (15 cycles) cycling (-1.5 V – 0.6 V) of a polymer film of **3c**. Cycling of **3b** and **c** were performed in 0.1 M TBAP/MeCN and **3a** was in 0.1 M TBAP/$PhNO_2$, all at 20 mV/s.

electropolymerization of **3c** could be monitored by the increase of the pseudocapacitance, **3a** exhibited a less uniform/regular pattern as the number of cycles increased, possibly due to changes in ion transport and radicals at the interface of the polymer and electrode. However, all three monomers **3a-c** could be electropolymerized by CV, and they demonstrated the importance of decreasing charge density during the polymerization process in which the monomer with the longest alkyl linker, **3c**, displayed the prototypical electropolymerization behavior.

Monomers **4a-b** were expected to exhibit similar electropolymerization behavior to **3a-c**. The electropolymerization CVs of **4a** and **4b** showed the oxidation of the TMB moiety (Figure 3-6). The lack of an abrupt increase in current at high potentials (> 0.9 V) is believed to be due to high local charge density as for **3a** and **3b**. In fact, **4a** and **4b** have to become quadruply charged in order to generate the Py cation radicals, which then couple with each other to propagate the polymerization process. The high charge densities associated with these electropolymerization processes led to equally thin film deposition (ca. 20 monolayers, estimated from the integrated charge of the first redox couple in the first cycles in Figure 3-6).

The different electropolymerization behaviors of **1a-d** and **3a-c** were evident in their surface morphologies as well. Scanning electron microscopy (SEM) images of poly-**1a** (Figure 3-7) exhibited the surface morphology of a uniform film composed of small spheres of approximately 100 nm in diameter. On the other hand, poly-**3b** showed a much less homogeneous surface morphology composed of clusters. The uniform morphology of poly-**1a** could be due to the steady electropolymerization and subsequent deposition processes. This closely resembles the behavior of PPy, as the

polymerization of both pyrrole and **1a** involves singly charged cation radicals, which leads to similar morphologies.[23] However, the deposition of poly-**3b,** on the electrode surface, likely depends on the growth/generation of nucleation sites on the electrode surface since the electropolymerization process was less stable and involved multiply charged cation radicals of **3b**.[24-26] During the polymerization process, as **3b** gradually becomes more oxidized, the increasing repulsion between the electrode surface and +3 monomers could prevent all but a small fraction of the monomers from achieving the +3 state in the vicinity of the electrode surface. (Recall that that electropolymerization process takes place at applied potentials that are well positive of the point of zero charge for GCE, so the electrode surface is net positive). Once coupled with poly-**3b** strands nucleated on the electrode surface, the polymerization process would be more likely to continue and expand on that nucleation site since +3 monomers would experience less repulsion than at the electrode surface. This process of electropolymerization, based on nucleation, results in an aggregating morphology for poly-**3b** that is distinct from the morphology of poly-**1a**. Surface morphology also suggests the stability of polymerization of the monomers.

While **1a-d**, **3a-c** and **4a-b** were shown to be electropolymerizable, we were unable to establish conditions to electropolymerize **2a-c**. Following the rise in the current at +0.6 V, often indicative of Py coupling, no growth in double layer capacitance was observed (Figure 3-2b). Moreover, on subsequent cycles, E_{onset} shifted to more positive potentials, indicating the formation of an insulating film, rather than a conducting layer. Possible modes of failure were explored experimentally. The

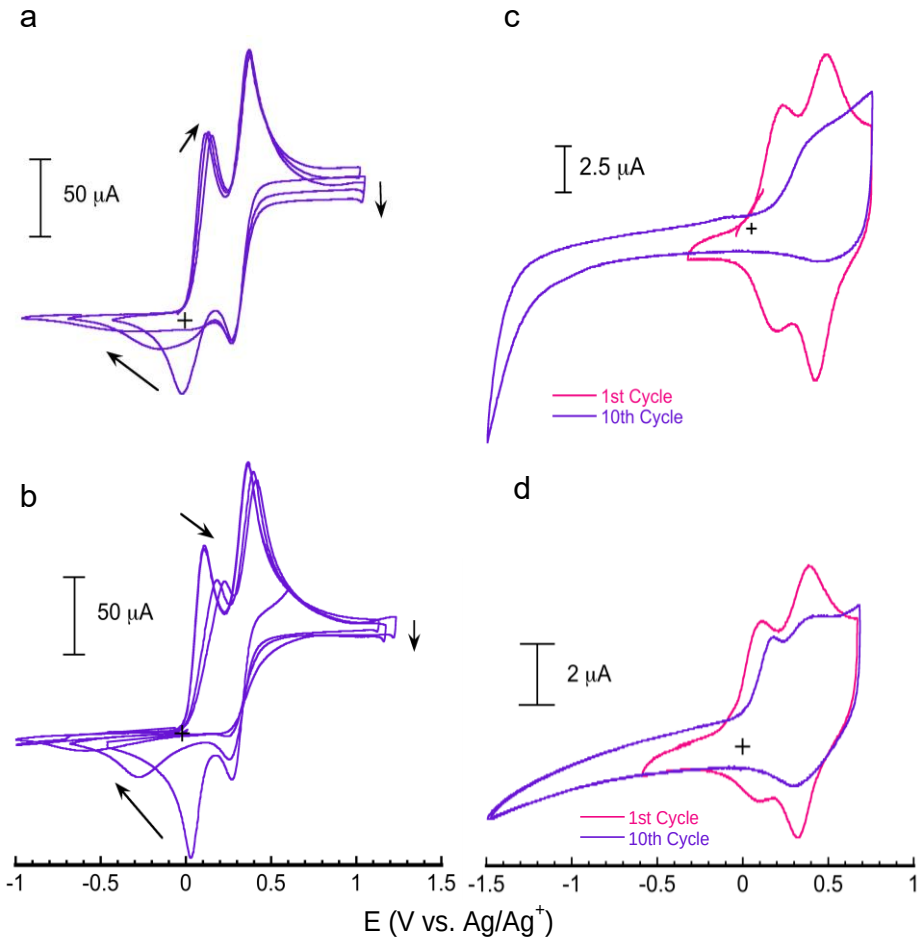

Figure 3-6. Cyclic voltammograms of electropolymerization of **4a-b** (a and b) and of poly-**4a-b** (c and d) excluding the effect of charge trapping by cycling to – 1.5 V. Supporting electrolyte is 0.1 M TBAP/MeCN and scan rate is 20 mV/s for a – d.

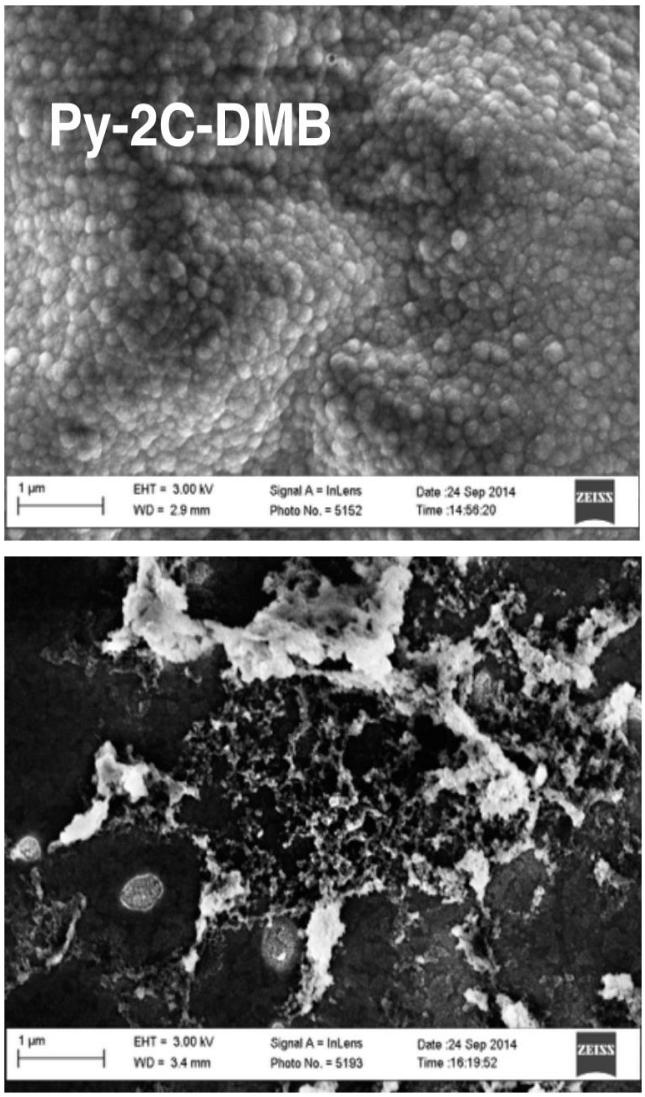

Figure 3-7. SEM images of poly-**1a** (a) and poly-**3b** (b)**.** Poly-**1a** exhibits a grain-like, morphology with spherical modules, while poly-**3b** shows the morphology of an aggregate. This could be due to the relative stability of electropolymerization. For cases in which the electropolymerization is more stable, as for **1a**, the surface morphology of the polymer is homogeneous across the surface of the electrode. For cases in which the electropolymerization is less stable, as for **3b**, the polymer appears to grow on nucleation sites and/or extending on existing chains/aggregates.

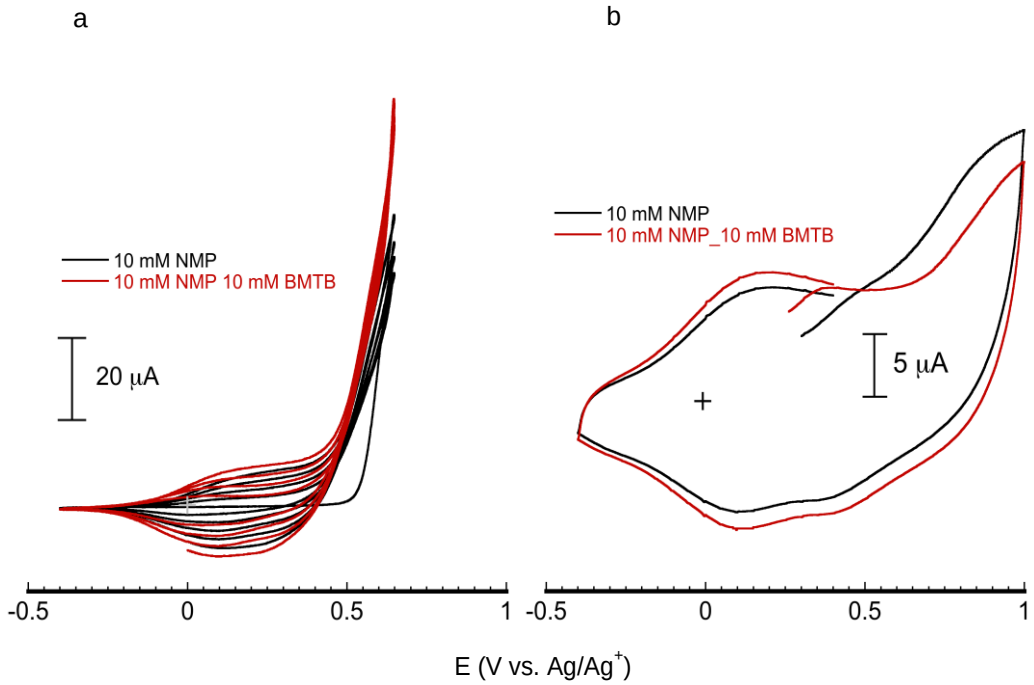

Figure 3-8. Electropolymerization of NMP in the presence of an equimolar concentration of BMTB in solution (a) and CV of the resulting films (b). As the resulting films show, there do not appear to be significant differences between films polymerized with NMP alone or in the presence of BMTB in solution. Supporting electrolyte is 0.1 M TBAP/MeCN and scan rate is 20 mV/s for both CVs.

possibility that the RAP, BMTB, inhibited the polymerization of Py was eliminated by the polymerization of NMP in the presence of an equi-molar concentration of BMTB (Figure 3-8). No significant differences were observed in either the polymerization or the CV of the resulting polymer composites when polymerized in the absence or presence of BMTB. The possibility of inhibition by an oxidized monomer cation radical was studied as well. The electropolymerization of NMP in the presence of an equimolar amount of **2a** did not affect polyNMP film formation (Figure 3-3). The electropolymerization CVs (Figure 3-3a. b) showed that while the current was higher in the solution with **2a**, the difference in current between polyNMP synthesized in NMP alone and NMP + **2a** was well within experimental error (±2 μA). This indicates that $\mathbf{2a}^{+2}$ does not significantly impede Py polymerization and that the ineffective and insulating coupling is intrinsic to **2a-c**.

3-4. Electrochemical Characterization of PPy-nC-RAP Polymer Films

After electropolymerization, the newly prepared polymer films were characterized electrochemically via CV in a 0.1 M tetrabutylammonium perchlorate (TBAP) in acetonitrile (MeCN) supporting electrolyte solution. Remarkably, all polymers generally exhibited voltammograms typical of pseudocapacitive polymer films. When the potential was swept between – 0.4 and +1.2 V for poly-**1a**, for example, a significant pseudocapacitance was observed (Figure 3-9a) between 0.0 and 0.7 V, before the onset of pendant oxidation. This pseudocapacitance is attributed to doping of the PPy with ClO_4^-. The films were characterized as synthesized, without the addition of common conducting additives (e.g. carbon black) or binder (e.g.

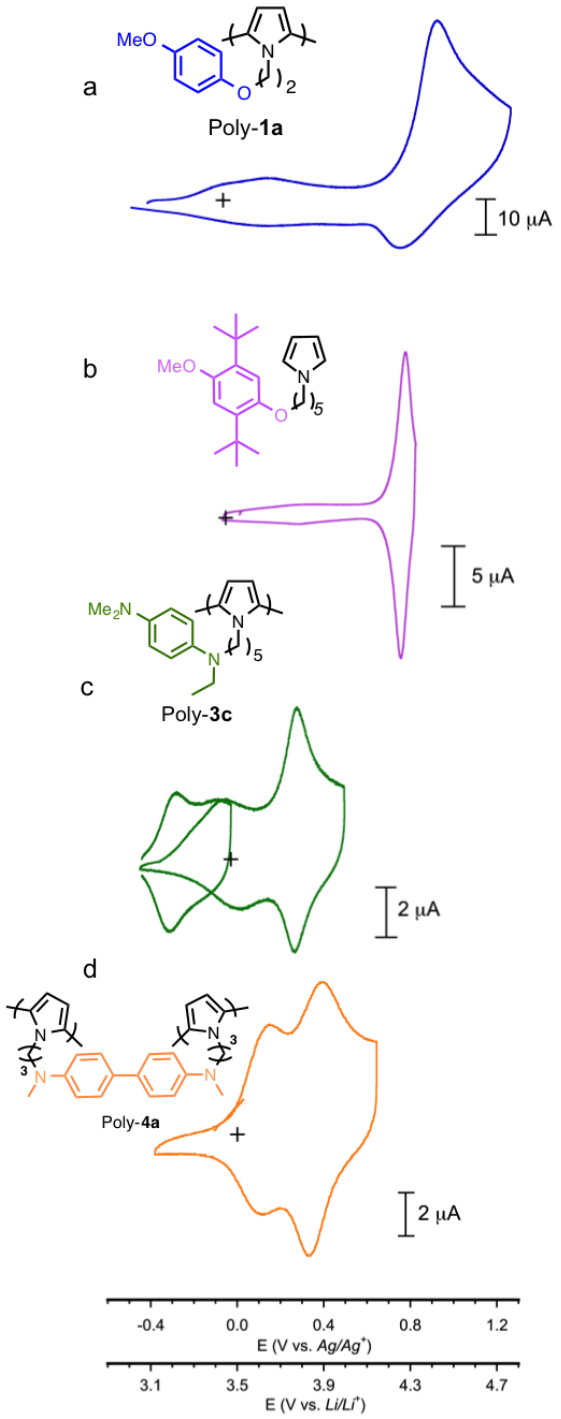

Figure 3-9 The first cycle cyclic voltammograms of polymer films of 1a (a), poly(Py-5C-dtbDMB) (b), 3c (c) and 4a (d) in 0.1 M TBAP/MeCN. Scan rate is 20 mV/s for 1a and 3c, and 50 mV/s for 4a.

polyvinylidene fluoride (PVDF)). The facile synthesis, lack of need of conducting additives, greatly improved theoretical capacities and working voltages of these polymers, making them promising candidates for use in electrical energy storage devices. As the potential was swept past the oxidation of the DMB pendants in poly-**1a-d**, large currents were usually observed at the E_{ox} of the pendants (+0.9 V), followed by diminished reduction currents, indicating chemical irreversibility of the oxidized DMB pendant in the polymer films. No oxidative current was observed for poly-**1a-d** positive of +0.8 V in the second cycle except for the pseudocapacitance contributed by PPy. The loss of redox activity positive of +0.8 V is indicative of a coupled chemical step upon oxidation of the DMB pendant (Figure 3-9a). As soon as the radical cation is formed, the highly electrophilic DMB-radical becomes susceptible to (nucleophilic) attack by reactive species such as acetonitrile and trace water in solution, leading to non-redox active byproducts.

In order to retain the reversibility of the redox process from the RAP, we implemented the use of *tert*-butyl substituents as protecting groups on the DMB-ring to mitigate/preclude side reactions.[27] The symmetric voltammogram of poly-(Py-5C-dtbDMB) at +0.8 V (Figure 3-9b) is confirmation of the structural-stability relationship of *tert*-butyl groups on DMB. Hence, the use of *tert*-butyl groups to mitigate the chemical instability of the DMB-cation radical confirms that the radical cation is likely responsible, as least in part, for the unwanted reactions of poly-**1a-d**. However, the chemical stability in poly-(Py-5C-dtbDMB) comes at the expense of a decreased theoretical capacity due to the increase in mass of the monomer unit (108 mAh/g, assuming 1.5 e^- per repeating unit).

On the other hand, the most promising electrochemical behaviors were observed for poly-**3a-c** and poly-**4a-b**, which exhibited two one-electron reversible waves. Poly-**4a-b** showed two one-electron reversible waves at +0.15 V and +0.40 V with small ΔE_p values (Figure 3-1b, 3-9d). The $E^{0'}$ values of the redox couples of the polymers are slightly negative of TMB, because the alkyl chain and Py donate their electron density toward the pendant rendering the oxidation process more facile.

Poly-**3a-c** represents the most promising class of polymers in this study due to their higher energy density and theoretical capacity relative to poly-**4a-b**. The symmetric redox processes at -0.25 and +0.28 V correspond to the redox processes from the TMPD pendant (Figure 3-9c). The overall shape of the two one-electron redox waves of poly-**3c** is consistent with the redox processes of TMPD. The peak potentials (E_p) of the two redox couples were slightly more negative than those of TMPD, likely due to donation of electron density from the alkyl chains and Py. At -0.40 V, where the polymer composite is ostensibly neutral, the small current observed is attributed purely to the double layer capacitance from the PPy backbone. At 0.00 V, the double layer capacitance dramatically increased because the composite becomes singly charged, and as expected, at +0.50 V, the current is further enhanced due to the doubly charged composite. These electrochemical properties of poly-**3a-c** make them the most promising class of molecules in this family, and also validate our design criteria for organic EES materials.

While these materials exhibit many promising electrochemical properties, poly-**3a-c** and poly-**4a-b** are limited by severe capacity fading caused by "charge trapping" of the RAP. In classic studies by Murray and coworkers,[28, 29] charge trapping

3rd cycle:
Area = 0.00141 A•V / 0.02 V/s = 0.0705 C

2nd cycle:
Area = 0.000231 A•V / 0.02 V/s = 0.0115 C

% Charge Recovered:
(0.0705 – 0.0115) / 0.0705 = 84 %

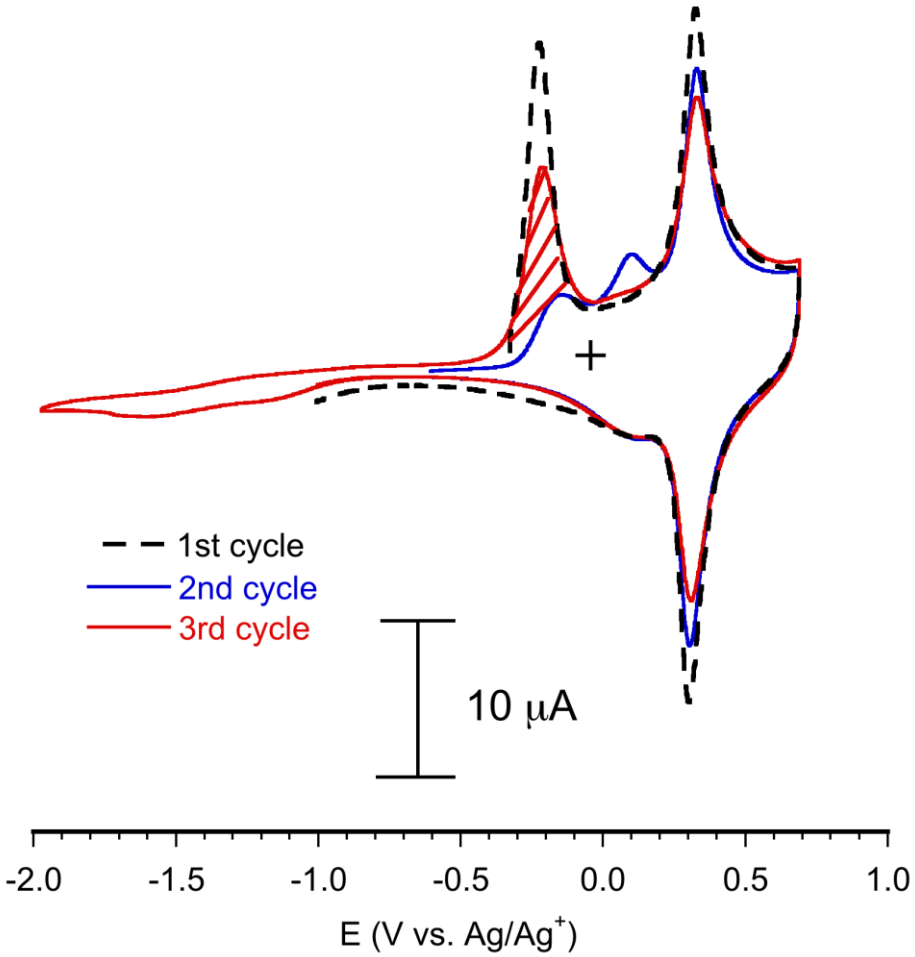

Figure 3-10. Charge trapping phenomena observed in a polymer film of 3c in 0.1 M TBAP/MeCN at 20 mV/s. The diminished amplitude of the first oxidation of the film, on the second cycle, is recovered after scanning the potential to – 2.0 V.

in multilayer thin film materials was observed when insulating domains were present in the film assembly. A similar trapping phenomenon was also observed when poly-**3a-c** was in their charged state. In the first cycle (Figure 3-10), two oxidations were observed. However, in the reverse scan, only the reduction associated with the second oxidation (ca. +0.30 V, Figure 3-10) was observed, which indicated incomplete reduction of the thin film assembly. When the potential sweep was reversed at -0.6 V, the first oxidation was dramatically diminished on the second full cycle (2^{nd} cycle, Figure 3-10) while the second redox wave remained unchanged. The hypothesis that insulating domains exist in the polymer films is also supported by the small oxidation peak in the 2^{nd} cycle near +0.1 V. The insulating domains in the films that were not oxidized in the first cycle (not electronically accessible) might gain some electronic accessibility after the 1^{st} cycle, possibly due to polymer, ion and solvent movement during cycling. As a result, the formerly insulating domains became somewhat electronically accessible and were oxidized, albeit at overpotentials of about 300 mV. Fortunately, the effect of charge trapping is reversible. While the polymers are "trapped" in their +1 state until at least -1.5 V, cycling to more negative potentials gave rise to a recovery of the first oxidation peak (3^{rd} cycle on Figure 3-10). The shallow peaks that appeared in the -1.1 to -1.5 V range suggest the complete reduction of the polymer film, and in the subsequent full cycle, about 84 % of the charge was recovered for the redox couple at ca. -0.25 V and both oxidation processes were observed (see Figure 3-10 for sample calculation). Such a high negative overpotential appears to be necessary to completely reduce the polymers back to neutral and ostensibly expel ClO_4^- anions from the film.

The immediate deleterious effect of charge trapping in a material for EES applications is the loss of energy density during discharge. Since the charge trapping occurs during discharge, decrease of the discharge potential scales linearly with the energy density of an electrode, as energy density is calculated by

$$E = V \times C \quad (1)$$

where E is energy density, V is working voltage and C is capacity. A lower discharge potential would result in a concomitant decrease in the energy density, which would be detrimental to any EES application.

While the mechanisms of charge trapping are still under investigation, we have found that the phenomenon is not specific to the identity of the electrolyte nor the molecular structure of the doubly-charged RAP. CVs of poly-**3c** films still exhibited charge trapping in tetrabutylammonium tetrafluoroborate and tetrabutylammonium hexaflorophosphate (Figure 3-11). In both cases, potentials more negative than -1.5 V were required in order to recover the redox activity of the film. Similarly, poly-**4a-b** also exhibited charge trapping and required high negative potentials to completely reduce the polymer (Figures 3-12). Thus, while these results suggest that charge trapping is not specific to the electrolyte, the *N*-containing and highly charged redox-active centers might be especially sensitive to charge trapping.

Other than charge trapping, the capacity fade of poly-**3a-c**, **4a-b** can also be attributed, at least in part, to partial dissolution of the polymer into the electrolyte solution as well as to side reactions involved at the very negative potentials (≥ - 1.5 V) applied during un-trapping. In Figure 3-5d, the capacities decreased as the poly-**3a-c** films were cycled. When cycling poly-**3a-3c** between -0.4 – +0.5 V, the loss in

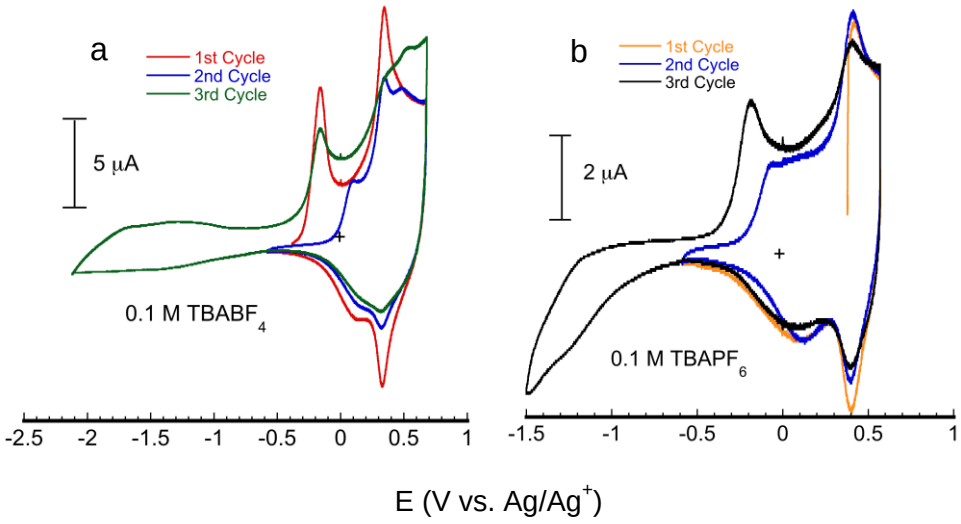

Figure 3-11. CV of poly-**3c** films in tetrabutylammonium tetrafloroborate ($TBABF_4$) (a) and tetrabutylammonium hexaflorophosphate ($TBAPF_6$) (b) at 20 mV/s. As shown in a and b, charge trapping persists even with different supporting electrolyte anions, as 3rd cycle, in which the film was un-trapped (cycled to $E \leq$ -1.5 V), in both a and b showed more prominent oxidation of the polymer than the 2nd cycle.

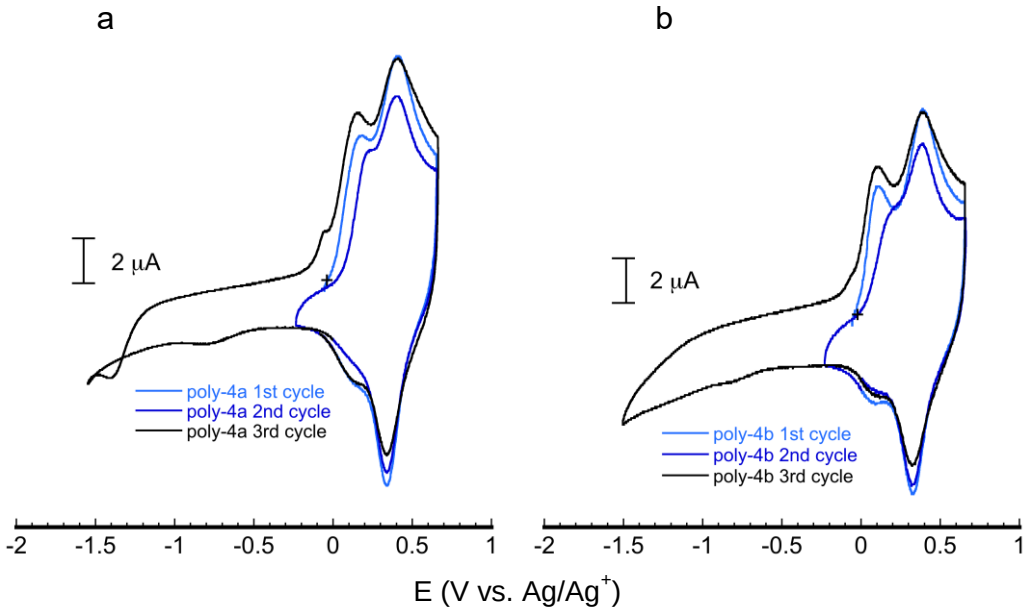

Figure 3-12. Cyclic voltammograms of poly-**4a** (a) and poly-**4b** (b) in 0.1 M TBAP/MeCN at 50 mV/s, showing the effect of charge trapping. Supporting electrolyte is 0.1 M TBAP/MeCN.

capacity was assumed to be largely due to charge trapping, since the polymer is expected to be chemically stable over this potential range. However, when cycling between +0.6 V and un-trapping potentials (-1.5 V – +0.6 V, Figure 3-5d), the capacities of the composites still diminished, though at a much slower rate. The loss of capacity from the first cycle to the 15th cycle in **3a-c** could be due to other factors. One possibility is dissolution of low molecular weight oligomeric chains of the polymer composites from the GC surface into the electrolyte solution, and the other is side reactions occurring during un-trapping. The small decrease in the double layer capacitance at 0.0 V in Figure 3-5d suggests contributions from dissolution, while the absence of any redox couples typical of TMPD or TMB suggests that side reactions likely occurred during cycling.

3-5. Conclusion

A new class of materials has been designed and investigated for use in EES applications. Monomers containing a polymerizable pyrrole and a redox-active pendant connected through an alkyl chain of variable length were synthesized and subsequently electropolymerized via CV. The best electropolymerization stability was observed when Py polymerization took place before pendant oxidation (**1a-d**). For monomers whose pendants oxidized prior to the oxidation of Py (**3a-c** and **4a-b**), a minimum alkyl chain length of trimethylene units was required for successful electropolymerization. Sample preparation via CV affords uniform and controlled films for electrochemical and morphological characterization. The electrochemical characterization of the polymer films, without conducting additives, suggests that, for O-containing RAPs (**1a-d**), greater chemical stability is found with hindered O-

pendants. The doubly charged *N*-containing RAPs, while exhibiting two reversible one-electron redox processes, have a tendency to undergo charge trapping, which leads to the rapid capacity fade of films of poly-**3a-c** and **4a-b**. To further improve the performance of these hybrid organic systems, we are currently investigating more robust and light-weight materials and we feel confident that this work and our on-going investigations will lead to organic cathode materials with dramatically higher energy densities and long term stability.

REFERENCES

1. A. S. Aricò, P. Bruce, B. Scrosati, J.-M. Tarascon and W. van Schalkwijk, *Nature Materials*, 2005, **4**, 366.
2. K. Nakahara, J. Iriyama, S. Iwasa, M. Suguro, M. Satoh and E. J. Cairns, *Journal of Power Sources*, 2007, **165**, 870-873.
3. A. A. Golriz, T. Kaule, M. B. Untch, K. Kolman, R. Berger and J. S. Gutmann, *ACS Applied Materials & Interfaces*, 2013, **5**, 2485-2494.
4. K. Motokuni, B. Häupler, R. Burges, D. Hager Martin and S. Schubert Ulrich, *Journal of Polymer Science Part A: Polymer Chemistry*, 2016, **54**, 2184-2190.
5. *Journal of Power Sources*, 2013, **242**, 33.
6. K. Koshika, N. Chikushi, N. Sano, K. Oyaizu and H. Nishide, *Green Chemistry*, 2010, **12**, 1573-1575.
7. Y. Liang, Z. Tao and J. Chen, *Advanced Energy Materials*, 2012, **2**, 742-769.
8. K. Nakahara, S. Iwasa, M. Satoh, Y. Morioka, J. Iriyama, M. Suguro and E. Hasegawa, *Chemical Physics Letters*, 2002, **359**, 351-354.
9. S. Yoshihara, H. Katsuta, H. Isozumi, M. Kasai, K. Oyaizu and H. Nishide, *Journal of Power Sources*, 2011, **196**, 7806-7811.
10. J.-K. Kim, G. Cheruvally, J.-W. Choi, J.-H. Ahn, S. H. Lee, D. S. Choi and C. E. Song, *Solid State Ionics*, 2007, **178**, 1546-1551.
11. H. Shirakawa, E. J. Louis, A. G. MacDiarmid, C. K. Chiang and A. J. Heeger, *Journal of the Chemical Society, Chemical Communications*, 1977, 578-580.
12. N. Mermilliod, J. Tanguy and F. Petiot, *Journal of The Electrochemical Society*, 1986, **133**, 1073-1079.
13. N. Oyama, T. Tatsuma, T. Sato and T. Sotomura, *Nature*, 1995, **373**, 598.
14. R. Bittihn, G. Ely, F. Woeffler, H. Münstedt, H. Naarmann and D. Naegele, 1987.
15. P. Novák, K. Müller, K. S. V. Santhanam and O. Haas, *Chemical Reviews*, 1997, **97**, 207-282.

16. G. MacDiarmid Alan, *Angewandte Chemie International Edition*, 2001, **40**, 2581-2590.
17. S. Conte, G. G. Rodriguez-Calero, S. E. Burkhardt, M. A. Lowe and H. D. Abruna, *RSC Advances*, 2013, **3**, 1957-1964.
18. M. A. Lowe, Y. Kiya, J. C. Henderson and H. D. Abruña, *Electrochemistry Communications*, 2011, **13**, 462-465.
19. L. Nyholm, G. Nyström, A. Mihranyan and M. Strømme, *Advanced Materials*, 2011, **23**, 3751-3769.
20. T.-T. Truong, G. W. Coates and H. D. Abruna, *Chemical Communications*, 2015, **51**, 14674-14677.
21. X. Huang, K. W. Anderson, D. Zim, L. Jiang, A. Klapars and S. L. Buchwald, *Journal of the American Chemical Society*, 2003, **125**, 6653-6655.
22. B. P. Fors, D. A. Watson, M. R. Biscoe and S. L. Buchwald, *Journal of the American Chemical Society*, 2008, **130**, 13552-13554.
23. E. De Giglio, M. R. Guascito, L. Sabbatini and G. Zambonin, *Biomaterials*, 2001, **22**, 2609-2616.
24. M. González-Tejera, I. C. Ramiro and I. Hernández-Fuentes, *Electrochimica acta*, 2000, **45**, 1973-1982.
25. İ. H. Kaplan, K. Dağcı and M. Alanyalıoğlu, *Electroanalysis*, 2010, **22**, 2694-2701.
26. J. Lukkari, R. Tuomala, S. Ristimäki and J. Kankare, *Synthetic metals*, 1992, **47**, 217-231.
27. L. M. Moshurchak, C. Buhrmester and J. R. Dahn, *Journal of The Electrochemical Society*, 2005, **152**, A1279-A1282.
28. H. D. Abruña, P. Denisevich, M. Umana, T. J. Meyer and R. W. Murray, *Journal of the American Chemical Society*, 1981, **103**, 1-5.
29. P. Denisevich, H. Abruna, C. Leidner, T. Meyer and R. W. Murray, *Inorganic Chemistry*, 1982, **21**, 2153-2161.

SUPPORTING INFORMATION

Electrochemical Measurements

General Procedures for Electrochemical Measurements. All electrochemical measurements, unless otherwise noted, were performed in a three-compartment fritted glass cell using a three-electrode configuration. A Pt wire was used as the counter electrode, the reference electrode was a homemade Ag/Ag^+ (with 0.05 M $AgClO_4$ in 0.1 M TBAP in MeCN solution inside the electrode and immersed in 0.1 M TBAP in acetonitrile (MeCN) solution) and a homemade glassy carbon electrode (3 mm diameter) was used as the working electrode. The working electrodes were electrochemically cleaned by cycling between – 2.0 V – 1.0 V (vs. Ag/AgCl) for 10 cycles in 0.5 M KOH solution, and subsequently mechanically cleaned with alumina/water slurry, 1.0 μm, 0.3 μm and 0.05, in this order, and then rinsed clean with DI water.

Electropolymerization Parameters of 1a-d and 3a-c. Electropolymerization of **1a-d** and **3a-c** was carried out via cyclic voltammetry. The electropolymerization solution contained 10 mM concentration of monomer in 0.1 M TBAP/MeCN. The potential was cycled at 20 mV/s for a specified number of cycles depending on the desired coverage. The potential range and number of cycles are presented in **Table 3-S1**. The substrate and deposition time are reported in **Table 3-S2**.

Table 3-S1. Electropolymerization Parameters for monomers **1a-d**, **2a-c** and **3a-c** on glassy carbon (GC) electrodes

Monomer	**Reversing *E* (V vs. Ag/Ag^+)**	**Number of cycles/Time**
1b	- 0.40 – 0.75	5
1c	- 0.40 – 0.75	5
1d	- 0.40 – 0.75	5
2a	- 0.30 – 0.65	
2b	- 0.30 – 0.65	N/A
2c	- 0.30 – 0.65	
3a	- 0.60 – 1.20	3
3b	- 0.60 – 0.90	3
3c	- 0.60 – 0.85	3
4a	-1.00 – 1.20	3
4b	-1.00 – 1.20	3
5 (CV)	-0.30 – 0.65	5
5 (Potential Step)	0.67	5 mins

[a]**2a-c** did not electropolymerize under these conditions.

Table 3-S2. Synthesis parameters of polymers **1a-d** and **3a-c** on Indium Tin Oxide (ITO) electrodes for Scanning Electron Microscopy (SEM) characterization

Monomer	Application	Substrate	Deposition Method	Potential Range (V vs. Ag/Ag^+)	Number of Cycles
1a-d	SEM	ITO	CV	- 0.30 – 0.75	5
3a-c				- 0.60 – 0.90	3

Electrochemical Characterization

All electrochemical measurements, unless otherwise noted, were performed in 0.1 M electrolyte solutions in the specified solvents. The electrolyte solution was purged with inert (N_2 or Ar) gas for at least 10 minutes before each experiment.

Instrumentation All manually controlled electropolymerization experiments were performed on a Hokuto Denko HABF1510m potentiostat/galvanostat. All the measurements were taken under anhydrous and inert conditions with a Princeton Applied Research VersaSTAT 3 potentiostat. For CV and chronoamperometry measurements, a BASi Epsilon-EC model potentiostat was used.

Scanning Electron Microscopy Polymer films prepared on ITO slides were synthesized as described above. After rinsing the polymer surfaces to completely remove extra oligomers and electrolyte, and drying of samples in vacuo overnight, SEM images of the polymer composites on ITO were taken with a voltage of 3 keV on a Zeiss 1550 FE-SEM electron microscope.

CHAPTER 4

AN ELECTROCHEMICAL INVESTIGATION OF CHARGE TRAPPING IN REDOX-ACTIVE POLYMERS

4-1. Introduction

Redox-active polymers are highly promising organic electrode materials for EESS, and have garnered much attention in the field. The previous chapter described a library of redox-active polymers. We employed an electronically conducting polymer, polypyrrole, as the polymer backbone, and four redox-active units as redox-active pendants and electropolymerized them into thin-film electro-active polymers. Among the polymers studied, PPy-5C-TMPD (Figure 4-2) was shown to have the most promising redox-active behavior as a potential cathode material. Because of its two chemically and electrochemically reversible redox couples at – 0.30 and 0.25 V vs. Li/Li^+.

However, PPy-5C-TMPD also exhibits a phenomenon that precludes it from becoming a practical cathode material. At the end of Chapter 3, we observed the CV of PPy-5C-TMPD, which exhibited two oxidations, about 500 mV apart, corresponding to the oxidation of the TMPD pendant. However, only one reduction wave centered at 0.3 V vs. Ag/Ag^+ was observed in the reverse scan. The reduction wave associated with the first oxidation was completely absent from the voltammogram. As a result, in the subsequent positive scan, the first oxidation was shown not evident, as the polymer was not completely reduced and remained in its +1 state, while the second redox couple remained with comparable magnitude to the initial scan. Subsequently, we found that, when a very large overpotential was applied

to the polymer at this stage, by scanning the potential to -2.5 V, shallow shoulders appeared at very low potentials, suggesting the expulsion of residual anions from the polymer film and returning it to its neutral form. As expected, in the subsequent cycle, the first oxidation was observed with a magnitude comparable to that in the first cycle. Such electrochemical behavior is termed “charge trapping”.

There are various types of “charge trapping” described in the literature and they all have somewhat different manifestations. For example, in semiconductors, such as quantum dots or TiO_2 which are important light absorbers, their ability to engage in light induced charge transfer events is their essential function.[1, 2] When light excites an electron in the valence band of a semiconductor, it creates an electron-hole pair. The electron can either get passed onto to a molecule, completing a charge transfer event, or it can recombine with the hole. Recombination of the electron and hole is not useful in photocatalysis as the energy is released as heat. Charge traps are electronic states within the band gap and can serve as efficient recombination sites. By trapping the electrons for a short a mount of time, the traps delay the immediately recombination of the electron and hole. In some cases, these charge carrier traps manifest themselves as defects between grains of crystals and those boundaries generally have slightly higher energy than the bulk crystal[2], making them a good place to “trap” the excited electrons. In reality, charge carrier traps work differently in different semiconductors in that they could be beneficial or detrimental to the catalytic cycle, but the idea is the same in that they are defect sites that are energetically within the band gap.

“Charge trapping” not only appears in inorganic semiconductors; it also

appears in organic semiconductors. Organic semiconductors can also exhibit charge trapping which is distinct from that in inorganic semiconductors. We will use the example of polythiophene, which is one of the most studied charge trapping case in conducting polymers.[3-5] Polythiophene has quite stable *p-doping* and *n-doping* regions, which is not very common in electronically conducting polymers. However, when the full potential window is swept from *undoped* to the full potential window, pre-peaks indicative of charge trapping will be observed. The observation of pre-peaks at these positions have been consistently observed and studied by many groups investigating conducting polymers, and researchers have come up with different causes for the charge trapping. Zotti has suggested that such behavior is not charge trapping, and that they are actual chemical modifications to the polythiophene chains due to trace impurities in the solution.[3] Others, such as Buttry[5], have observed that at charge trapping potentials, we expect expulsion of ions from the previous process, i.e. residual anion expulsion during pre-peak from *p-doping* state. However, contrary to expectation, they observed cation insertion during the cathodic pre-peak, instead of anion expulsion. Given that the film had residual anions, insertion of cations was very surprising since this occupied more volume. While the charge trapping events are well documented for polythiophene, their cause is still not clear. Researchers attribute charge trapping in polythiophene to low dielectric regions within the film, causing charge trapping and the presence of pre-peaks. While low dielectrics could explain the presence of pre-peak, it does not fully explain its effect on only one but not both of the pre-peaks and remains insufficient.

The final type of “charge trapping” is present in multilayer polymer film

assemblies, where outermost layer can be rendered accessible only when the inner layers are activated, and hence "trapping" charges of the outermost layer.[6] The simplest form of such multilayer polymer film assembles can be represented

Another type of "charge trapping" is present in multilayer polymer film assemblies. Where charge trapping is intentional by making multi-layer polymer assemblies that are engineered to trap charges. A rectifying bilayer is an assembly of at least two layers of different polymers that have mismatching redox potentials.[6] For example, a rectifying bilayer can have an inner layer that exhibit redox events at -1.25 and 1.5 V, and an outer layer that exhibit redox event at 0.75 V. As these are redox polymers and not conducting polymers, transport of electrons and ions are only allowed during redox events. As a result, when sweeping from 0.0 V to 0.75 V, no redox events can be accessed as the outer layer which oxidizes at 0.75 is physically separated from electrode contact, and that the assembly would not get oxidized until layer A is activated, which is at -1.5 and 1.25 V. At either of those potentials, layer B would also be redox active with significant overpotential, the kinetic of those two redox processes is really fast, resulting in adsorptive and desorptive voltammegrams. In a vague manner, rectifying bilayer is similar to semiconductor charge trapping in that a thermodynamic barrier manifests as the trap. However, a rectifying bilayer is also manufactured, and in most cases, charge trapping polymer films are not so deliberate.

From Chapter 3, we have a few clues regarding "charge trapping" phenomena. First, it is chemically reversible but electrochemically irreversible. As we mentioned, the charges trapped can be recovered (untrapped), corresponding to chemical

reversibility, but enormously large overpotentials are required, corresponding to

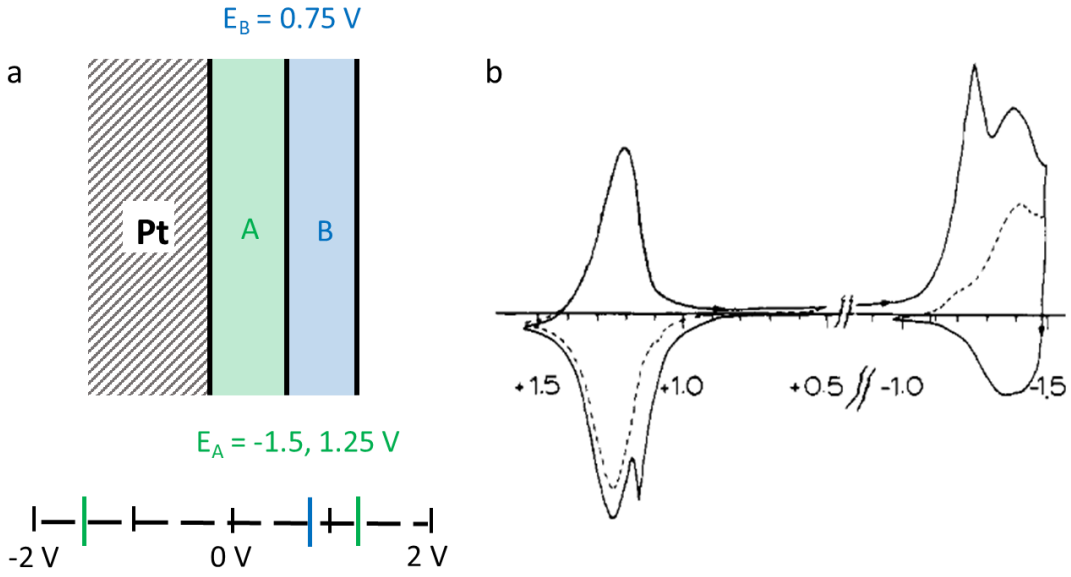

Figure 4-1. a) A rectifying multilayer polymer assembly. The inner layer has two redox potentials at – 1.5 and 1.25 V and the outer layer has a redox couple at 0.75 V, between those of the inner layer. b) The CV of this multilayer polymer assembly. Adapted from reference 6.

electrochemical irreversibility. Secondly, in Chapter 3 we showed that charge trapping is not specific to ion-pairing. We observed charge trapping with both perchlorate and hexafluorophosphate anions, suggesting that it is unlikely to be specific ion-pairing between TMPD and anions. Thirdly, charge trapping appears to occur in the first redox couple rather than the second redox couple.

In this chapter, based on the above indications, I will investigate, in detail the electrochemical basis for charge trapping in PPy-5C-TMPD. Specifically, I will seek any distinctions between electrochemical behaviors of the two redox couples, in an attempt to obtain more information regarding the electrochemical nature of the charge trapping processes. When compared to the various types of charge trapping described above, charge trapping in PPy-5C-TMPD is most similar to that described in polythiophene. As PPy-5C-TMPD undergoes redox behaviors, charge compensation by counter-ion incorporation is paramount, and we will use the method employed to study polythiophene charge trapping, to monitor that movement using the electrochemical quartz microbalance (EQCM) to monitor counter-ion movement and observe any deviations. As we obtained more information regarding the electrochemical nature of the charge trapping in PPy-5C-TMPD, measures were taken to avoid it and to realize the full potential of the conducting polymer redox-active polymer architecture for EESS applications.

4-2. Electrochemical Behavior of Charge Trapping in PPy-5C-TMPD

The disappearance of the reduction associated with the first oxidation (E_1) is peculiar, especially since the second redox couple (E_2) remains intact during cycling. The two redox couples were first separated by cycling each redox couple for 10 cycles

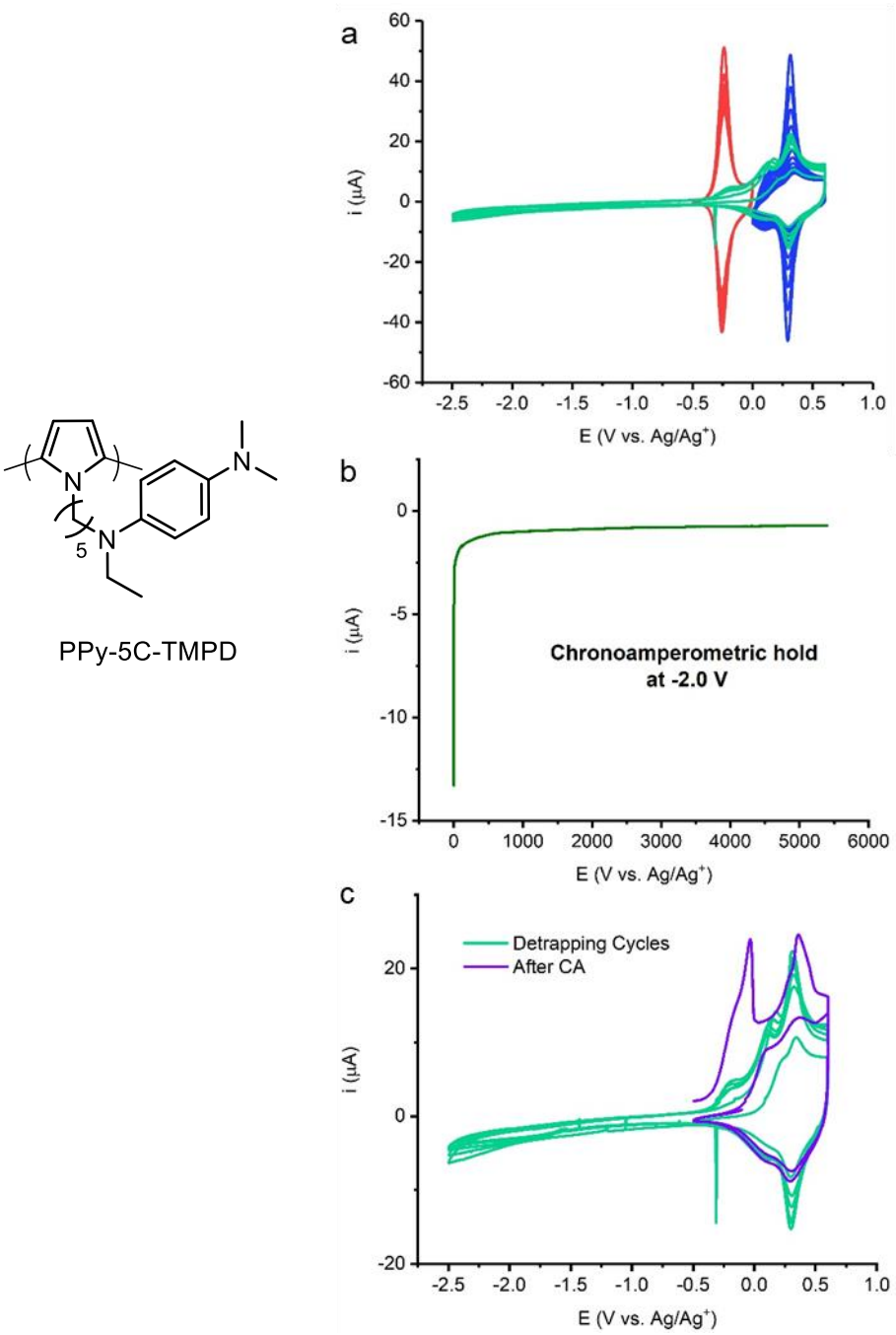

Figure 4-2 a) Separate cycling of E_1 and E_2 and the subsequent detrapping attempt. b) Extended chronoamperometric experiment at – 2.0 V to detrap PPy-5C-TMPD. c) Cycling of film immediately after extended chronoamperomety in b).

to determine if charge trapping was specific to only the first redox couple and not the second. As shown in Figure 4-2, cycling over E_1 alone for ten cycles gave rise to a gradual decrease in its peak current, i_{pk}. The decrease was much more severe upon cycling over E_2. The same effect is observed when using PF_6^- as the anion. This set of simple experiments unequivocally indicate that charge trapping is not specific to one of the redox couples, but occurs to both E_1 and E_2.

A decrease in i_{pk} could indicate either a) charge trapping occurs, or b) degradation/loss of polymer during cycling. The recovery of the trapped charges would confirm a and disprove b, and the opposite would also be true. Initial attempts to recover the trapped charges upon separate redox cycling failed. Upon scanning to -2.5 V, no charges were recovered in the subsequent scan, as no oxidation associated with E_1 was observed. While this seemingly confirms the validity of b, it is also worth pointing out that, by separately cycling E_1 and E_2 for ten cycles, significant amounts of time were spent at the charged states of the polymer. Such prolonged duration in the charged states could give rise to more severe charge trapping than the brief cycling in Figure 4-1a. Hence, prolong duration was also applied to the detrapping process, by chronoamperometry (CA) at – 2.0 V for almost 2 hours (Figure 4-2b). Charges were transiently recovered upon extended detrapping (Figure 4-2c). This result also

confirmed that by cycling longer over the charged states, PPy-5C-TMPD showed more severe charge trapping.

Based on the above observation, that charge trapping occured to both E_1 and E_2, and that the length of time PPy-5C-TMPD spent in its charged states was correlated with the severity of charge trapping, there must be a time-dependent component to the charge trapping process. To decouple the thernodymic and kinetic aspects of charge trapping, a simple scan rate dependence experiment was performed

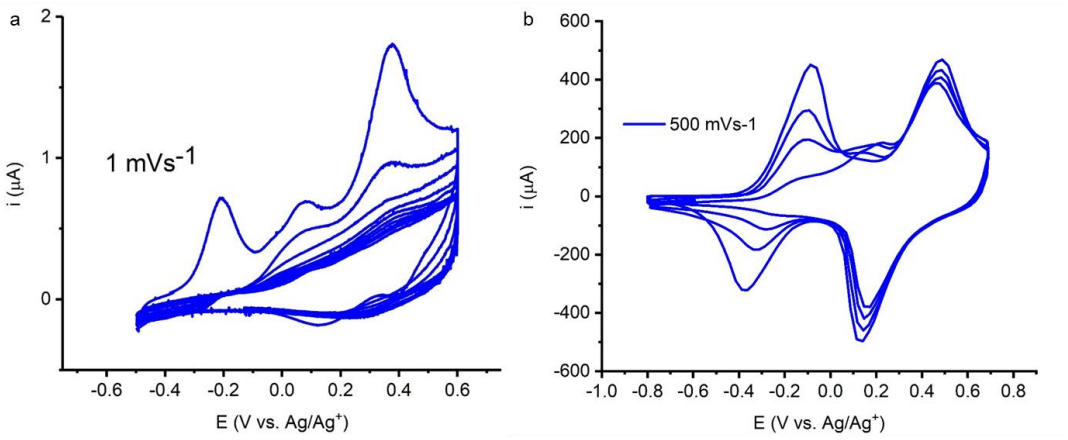

Figure 4-3. a) CV of PPy-5C-TMPD at 1 mVs^{-1}, and b) at 500 mVs^{-1}. All experiements were carried out in 0.1 M TBAP/MeCN.

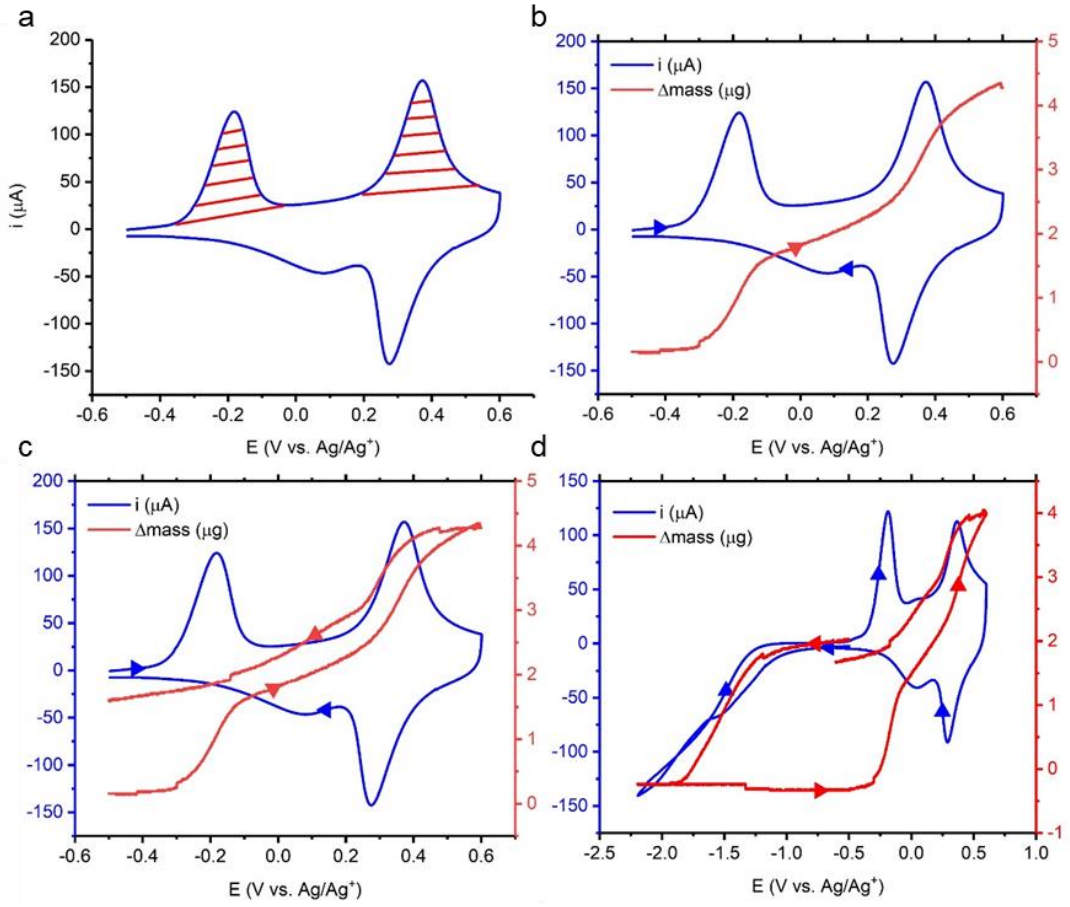

Figure 4-4. a) Area of oxidations taken to calculate charges involved. b) Mass variations during the two oxidations to calculate mass of anions involved. c) The difference in mass before and after cycling were used to calculate the mass of trapped species. d) QCM and CV of detrapping processes.

to confirm the hypothesis (Figure 4-3). Indeed, at a scan rate of 1 mV/s, complete charge trapping was observed in the first cycle; no reduction waves were observed for either E_1 or E_2 in the first reverse scan. At a scan rate of 500 mV/s, while charge trapping eventually set in after four cycles, the magnitude of the reduction wave of *E1* appeared much larger than that observed at 20 mV/s. This result clearly indicates PPy-5C-TMPD is thermodynamically stable at both of its charged states, but it is kinetically limited to access both process under fast scan conditions.

4-3. Electrochemical Quartz Crystal Microbalance Studies of PPy-5C-TMPD

As charge trapping has a time-dependent component, it is critical to investigate the ion movement associated with the relevant redox processes. One possible hypothesis of the kinetic limitation for charge trapping is that it might have cation involvement, as in the case of polythiophene. While anion expulsion is expected, cation insertion is observed for charge compensation due to the insulating nature of the polymer, and charge trapping could be a result of free-volume limitations of the polymer. To assess the validity of this hypothesis, two methods were employed: 1) electrochemical quartz microbalance (*EQCM*) can be used to monitor ion movement during redox processes, and 2) cation size variations should affect the charge trapping if cation involvement is indeed present.

In fact, *EQCM* measurements in this case would provide ample information, not only as an *in-situ* ion incorporation monitoring method, but it will also provide information regarding doping levels and solvation changes. There are various aspects about which we can gain insightful information about PPy-5C-TMPD using the *EQCM*. First, we can quantify the amount of anions incorporated from CV and *EQCM*, and discrepancies between the two methods would indicate significant changes in solvation. Secondly, we can probe the type of anion trapped based on

EQCM data. Thirdly, these experiments would also allow us to quantify the doping level of the PPy-5C-TMPD backbone. From the literature, conducting polymers generally exhibit doping levels between 0.3 – 0.5, and we can confirm that assumption by *EQCM*. Finally, by coupling mass-transport data to electrochemical processes, a comprehensive picture of charge trapping dynamics can be obtained.

Py-5C-TMPD was electropolymerized onto an AT-cut Au QCM substrate in the QCM chamber. The thickness of a film after three cycles of electropolymerization was measured by profilometry to be between 50 – 60 nm with a smooth surface morphology as determined from scanning electron microscopy (SEM).

Upon cycling in blank electrolyte solution, amount of redox-active moiety on PPy-5C-TMPD was quantified both by charge (Q) from CV and mass from *QCM* (Figure 4-4a,b). Calculation indicates about 1.58×10^{-8} mole of ClO_4^- per oxidation process by mass, and 1.38 and 1.80×10^{-8} mole of Q for the first and second oxidation, respectively, by CV. Polymer film solvation can be probed from this set of data. For example, for the first Faradaic process, if the amount of perchlorate ions entered for charge compensation was determined by charge, excess mass detected from QCM measurement accounts for solvation. Based on this assumption in the first Faradaic process, every 2.8 ClO_4^- are accompanied with one MeCN solvent molecule. The confirmation of anion influx by mass and charge validated the lack of significant solvent involvement, which could indicate an insulating nature inside the polymer film.

After oxidation and on the return scan, the reduction associated with the first oxidation was expected to be absent in the CV, and we sought out evidence from *EQCM*. When comparing the film's mass before and after one cycle in electrolyte solution, its mass increased by 1.61 μg, which corresponds to one equivalent of ClO_4^-, based on the number of redox-active units. This confirmation is again validated by

charge and mass comparisons, confirming the previous electrochemical observations of charge trapping.

By following the full cycling of the polymer from untrapped to trapped to being detrapped, we can better understand the incorporation and expulsion processes of ClO_4^- (Figure 4-4d). As we mentioned, after one cycle, one equivalent of ClO_4^- was shown to be trapped inside of the polymer matrix. Previously, very large overpotentials (- 2.5 V) were required to detrap the polymer and expel anions. When the polymer was cycled to – 2.25 V, a drastic drop in mass was observed starting at – 1.6 V toward more negative potentials. The current also indicated a negative value, suggesting that the polymer was being reduced. The mass loading of the polymer reached 0.0 μg at ~ - 1.7 V by EQCM and remained constant until oxidation of the polymer was accessed at – 0.3 V, and a similar pattern of ion movement was observed. It is worth noting that during redox cycling of the polymer film, only ClO_4^- insertion and expulsion were observed during oxidation and reduction, respectively, and no other species were observed to be participating in the redox processes studied.

Additional information on doping levels could be obtained from the mass change profile of PPy-5C-TMPD during redox cycling (Figure 4-4c). As shown in Eq. 1 below, the total mass of ClO_4^- incorporated into the polymer film should be the sum of anions from the two Faradaic processes and anions from PPy doping.

$$\Delta m_t = \Delta m_{f1} + \Delta m_{f2} + \Delta m_p \qquad (1)$$

Based on this simple tabulation, we determined that the doping level of PPy in this redox-active polymer was 0.7. This doping level is much higher than that in most of the conjugated polymers studied, which usually have doping levels ranging from 0.3 – 0.5, with a low value of 0.1 being able to elicit dramatic changes in the electronic conductivity of these polymers. This extraordinarily high doping level is beneficial for two reasons. First of all, heavily doped PPy-5C-TMPD should have a high electronic

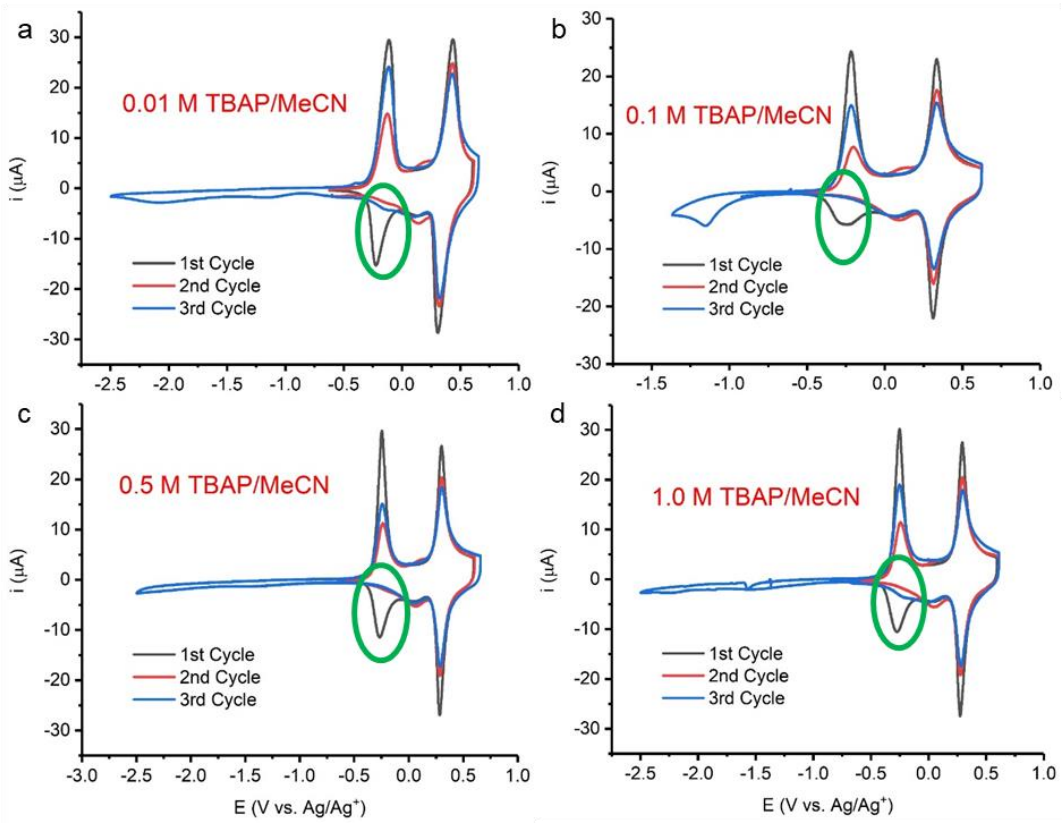

Figure 4-5. a, b, c, d) show the voltammetric responses of PPy-5C-TMPD at various concentration of TBAP/MeCN electrolyte solution, ranging by two orders of magnitutde. All at 20 mV/s.

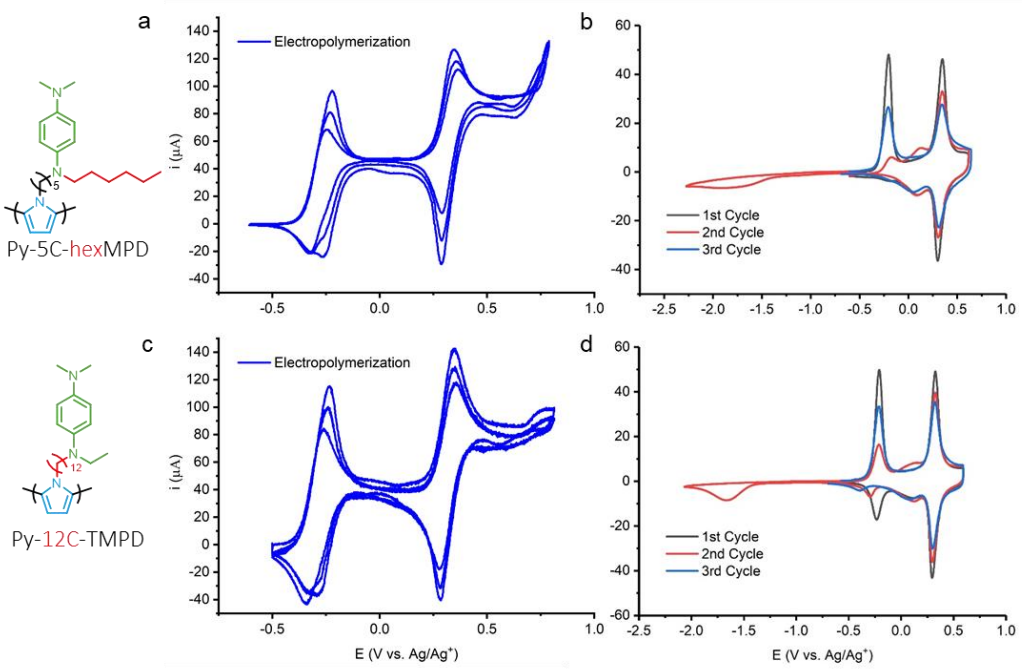

Figure 4-6. a, b) The electropolymerization and film cycling of Py-5C-hexMPD. c, d) The electropolymerization and film cycling of Py-12C-TMPD. All in 0.1 M TBAP/MeCN at 20 mV/s for both electropolymerization and film cycling**.**

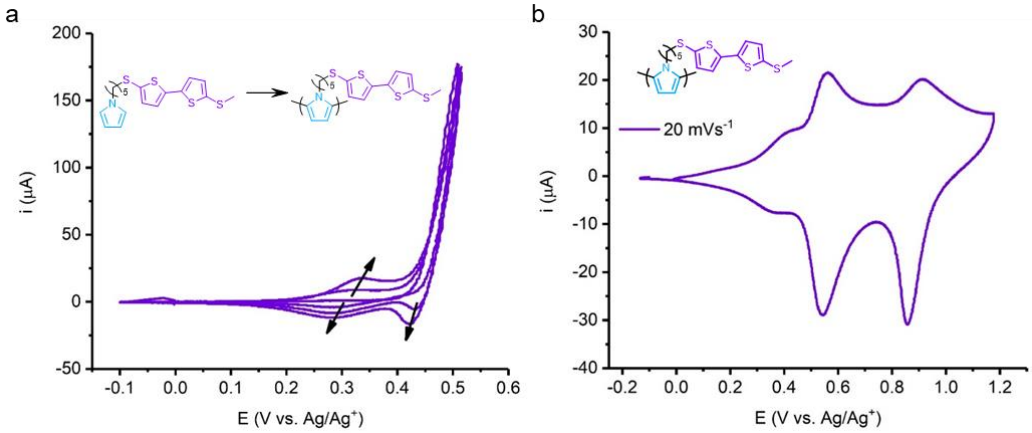

Figure 4-7. a) The electropolymerization of Py-5C-BMTbT and b) film cycling of PPy-5C-BMTbT. All in 0.1 M TBAP/MeCN at 20 mV/s for both electropolymerization and film cycling; 10 mM monomer was used in electropolymerization.

conductivity, validating our design criteria. Secondly, a high doping level also increases the theoretical capacity of PPy-5C-TMPD, which were previously assumed to by 0.3 from anion doping.

EQCM studies of PPy-5C-TMPD have thus provided ample information regarding ion dynamics of PPy-5C-TMPD during redox cycling. We were able to quantify the amount of redox sites and hence ClO_4^-, and determine that there were no other charged species involved in the process. While this information has been helpful in understanding the redox dynamics of PPy-5C-TMPD, *EQCM* has yet to point to a clear direction as to the origin and potential solutions to charge trapping.

4-4. Avoiding Charge Trapping

Finally, with the ample information gathered regarding charge trapping in PPy-5C-TMPD, exhaustive plans were executed to attempt to prevent charge trapping. First, we investigated potential environmental conditions. As briefly mentioned, the insulating nature of the polymer film could induce charge trapping behavior in conducting polymers and a mismatch between polymer and electrolyte could exacerbate that effect. First of all, we varied the ionic strength by two orders of magnitude in an attempt to alleviate charge trapping, but without success (Figure 4-5). Subsequently, a variety of solvents with a wide range of dielectric constants (7 – 64) were also tested to the same end, but again without success. These results indicate that it is unlikely that environmental conditions are causing charge trapping. Subsequently, a number of structural modifications were attempted to alleviate charge trapping, including the installation of hexyl side-chains to the TMPD unit to prevent π-π stacking as well as elongation of the alkyl linker (from 5C to 12C) to lessen the local charge density. Both measures were proven unsuccessful (Figure 4-6).

After our exhaustive search for measures to prevent charge trapping, results

have shown that both the polymer structure and the environmental conditions are sound, as they did not induce nor prevent charge trapping. If charge trapping is a chemically specific phenomenon to TMPD in this context, a pendant substitution would be a promising solution. TMPD was then substituted with BMTbT as a redox-active pendant, and indeed the resulting polymer showed good electrochemical and chemical reversibility with two well-defined redox couples. It can be concluded from this substitution that in the PPy-5C-TMPD polymer, TMPD is the cause of charge trapping and great caution should be taken when selecting redox-active pendants to use (Figure 4-7).

4-5. Conclusions

Charge trapping in PPy-5C-TMPD was studied in detail using a variety of characterization methods. The kinetic nature of charge trapping was identified by CV, and indicated that both redox couples are susceptible to charge trap. *EQCM* confirmed that anion incorporation and expulsion were coupled to the Faradaic processes. Upon exhaustive environmental and structural controls, it was concluded that charge trapping is due to the intrinsic reactivity of TMPD, as shown by the absence of charge trapping when TMPD was substituted with BMTbT in PPy-5C-BMTbT. In general, this study instructs us to choose redox-active pendants with care to avoid undesirable reactivity.

REFERENCES

1. Linsebigler, A. L.; Lu, G.; Yates, J. T. *Chemical Reviews* **1995,** *95* (3), 735-758.

2. Huang, Y. L.; Chen, Y.; Zhang, W.; Quek, S. Y.; Chen, C.-H.; Li, L.-J.; Hsu, W.-T.; Chang, W.-H.; Zheng, Y. J.; Chen, W.; Wee, A. T. S. *Nature Communications* **2015,** *6*, 6298.

3. Zotti, G.; Schiavon, G.; Zecchin, S. *Synthetic Metals* **1995,** *72* (3), 275-281.

4. Semenikhin, O. A.; Ovsyannikova, E. V.; Ehrenburg, M. R.; Alpatova, N. M.; Kazarinov, V. E. *Journal of Electroanalytical Chemistry* **2000,** *494* (1), 1-11.

5. Borjas, R.; Buttry, D. A., *Chemistry of Materials* **1991,** *3* (5), 872-878.

6. Abruña, H. D.; Denisevich, P.; Umana, M.; Meyer, T. J.; Murray, R. W., *Journal of the American Chemical Society* **1981,** *103* (1), 1-5.

7. Conte, S.; Rodriguez-Calero, G. G.; Burkhardt, S. E.; Lowe, M. A.; Abruna, H. D. *RSC Advances* **2013,** *3* (6), 1957-1964.

8. Shen, L.; Mizutani, M.; Rodríguez-Calero, G. G.; Hernández-Burgos, K.; Truong, T.-T.; Coates, G. W.; Abruña, H. D., *J. Electrochem. Soc.*, **2017**, 164, A1946-1951.

SUPPORTING INFORMATION

Electrochemical Measurements

General Materials and Methods. Pyrrole (>99%) were purchased from TCI without further purification. 18-crown-6 (>99%), 1,5-dibromopropane (99%), 1,12-dibromododecane (99%), 1-bromohexane (98%), 2,2'-bithiophene (99%), n-Butyllithium (2.5 M in hexane), sulfur (99.998%), *N*,*N*-dimethylephenyldiamine (97%), 1-bromoethane (98%) were purchased from Sigma-Aldrich. *N*-ethyl-*N'*,*N'*-dimethyle-*p*-phenylenediamine was prepared according to a literature procedure[7]. All reactions were run in a drybox or using standard Schlenk techniques. All other reagents were purchased from commercial sources and used as received. A Varian Mercury (300 MHz) spectrometer was used to record ^{1}H NMR spectra.

General Procedures for Electrochemical Measurements. All electrochemical measurements, unless otherwise noted, were performed in a three-compartment fritted glass cell using a three-electrode configuration. A Pt wire was used as the counter electrode, the reference electrode was a homemade Ag/Ag^+ (with 0.05 M $AgClO_4$ in 0.1 M TBAP in MeCN solution inside the electrode and immersed in 0.1 M TBAP in acetonitrile (MeCN) solution) and a homemade glassy carbon electrode (3 mm diameter) was used as the working electrode. The working electrodes were electrochemically cleaned by cycling between – 2.0 V – 1.0 V (vs. Ag/AgCl) for 10 cycles in 0.5 M KOH solution, and subsequently mechanically cleaned with alumina/water slurry, 1.0 μm, 0.3 μm and 0.05, in this order, and then rinsed clean with DI water.

The following procedure was taken to clean Au QCM electrode before use.

Any residual organic material was removed using a fine swab that does not scratch surfaces with acetone. The Au electrode was then cycled in 0.1 M $HClO_4$ between – 0.2 – 1.4 V vs. Ag/AgCl at 200 mVs^{-1} until a clean and stable Au profile is obtained.

Monomer Synthesis

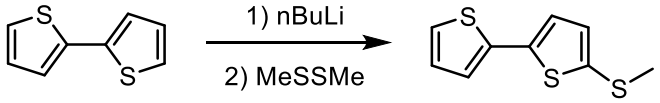

5-(methylthio)-2,2'-bithiophene

2,2'-Bithiophene (1.0 g, 6.01 mmol) was dissolved in 20 mL of ether and was slowly added with 3.95 mL of nBuLi (6.32 mmol) at -78 °C. After 1 hour, the resulting solution was warmed to 25 °C, and 0.63 g of MeSSMe (0.664 mmol)) was added at -78 °C. After the solution was let reacting overnight at 25 °C, it was washed with diethyl ether twice and then water. After purification with hexane by silica gel column chromatography, cololess oil was separated. Yield: 0.70 g (55 %). **^{1}H NMR** (300 MHz, DMSO-D_6): δ 7.26 (1H), 7.20 (1H), 7.13 (1H), 7.01 (2H), 2.51 (3H).

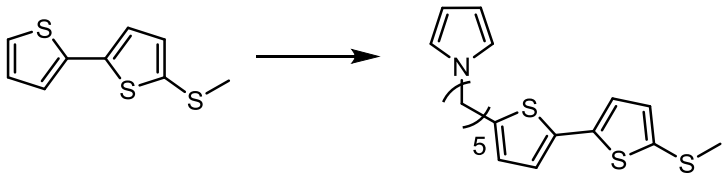

Py-5C-BMTBT

5-(methylthio)-2,2'-bithiophene from last step (0.5 g, 2.35 mmol) was slowly added with nBuLi (1.54 mL, 2.47 mmol) at -78 °C. After 1 hour, the resulting solution was warmed to 25 °C, and was added slowly with S (0.073 g, 2.35 mmol) and Py-5C-Br (0.64 g, 2.94 mmol) in this order. The reaction mixture reacted overnight at 25 °C, and was then washed twice with ether and then water. The green oil was separated by silica gel column chromatograph (dichloromethane:hexane = 25:75). Yield: 0.21 g (30 %). **^{1}H NMR** (300 MHz, $CDCl_3$): δ 6.97 (4H), 6.63 (1H), 6.13 (1H), 5.30 (1H), 3.87 (2H), 2.78 (2H), 1.79 (2H), 1.65 (2H), 1.40 (2H).

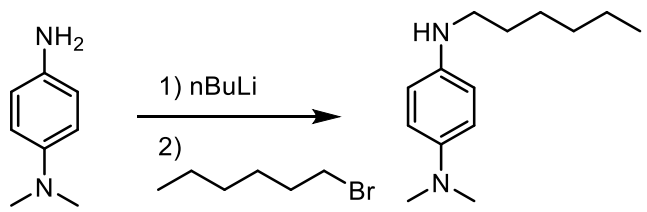

N^1-hexyl-N^4,N^4-dimethylbenzene-1,4-diamine

HexylMPD was synthesized based on procedure previously reported in publication in chapter 3. *N*,*N*-dimethylphenylenediamine (2.0 g, 14.68 mmol) was dissolved in THF, and 6.30 mL of nBuLi (10.10 mmol) was slowly added at -78 °C. after reacting for 1 hour at 25 °C, 2.1 mL of hexylbromide was slowly added to the mixture at -78 °C. After reacting overnight at 25 °C, the crude material was separated by washing the reaction mixture with ether twice and then water. The product was separate by silica gel column chromatography (ethyl acetate:dichloromethane = 1:2). Yield: 1.85 g (57 %). **^{1}H NMR** (300 MHz, DMSO-D_6): δ 6.60 (2H), 6.47 (2H), 4.82 (1H), 2.86 (2H), 2.68 (6H), 1.49 (2H), 1.28 (6H), 0.85, 3H).

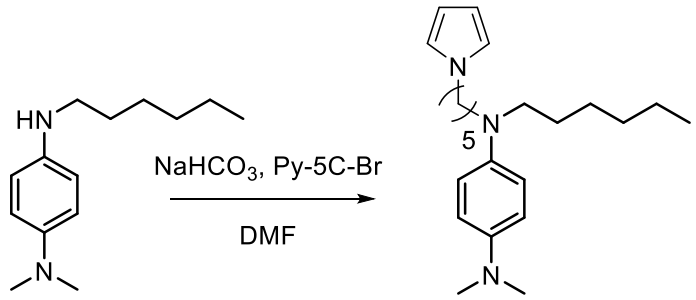

Py-5C-hexylMPD

Py-5C-hexylMPD was synthesized based on the procedure previously reported in publication in chapter 3 using hexylMPD as the reactant. 0.5 g (2.31 mmol) of Py-5C-Br was mixed with hexylMPD (0.67 g, 3.04 mmol) in DMF with $NaHCO_3$ (1.05 g, 12.50 mmol) in 5 mL of DMF. The reaction was run overnight at 90 °C, and the resulting mixture was washed with KOH solution, diethyl ether twice and water in that order. The product was separate by silica gel column chromatography (hexane:diethyl ether = 50:50). Yield: 1.02 g (94 %).**^{1}H NMR** (300 MHz, DMSO-D_6): δ 6.68 (2H), 6.62 (4H), 5.93 (2H), 3.81 (2H), 3.05 (4H), 2.71 (6H), 1.66 (2H), 1.39 (4H), 1.23 (8H), 0.84 3H).

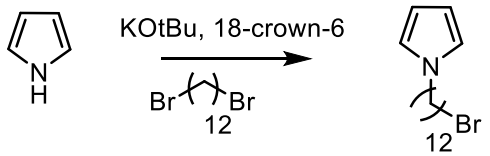

Py-12C-Br

Py-12C-Br was synthesized based on previously reported procedures in publication in chapter 3. 2.00 g of pyrrole (30.0 mmol) was dissolved in diethyl ether, and it was slowly added to 4.40 g (39.3 mmol) of KO^{t}Bu. After let reacting for 1 hour, 7.1 g (21.6 mmol) of dibromododecane was added to the mixture dropwise. After let reacting overnight at 25 °C, the mixture was washed with diethyl ether twice then with water. The product was separate by silica gel column chromatography (hexane:dichloromethane = 50:50). Yield: 1.54 g (16 %). **^{1}H NMR** (300 MHz, $CDCl_3$): δ 6.67 (2H), 6.15 (2H), 3.88 (2H), 3.51 (2H), 2.07 (2H), 1.89 (2H), 1.41 (16H).

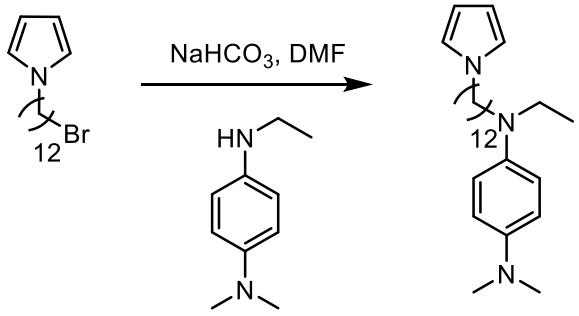

Py-12C-TMPD

Py-12C-TMPD was synthesized based on previously reported procedures in publication in Chapter 3. 0.2 g (0.64 mmol) of Py-12C-Br was added with 0.1 g (0.64 mmol) of N-ethyl,N',N'-dimethylphenylenediamine and 0.107 g (1.20 mmol) of $NaHO_3$ in 5 mL of DMF. The reaction was run overnight at 90 °C, and it was then washed twice with ether and water. The product was separated by silica gel column chromatography with either. Yield: 0.21 g (82 %). **^{1}H NMR** (300 MHz, $CDCl_3$): δ 6.76 (2H), 6.72 (2H), 6.64 (2H), 6.13 (2H), 3.86 (2H), 3.49 (2H), 3.23 (2H), 2.83 (6H), 1.75 (2H), 1.43 (2H), 1.25 (16H), 1.08 (3H).

NMR Spectra

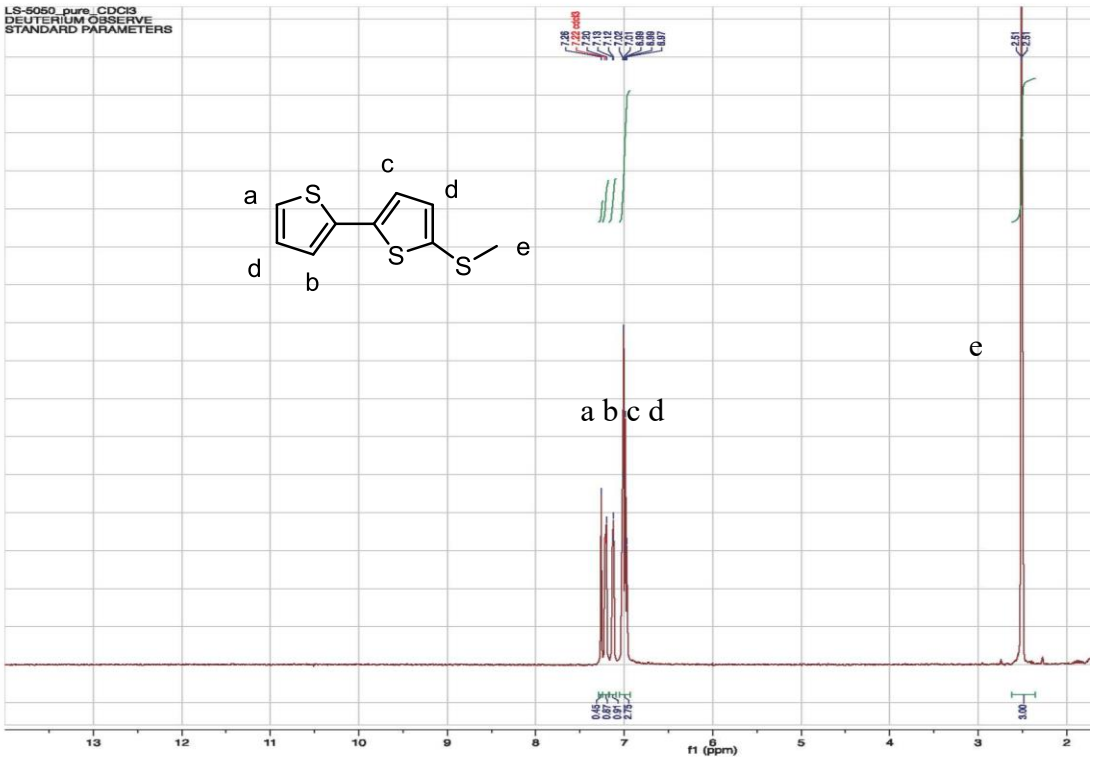
LS-5050_pure_CDCl3
DEUTERIUM OBSERVE
STANDARD PARAMETERS
a
b
c
d
e
S
S
a b c d
e
f1 (ppm)

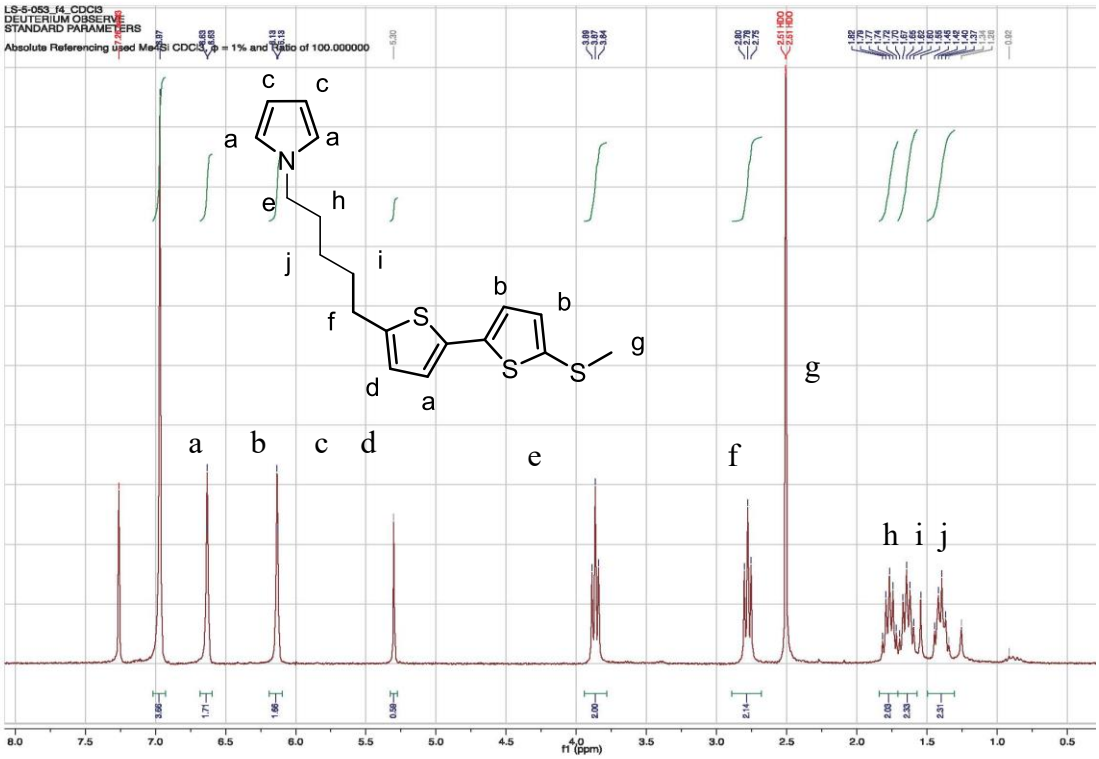
LS-5-053_f4_CDCl3
DEUTERIUM OBSERVE
STANDARD PARAMETERS
N
a
b
c
d
e
f
g
h
i
j
S
S
a b c d
e
f
g
h i j
f1 (ppm)

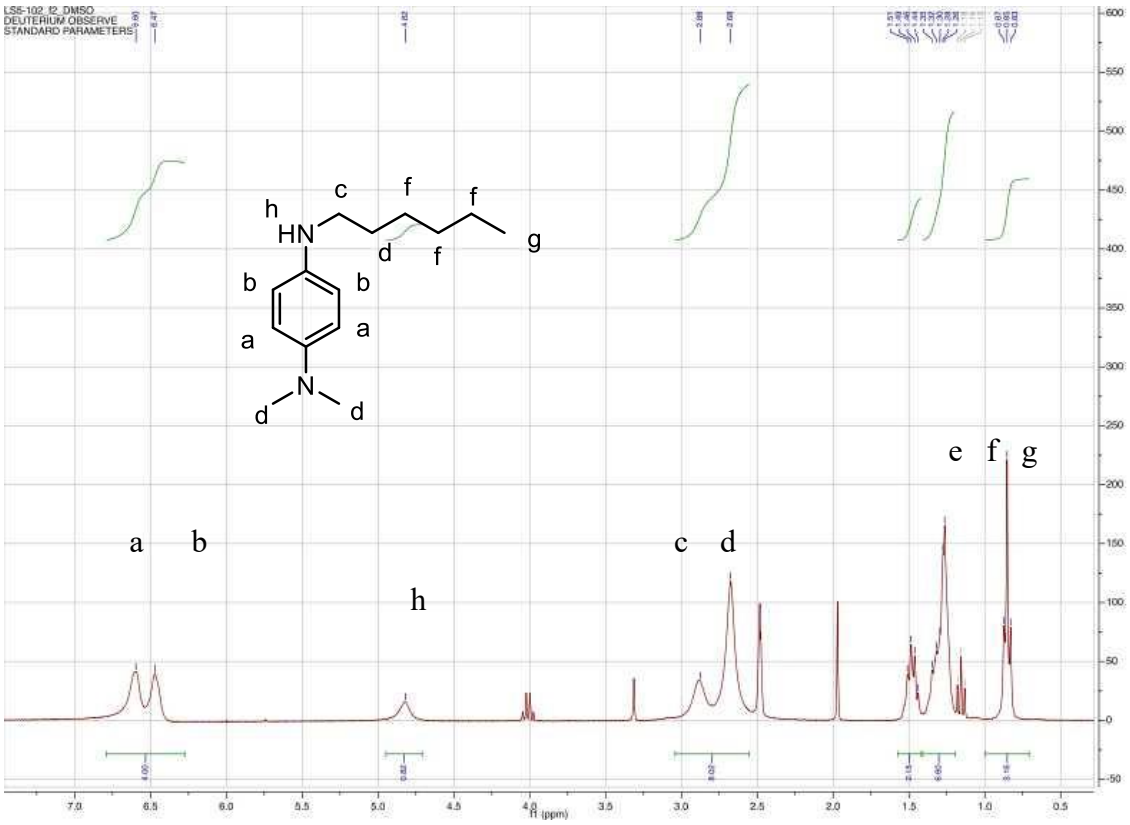
LS6-102_f2_DMSO
DEUTERIUM OBSERVE
STANDARD PARAMETERS
h
HN
c
f
f
g
d
f
b
b
a
a
N
d
d
a
b
h
c
d
e
f
g

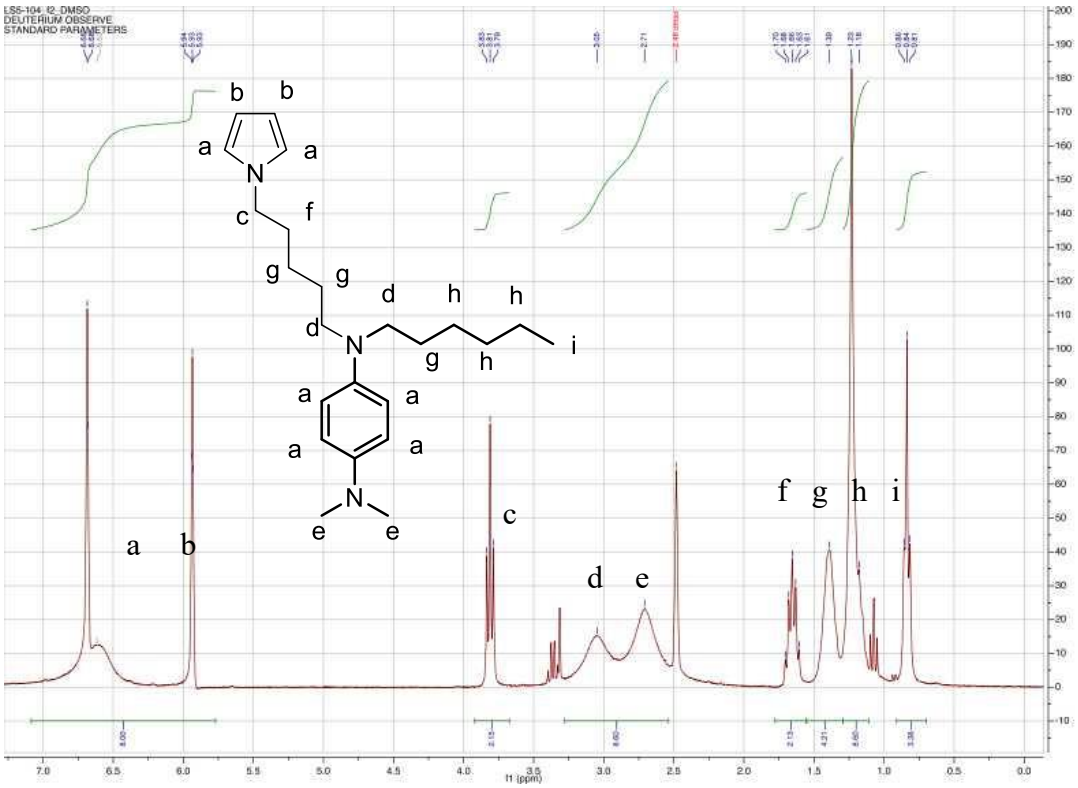
LS6-104_f2_DMSO
DEUTERIUM OBSERVE
STANDARD PARAMETERS
b
b
a
a
N
c
f
g
g
d
h
h
d
N
g
h
i
a
a
a
a
N
e
e
a
b
c
d
e
f
g
h
i

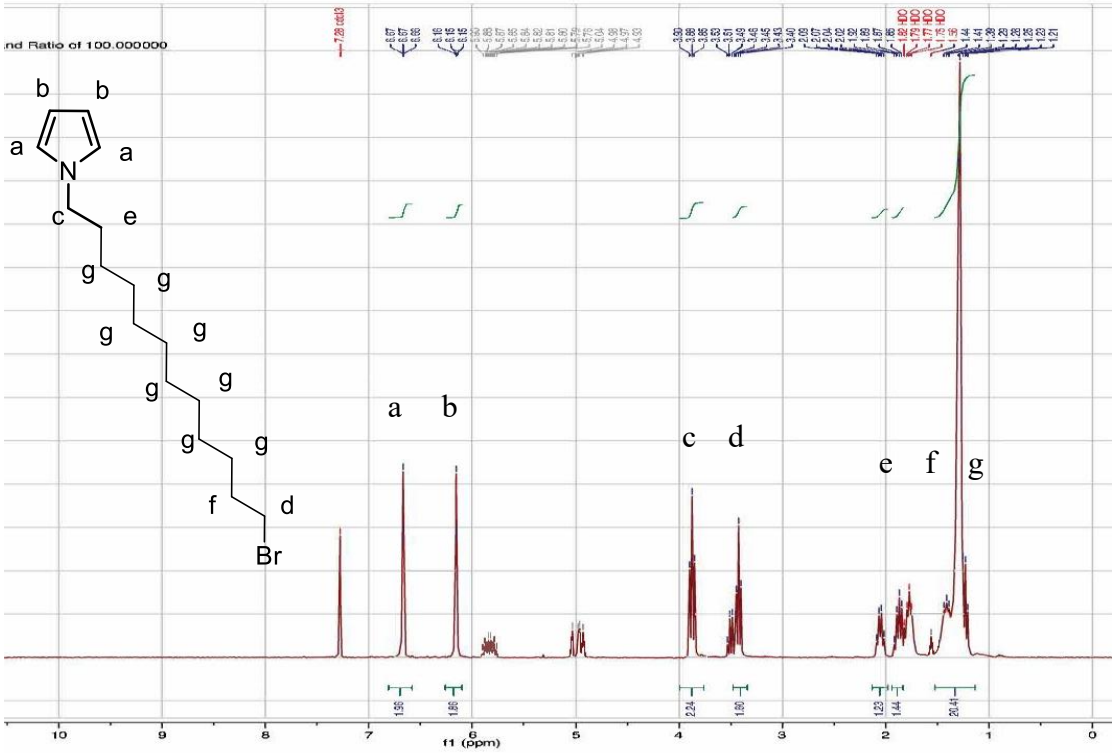
nd Ratio of 100.000000
b b
a a
N
c e
g g
g g
g g
g g
g g
f d
Br
a b
c d
e f g
f1 (ppm)

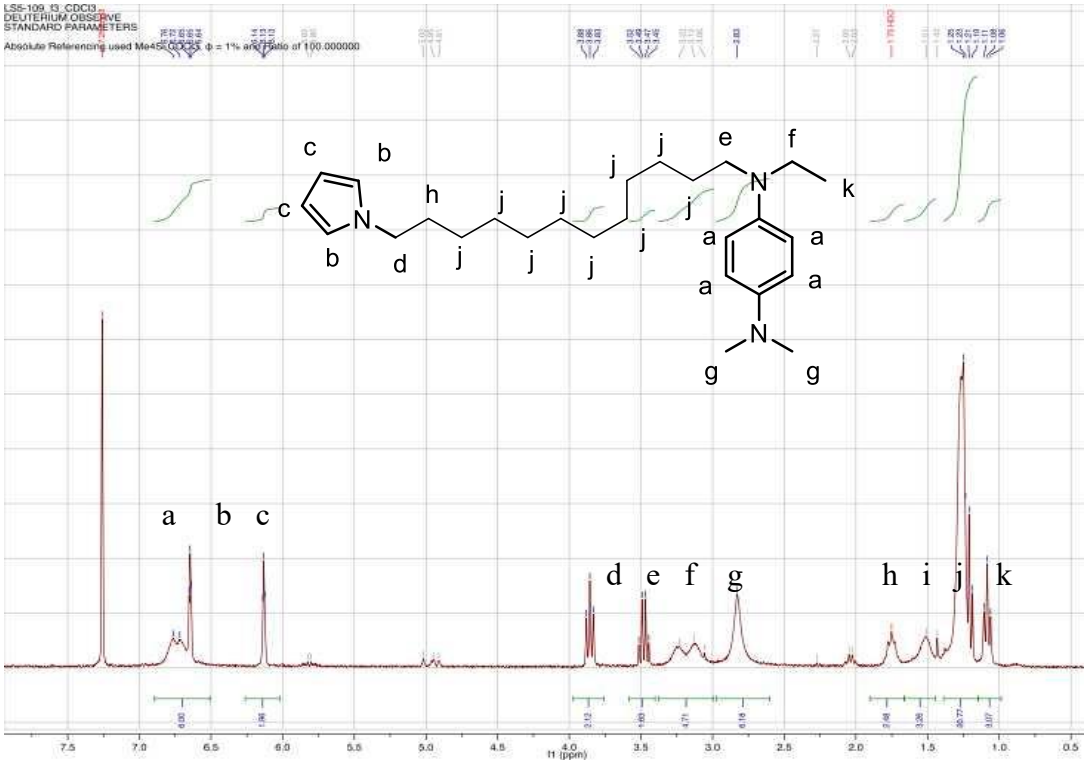
LS5-109_f3_CDCl3
DEUTERIUM OBSERVE
STANDARD PARAMETERS
c b
c N
b
h
d
j
e f
k
N
a a
a a
N
g g
a b c
d e f g
h i j k
f1 (ppm)

CHAPTER 5
PHENOTHIAZINE-BASED POLYMER CATHODE MATERIALS WITH ULTRA-HIGH POWER DENSITITIES FOR LITHIUM ION BATTERIES[vii]

5-1. Introduction

LIBs currently deliver the highest energy density of any known secondary electrochemical energy storage system. However, new cathode materials are needed to improve the power densities of LIBs.[1-3] Organic and polymeric materials are excellent candidates for next-generation electrode materials in high-power and high-energy density electrochemical energy storage applications. In contrast to traditional LIB cathodes such as metal oxides, organic materials possess a few advantages over them. Being environmentally friendly by using non-precious and earth-abundant elements, organic and polymeric materials align perfectly with the green and sustainable approach that global communities are striving. Most importantly, structural tunability of organic and polymeric materials continues to provide wide possibilities for high-energy and high-power materials. To maximize energy density, the maximum number of electrons transferred can be achieved by molecular design such as incorporating heteroatoms within aromatic systems. Power density can be enhanced by the incorporation of π-extended systems in the anchoring structures. Over the past decades, the field of organic and polymeric cathodes for LIBs has blossomed from electrochemical ideals to highly promising practicals.

5-2. Design Criteria

[vii] This chapter was reproduced in part with permission from Peterson, B.[*]; Shen, L.[*]; Ren, D.[*]; Ulgut, B.; Abruña, H. D.; Fors, B. P. Ultrahigh Rate Electrochemical Performance of a Class of High-Energy Phenothiazine-Derivatized Main-Chain Polymers for Lithium-Ion

While in the previous chapter, conducting polymers were explored and studied as promising candidates as battery electrodes, the majority of organic electrode work has been focused on redox polymers. These polymers, while anchored either onto a substrate or to a neighboring redox unit by the polymer backbone, improve upon the redox-active small molecule electrodes in terms of solubility. The anchoring and/or presence of a polymer backbone can largely mitigate the solubility of electrode materials into the battery electrolyte solution, improving long-term cycling stability. However, the problem of diminishing electronic conductivity surfaces when an insulating backbone is used as the anchoring functionality.

On the other hand, a rich reservoir of redox-active small molecules provides ample candidates to be attached to the polymer backbone for maximum energy density.[4-6] In addition to the redox-active centers discussed in the previous chapters, we utilized another molecule that has recently gained attention. Phenothiazine is an aromatic heterocyclic small molecule with N and S as heteroatoms. It was popularized in the form of methylene blue, a diaminated cationic version of phenothiazine. Phenothiazine exhibits two chemically and electrochemically reversible redox couples at 0.5 and 1.3 V vs. *Ag/Ag+*. Recently, several groups have employed phenothiazine as the redox-active unit in a polymer architecture to be used in batteries, expanding the library of *p-type* electrodes. [7-9] However, detrimental aspects still exist in these polymer architectures, including the use of an insulating polymer backbone that limits the active material loading in the device. In response to these limitations, we incorporated phenothiazine into a novel architecture (Figure 5-1).

Battery. *Manuscript in preparation.*

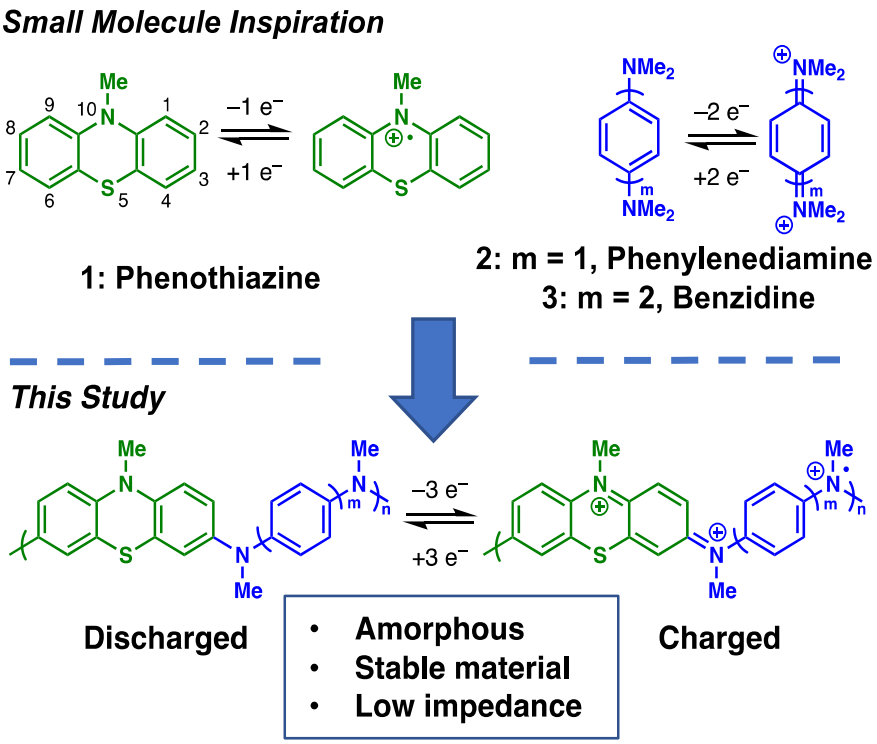

Figure 5-1. Small molecule inspiration and molecular design.

In the design, we sought to synthesize phenothiazine based polymer cathodes capable of delivering high energy densities at fast charging and discharging rates. We hypothesized that stabilization of N-methylphenothiazine **(1)** through copolymerization with electron rich and redox active aryl amines would mimick the stabilized oxidized state of methylene blue, and afford polymers with high theoretical capacities and stable charged states. Two aryl amines, *N, N, N', N'*-tetramethyl-*p*-phenylenediamine **(2)** and *N, N, N', N'*-tetramethylbenzidine **(3)**, were natural candidates, considering their multiple oxidation events to a stabilized quinoidal dication at potentials greater than 3.3 V vs Li/Li^+.[10] We further hypothesized that copolymerization through the 3 and 7 positions of phenothiazine would facilitate fast charging and discharging rates, since partial conjugation throughout the entire backbone would allow for facile electron transfer.

5-3. Electrochemical Characterization

Poly(*N*-methylphenothiazine dimethylphenylenediamine) (PT-DMPD) and poly(*N*-methylphenothiazine benzidine) (PT-BZ) were synthesized from inexpensive starting materials using Buchwald-Hartwig cross-coupling of 3,7-dibromo-*N*-methylphenothiazine **(1a)** and dimethylphenylenediamine **(2a)** or dimethylbenzidine **(3a)** (Figure 5-2a).[11, 12] The resulting linear polymers were insoluble in their neutral state, and their electrochemical properties were probed using cyclic voltammetry (CV), measured as slurries, in a solution of $LiPF_6$ (1 M) in ethylene carbonate/diethyl carbonate (EC/DEC). The neutral and oxidized redox states of PT-DMPD are displayed in Figure 5-1. The three discrete redox couples of each polymer were observed

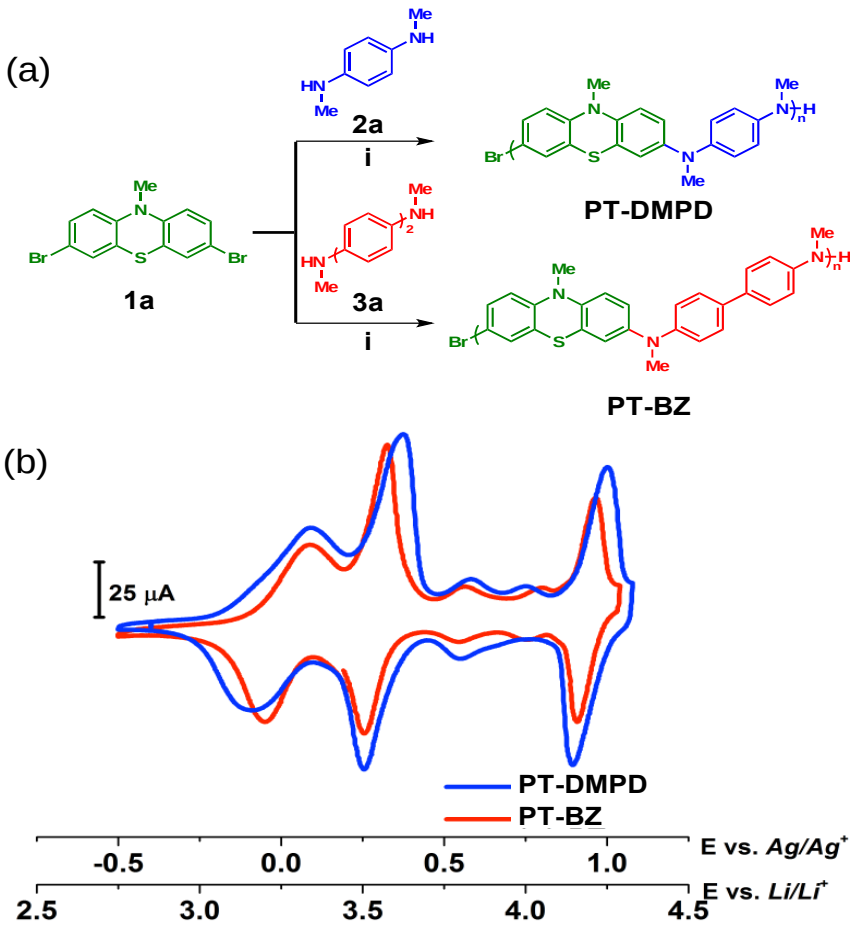

Figure 5-2. (a) General synthetic strategy for PT-DMPD and PT-BZ polymers using Buchwald-Hartwig coupling. i: NaO*t*Bu, RuPhos (3 mol%), RuPhos Pd G2 (3 mol%), Toluene, 80 °C. (b) Neutral and oxidized states of PT-DMPD (c) Slurry CV of PT-DMPD and PT-BZ in $LiPF_6$ (1 M) in EC/DEC at 20 mVs^{-1}.

by CV (Figure 5-2b), taking place at 3.3, 3.6, and 4.3 V vs Li/Li^+ [viii], respectively. These redox potentials are among the highest in organic battery electrodes reported for electrical energy storage applications.

5-4. Device Performance and the Effect of Polymer Cross-linking

Coin cells employing PT-DMPD or PT-BZ as the cathode and Li metal as the anode were assembled to explore the performance of the polymers in devices. Due to the limited stability window of the electrolyte medium (EC/DEC), only the first two redox couples were accessed in coin cell cycling (See supporting information, Figure 5-S1). Figure 5-3a presents the first charge-discharge curves of PT-DMPD and PT-BZ at 1 C over the voltage range from 2.8 to 4.3 V. Both exhibit reversible two-stage charge-discharge behavior, which is consistent with the two major redox couples observed in the CV. The discharge capacities of PT-DMPD and PT-BZ were 128 mAh/g and 97 mAh/g, representing 82 and 76% of their theoretical capacities, respectively. However, both materials exhibited a relatively low coulombic efficiency (35% for PT-DMPD and 44% for PT-BZ). The cycling performances of the PT-DMPD and PT-BZ cathode materials are shown in Figure 5-3b. Both cells were cycled at 25 °C over the same voltage range at 1 C. The discharge capacity of PT-DMPD was 82 mAh/g after 50 cycles (64% retention), while that of PT-BZ was 64 mAh/g after 50 cycles (66% retention). Since the PT-DMPD polymer exhibited higher capacity than PT-BZ polymer, further work focused on the former.

We hypothesized that the low coulombic efficiency and capacity fade upon

[viii] We hypothesize the two small redox couples at 3.6 and 4.0 V vs. Li/Li^+ correspond to redox active end groups of the polymers.

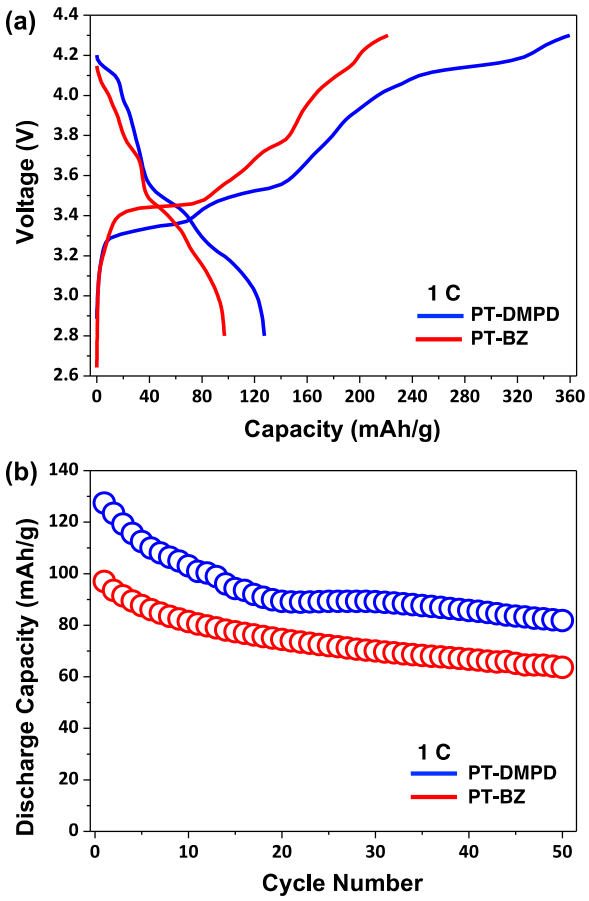

Figure 5-3. (a) Initial charge–discharge curves of PT-DMPD and PT-BZ coin cells at 1 C in 1M $LiPF_6$ in EC/DEC. (b) Cycling performance of the PT-DMPD and PT-BZ cells at 1 C.

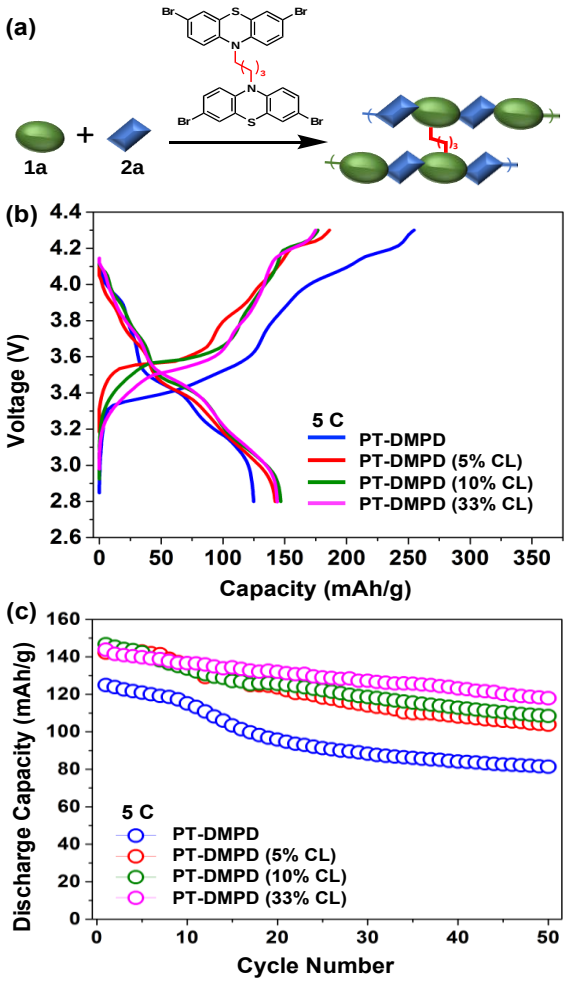

Figure 5-4. (a) Cross-linker (CL) structure and material design. (b) Initial charge-discharge of PT-DMPD, PT-DMPD (5% CL), PT-DMPD (10% CL), and PT-DMPD (33% CL) at 5 C. (c) Cycling performance of PT-DMPD, PT-DMPD (5% CL), PT-DMPD (10% CL), and PT-DMPD (33% CL) at 5 C.

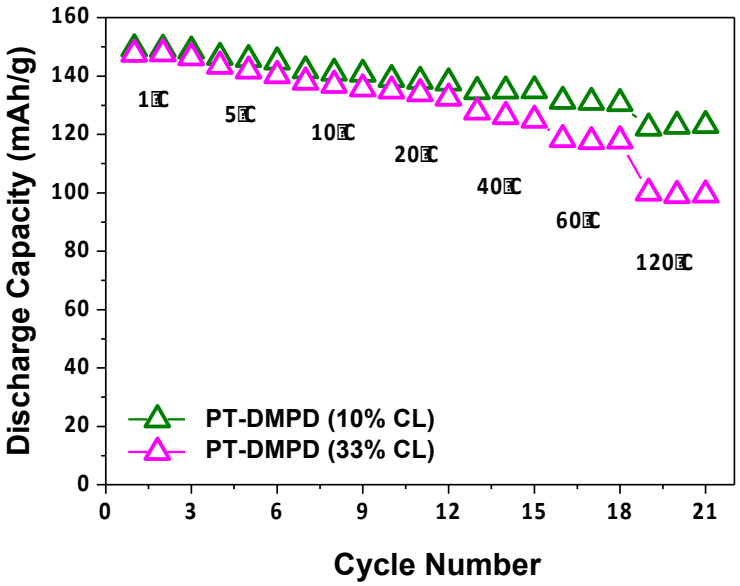

Figure 5-5. Discharge capacities of PT-DMPD (10% CL) and PT-DMPD (33% CL) at C-rates from 1 C to 120 C.

cycling were caused by dissolution of the polymer upon oxidation. This dissolution could be observed visually as green dissolved polymer diffused away from the electrode during CV cycling. To address these limitations, a second class of cross-linked materials was synthesized to generate polymers with decreased solubility in the electrolyte medium (Figure 5-4a). The first charge-discharge cycles of PT-DMPD, PT-DMPD (5% cross-linked, 5% CL), PT-DMPD (10% CL), and PT-DMPD (33% CL) at 5 C are shown in Figure 5-4b. Increased discharge capacities were obtained as the mol percentage of cross-linker was increased, with PT-DMPD (10% CL) exhibiting the highest discharge capacity of 150 mAh/g (97% of the theoretical value of PT-DMPD). In addition, the decrease in charging capacity loss led to a significant improvement in the coulombic efficiency with increasing cross-linker content. It is likely that this decrease in charging capacity loss results from either a suppression of polymer degradation or a decrease in small, soluble oligomers, which can act as electron shuttles between electrodes during charging.[13-15] The coulombic efficiency at 5 C increased from 49% to 82% between linear (no cross-linker) and 33% cross-linked polymer. By eliminating dissolution through cross-linking, both the capacity and coulombic efficiency were greatly improved.

The cycling performance of PT-DMPD, PT-DMPD (5% CL), PT-DMPD (10% CL) and PT-DMPD (33% CL) materials was investigated between 2.8 and 4.3 V at 5 C, as shown in Figure 5-4c. Increasing the mol percentage of cross-linker resulted in materials exhibiting enhanced cycling performance when compared to linear PT-DMPD. As the mol percentage of cross-linker increased from 0% to 5% to 10% to 33%, the capacity retention after 50 cycles increased from 65% to 73% to 74% to

82%, respectively. These results demonstrate that dissolution of the polymer from the cathode was mitigated in the cross-linked materials.

For use in high power applications, the proposed materials must be able to deliver high discharge capacities at fast discharge rates. To better understand the relationship between mol% cross-linker and the materials capacity retention at increasing discharge rates, the rate capabilities of PT-DMPD (10% CL) and PT-DMPD (33% CL), the two materials displaying the highest discharge capacities, were investigated between 2.8 and 4.3 V. Figure 5-5 compares the discharge capacities of these materials charged at 1 C and discharged at C-rates of 1, 5, 10, 20, 40, 60, and 120 C. Significantly, excellent capacity retention (82%) was observed in PT-DMPD (10% CL) between even the most extreme discharging rates, 1 C to 120 C. While similar capacities are observed at the lower rates for both materials, an apparent decrease in capacity is evident in PT-DMPD (33% CL) at higher discharge rates. We attribute this to a decrease in the rate of counterion transport through the more densely cross-linked material. Notably, the PT-DMPD (10% CL) material retained a very high discharge capacity of 122.3 mAh/g at the ultrahigh C-rate of 120 C.[ix]

Encouraged by the fast discharge rates exhibited by these materials, electrochemical impedance spectroscopy (EIS) was used to measure the charge transfer resistance of PT-DMPD (10% CL) in a coin cell to explore the origin of the ultrahigh-rate behavior.[16-18] In impedance measurements, a high frequency semicircle is attributed to the double layer and the kinetics of the active material (Figure 5-S4). In

[ix] By comparison, the reported materials retain 82 % of initial capacity (150 mAh/g) at 120 C, whereas phenothiazine-based material reported in Ref. 8 retains 52 % of initial capacity (79 mAh/g) at 100 C.

addition, the low frequency behavior is attributed to transport effects. The high frequency semicircle was fit to a simplified Randles model, and the charge transfer resistances obtained are given as an inset to Figure 5-S4.

As expected, the charge transfer resistance was a function of the oxidation state of the polymer. The charge transfer resistances near the redox couple around 3.6 V were found to be much lower than the charge transfer resistances near 4.1 V and 3.1 V. Overall, the charge transfer resistances were between 80 Ω and 230 Ω. When compared to literature reports, these values are similar or lower than comparable systems, reflecting fast charge transfer kinetics.[16, 18-22] This facile kinetic behavior allows the battery to operate at high C-rates without excessive overpotentials. The low overpotentials, in turn, are one of the reasons for the high rate cycling capability without significant loss of capacity. The low charge transfer resistance is shown by retention of capacity and cycling stability in coin-cells with 75% active material loading (Figure 5-S3).

5-5. Conclusions

In conclusion, we have designed, synthesized, and tested a class of high-energy phenothiazine-derived redox-active polymers that deliver high capacities at ultra-fast discharge rates and high operating voltages in lithium ion batteries. The initial capacity fade, due to electrode dissolution, was largely mitigated through the use of cross-linked materials, which led to dramatically improved cycling performance, discharge capacity, and coloumbic efficiency without compromising the material's rate capability. PT-DMPD (10% CL) retained 82% capacity at an unparalleled 120 C rating. These results validate our design principles, and are highly instructive for

future design of high-energy and high-rate organic electrodes for electrical energy storage applications.

REFERENCES

1. P. Novák, K. Müller, K. S. V. Santhanam and O. Haas, *Chemical Reviews*, 1997, **97**, 207-282.
2. Y. Liang, Z. Tao and J. Chen, *Advanced Energy Materials*, 2012, **2**, 742-769.
3. T. B. Schon, B. T. McAllister, P.-F. Li and D. S. Seferos, *Chemical Society Reviews*, 2016, **45**, 6345-6404.
4. B. Häupler, R. Burges, C. Friebe, T. Janoschka, D. Schmidt, A. Wild and S. Schubert Ulrich, *Macromolecular Rapid Communications*, 2014, **35**, 1367-1371.
5. Y. Imada, H. Nakano, K. Furukawa, R. Kishi, M. Nakano, H. Maruyama, M. Nakamoto, A. Sekiguchi, M. Ogawa, T. Ohta and Y. Yamamoto, *Journal of the American Chemical Society*, 2016, **138**, 479-482.
6. M. E. Speer, M. Kolek, J. J. Jassoy, J. Heine, M. Winter, P. M. Bieker and B. Esser, *Chemical Communications*, 2015, **51**, 15261-15264.
7. A. A. Golriz, T. Kaule, M. B. Untch, K. Kolman, R. Berger and J. S. Gutmann, *ACS Applied Materials & Interfaces*, 2013, **5**, 2485-2494.
8. M. Kolek, F. Otteny, P. Schmidt, C. Muck-Lichtenfeld, C. Einholz, J. Becking, E. Schleicher, M. Winter, P. Bieker and B. Esser, *Energy & Environmental Science*, 2017, **10**, 2334-2341.
9. T. Godet-Bar, J. C. Lepretre, O. Le Bacq, J. Y. Sanchez, A. Deronzier and A. Pasturel, *Physical Chemistry Chemical Physics*, 2015, **17**, 25283-25296.
10. T.-T. Truong, G. W. Coates and H. D. Abruna, *Chemical Communications*, 2015, **51**, 14674-14677.
11. B. P. Fors, D. A. Watson, M. R. Biscoe and S. L. Buchwald, *Journal of the American Chemical Society*, 2008, **130**, 13552-13554.
12. B. P. Fors, N. R. Davis and S. L. Buchwald, *Journal of the American Chemical Society*, 2009, **131**, 5766-5768.
13. E. Peled, Y. Sternberg, A. Gorenshtein and Y. Lavi, *Journal of The Electrochemical Society*, 1989, **136**, 1621-1625.

14. Y. V. Mikhaylik and J. R. Akridge, *Journal of The Electrochemical Society*, 2004, **151**, A1969-A1976.
15. Y. Diao, K. Xie, S. Xiong and X. Hong, *Journal of Power Sources*, 2013, **235**, 181-186.
16. M. E. Bhosale and K. Krishnamoorthy, *Chemistry of Materials*, 2015, **27**, 2121-2126.
17. K. Zhang, C. Guo, Q. Zhao, Z. Niu and J. Chen, *Advanced Science*, 2015, **2**, 1500018-n/a.
18. H. Wu, S. A. Shevlin, Q. Meng, W. Guo, Y. Meng, K. Lu, Z. Wei and Z. Guo, *Advanced Materials*, 2014, **26**, 3338-3343.
19. Z. Song, Y. Qian, M. L. Gordin, D. Tang, T. Xu, M. Otani, H. Zhan, H. Zhou and D. Wang, *Angewandte Chemie*, 2015, **127**, 14153-14157.
20. S. Wang, Q. Wang, P. Shao, Y. Han, X. Gao, L. Ma, S. Yuan, X. Ma, J. Zhou, X. Feng and B. Wang, *Journal of the American Chemical Society*, 2017, **139**, 4258-4261.
21. K. Zhang, C. Guo, Q. Zhao, Z. Niu and J. Chen, *Advanced Science*, 2015, **2**, 1500018.
22. Z. Song, Y. Qian, X. Liu, T. Zhang, Y. Zhu, H. Yu, M. Otani and H. Zhou, *Energy & Environmental Science*, 2014, **7**, 4077-4086.

SUPPORTING INFORMATION

Materials and Reagents:

Toluene, dichloromethane (DCM), and tetrahydrofuran (THF) were purchased from J.T. Baker and purified by vigorous purging with argon for 2 hours, followed by passing through two packed columns of neutral alumina under argon pressure. BrettPhos (96%), BrettPhos Pd G3 (95%), RuPhos (95%), RuPhos Pd G2, sodium *tert*-butoxide (NaO*t*Bu), potassium *tert*-butoxide (KO*t*Bu), methylamine (40% in water), hydrazine (anhydrous), 4,4-dibromobiphenyl, 4-bromo-*N,N'*-dimethylaniline (97%), *N*-methyl-aniline, 1,4-dibromobenzene (98%), and copper powder (99%) were purchased from Sigma Aldrich and used as received. 4,4'-dibromobiphenyl (98%), 1,4-dibromobutane (99%), phenothiazine (98%+), iodomethane (99.5%), and methylamine (2M in THF) were purchased from Alfa Aesar, and used as received. Anhydrous magnesium sulfate was purchased from EMD Chemicals. *N*-Bromosuccinimide (NBS) was purchased from Oakwood Chemicals and recrystallized from DI water before use. Sodium sulfite was purchased from Fischer Scientific. Tetrabutylammonium perchlorate was purchased from TCI American (>98%) and recrystallized from ethyl acetate three times to obtain white crystals. Acetonitrile (ACS Grade), from Fischer Scientific, was dried over activated 4 Å molecular sieves. 1-Methyl-2-pyrrolidinone (NMP, anhydrous, 99.5%) was purchased from Sigma Aldrich and used without further purification.

General Analytical Information:

Nuclear magnetic resonance (NMR) spectra were recorded on a Mercury 300 MHz, a Varian 400 MHz, or a Bruker 500 MHz. Infrared spectra were recorded on a

Bruker Hyperion FT-IR Spectrometer with an ATR objective. Gel Permeation Chromatograms were acquired on a Waters Ambient Temperature GPC. THF was used as the eluent and number-average molecular weights (M_n), weight-average molecular weights (M_w), and dispersities (Đ) were calculated from refractive index chromatograms against polystyrene standards.

All electrochemical measurements were performed in a three-compartment glass cell with medium porosity glass frits separating the compartments. An Ag/Ag^+ reference electrode and a Pt wire counter electrode were used, unless otherwise specified. All potentials are referenced to an Ag/Ag^+ reference electrode, which is 0.50 V vs NHE. All 3-mm glassy carbon (GC) electrodes were homemade, in which a glassy carbon slug was press-fitted into a Teflon casing. Prior to the experiment, solutions were subjected to 10 minutes of sparging with Ar or N_2 to prevent undesirable side-reactions and oxygen reduction over the applied potential window.

The following procedure was taken to clean GC electrodes before use. Electrodes were sonicated in ethanol for 30 seconds before polishing with diamond paste and MetaDi Fluid (Buehler). Following polishing, the electrodes were sonicated in ethanol again for 30 seconds and dried with an IR lamp.

Electrochemical Tests:

Electrochemical measurements were carried out in CR 2032 coin cells assembled in an argon filled glove box (residual water and oxygen were 0.5 ppm and 0.1 ppm, respectively) with lithium metal as the anode. The working cathode was fabricated with 30 wt% active material, 60 wt% Super P carbon, and 10 wt% poly(vinylidene

fluoride) (PVDF) as binder. The high loading cathode was fabricated with 75 wt% active material, 15 wt% Super P carbon, and 10 wt% poly(vinylidene fluoride) (PVDF) as binder. The resulting slurry was coated onto a carbon paper current collector. The coated electrode was dried for 12 h at 100 ^{o}C in a vacuum oven. The counter electrode was Li metal. The two electrodes were separated by a polypropylene separator (Celgard 2300). The electrolyte was 1.0 M $LiPF_6$ in a 1:1 ratio of EC (ethylene carbonate) to DEC (diethyl carbonate). Galvanostatic charge/discharge of the coin cells was carried out using an Arbin BT-2000 battery tester with a constant charge-discharge current rate and a voltage range of 2.8 to 4.3 V vs. Li/Li^+ at 25 °C.

Electrochemical Impedance Spectroscopy (EIS):

Electrochemical impedance spectroscopy measurements using a Solartron 1280-B potentiostat, were performed on a lithium coin cell with PT-DMPD (10% CL) as cathode. Impedance measurements were taken at 3.1, 3.3, 3.6, 3.9 and 4.1 V vs. Li/Li+ after 3600 s of pretreatment at the respective potentials from 0.001 - 20000 Hz. AC amplitude of the measurements were 10 mV.

Slurry Preparation:

2.0 mg of bulk polymer, 2.5 mg of carbon black and 0.5 mg of PVDF were mixed in a 5 mL vial with 1 mL NMP. Such a composition yields a composite loading of 5 mg mL^{-1}. The mixture was sonicated for 1 h until the mixture was homogenously dispersed in solvent, 10 µL of ink were drop-casted onto the GC surface to create a polymer loading of 0.28 mg cm^{-2}. Even though the powdered polymers were insoluble in conventional organic solvents, when oxidized the polymers become slightly soluble in EC/DEC, as the slurry on the GC dissolved as the materials became oxidized. Since

materials were lost during cycling, scan rate dependence and other quantitative analysis were not performed on CVs obtained from slurries.

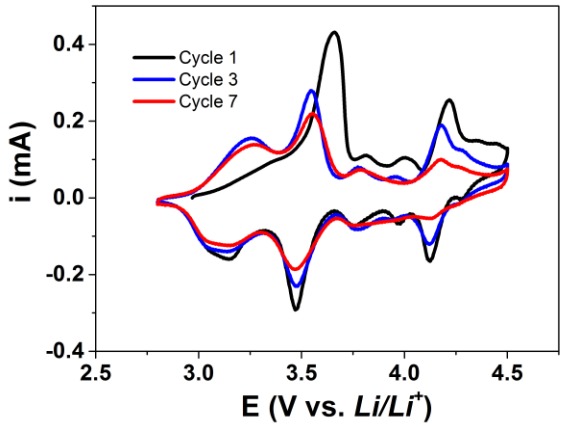

Figure 5-S1: CV cycling over the full potential window of 10% CL PT-DMPD in 1 M $LiPF_6$ in EC/DEC in a coin cell at 0.2 mVs^{-1}. In the 1st cycle, there is likely a kinetic barrier in "breaking in" the electrode material to be incorporated with anions in the first cycle, as the total charge in the first cycle approximates the charge involved in the first two redox processes in subsequent cycles.

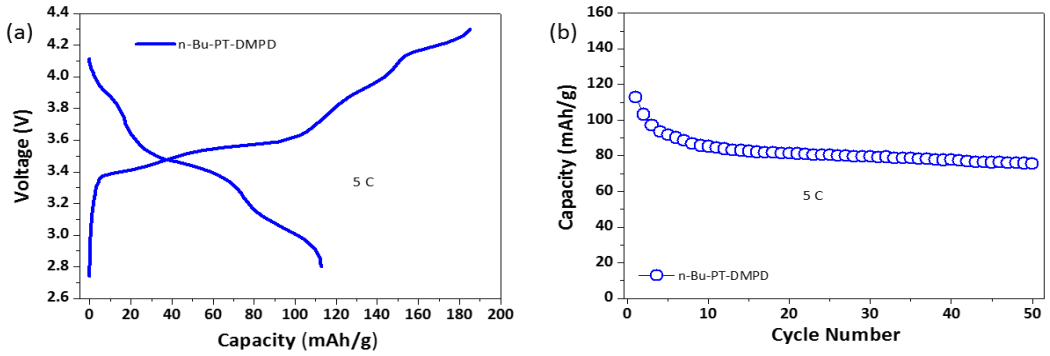

Figure 5-S2: Poly(*N*-*n*butylphenothiazine dimethylphenylenediamine) (nBuPT-DMPD) was synthesized in an attempt to make soluble derivatives of PT-DMPD polymers for more complete characterization. Detailed synthesis and characterization of nBuPT-DMPD are presented in the synthesis section later in the SI. (a) Initial charge–discharge curves of the nBuPT-DMPD cell at 5 C between 2.8 and 4.3 V. (b) Cycling performance of the nBuPT-DMPD cell at 5 C between 2.8 and 4.3 V.

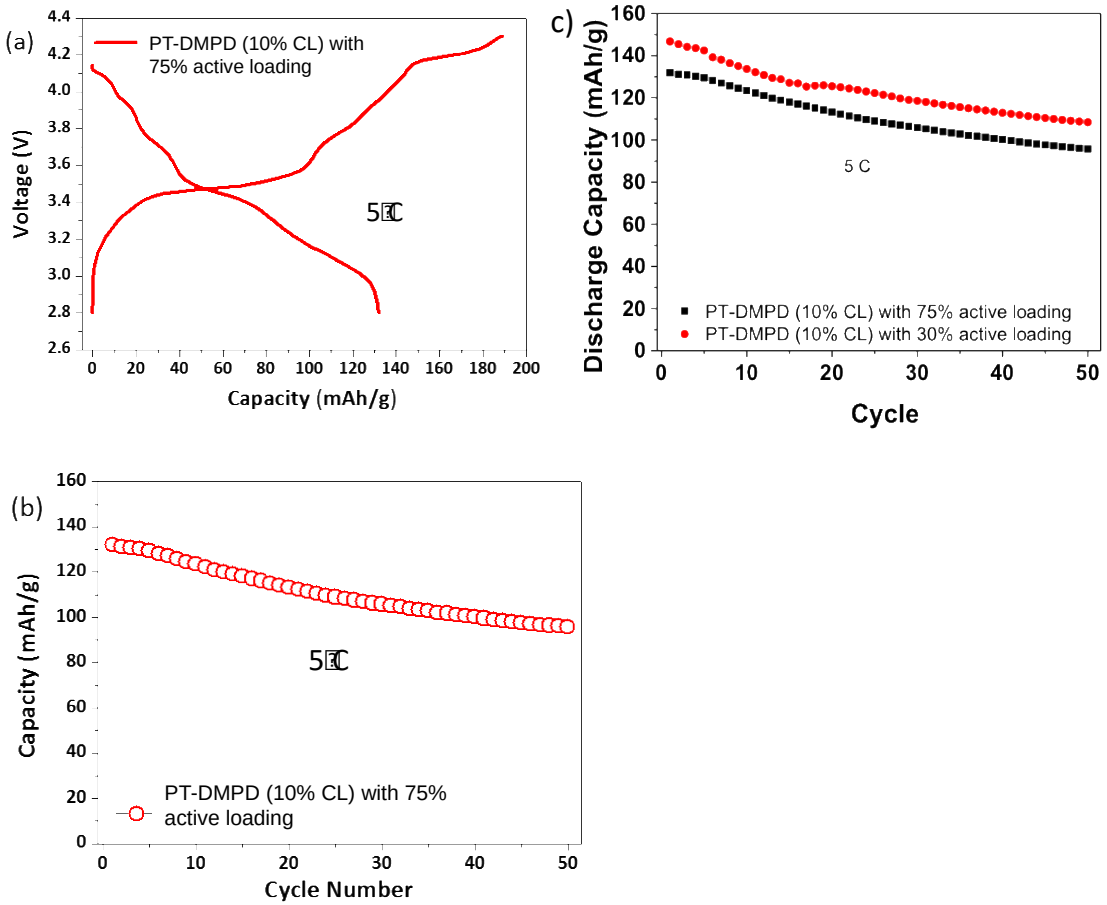

Figure 5-S3: (a) Initial charge–discharge curves of the PT-DMPD (10% CL) cell with 75% active material loading at 5 C between 2.8 and 4.3 V. (b) Cycling performance of the PT-DMPD (10% CL) cell with 75% active loading at 5 C between 2.8 and 4.3 V. (c) Cycling of PT-DMPD (10% CL) cell with 75% active loading at 5C and PT-DMPD (10% CL) cell with 30 % active loading at 5 C.

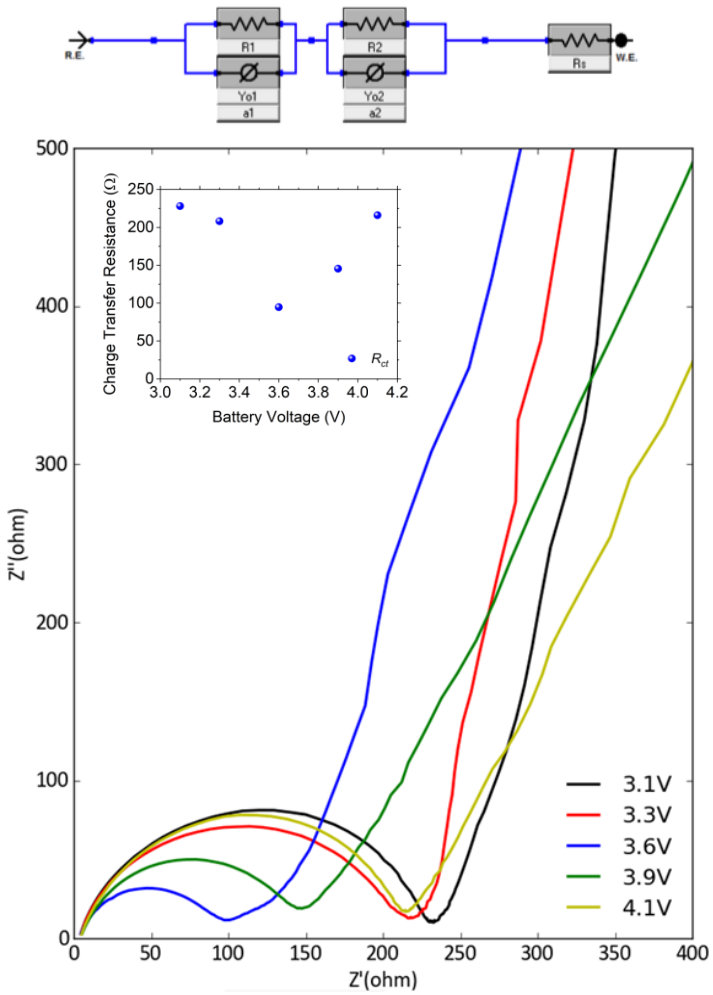

Figure 5-S4: Top panel: Equivalent circuit model for electrochemical impedance spectroscopy data. Middle panel: Electrochemical impedance spectroscopy performed on a typical coin cell using PT-DMPD (10% CL) as cathode material. Impedance of the device at 3.1, 3.3, 3.6 3.9 and 4.1 V were measured after 3600 s of potentiostatic pretreatment from 0.001 – 20000 Hz. Inset shows the charge transfer resistance (R_{ct}) as a function of potential of the device.

Rates	PT-DMPD (10% CL)		PT-DMPD (33% CL)	
	Discharge capacity (mAh/g)	Capacity retention (%)	Discharge capacity (mAh/g)	Capacity retention (%)
1 C	149.4	100	147.5	100
5 C	146.4	98.0	143.5	97.3
10 C	141.9	95.0	138.0	93.6
20 C	138.9	93.0	134.9	91.5
40 C	134.7	90.2	127.8	86.6
60 C	131.5	88.0	118.3	80.2
120 C	122.3	81.9	100.0	67.8

Table 5-S1: Discharge capacities of the PT-DMPD (10% CL) sample and the PT-DMPD (33% CL) sample at different rates and the corresponding capacity retentions (Note: retention at 1 C is defined as 100%).

CHAPTER 6

ELUCIDATION OF REDOX MECHANISMS OF PHENOTHIAZINE-DERIVATIZED REDOX-ACTIVE MAIN-CHAIN POLYMERS AS A HIGH-ENERGY CATHODE FOR ENERGY STORAGE[x]

6-1. Introduction

In this manuscript, we delve deeper into the electrochemical behavior of redox-active main-chain polymer cathodes. In order to rationally improve the properties of our materials as electrode materials, a fundamental understanding of their electrochemical properties is indispensable. Specifically, understanding the origin of theoretical capacity, as well as understanding the mechanisms of the observed redox events are paramount for assessing the performance and stability of polymeric cathodes. Herein, we report on the synthesis and elucidation of the electrochemical properties of a class of high-energy PT-based polymers for LIBs. We provide strong evidence as to the distinct redox states that the polymer underwent, observation of the presence of redox-active end-groups as well as the calculation of their theoretical capacities based on cyclic voltammetry, model compound studies and electrochemical quartz crystal microbalance studies.

6-2. Polymer Design and Synthesis

It has been known that for organic materials electrochemical events occur primarily at heteroatoms, and as a result incorporation of heteroaromatic compounds

[x] This chapter was reproduced in part with permission from Shen, L.; Peterson, B.; Ren, D.; Wu, Y.-C. M.; Fors, B. P.; Abruña, H. D. Elucidation of Redox Mechanism of Phenothiazine-Derivatized Redox-Active Main-Chain Polymers as A High-Energy Cathode for Energy Storage. *Manuscript in prepration.*.

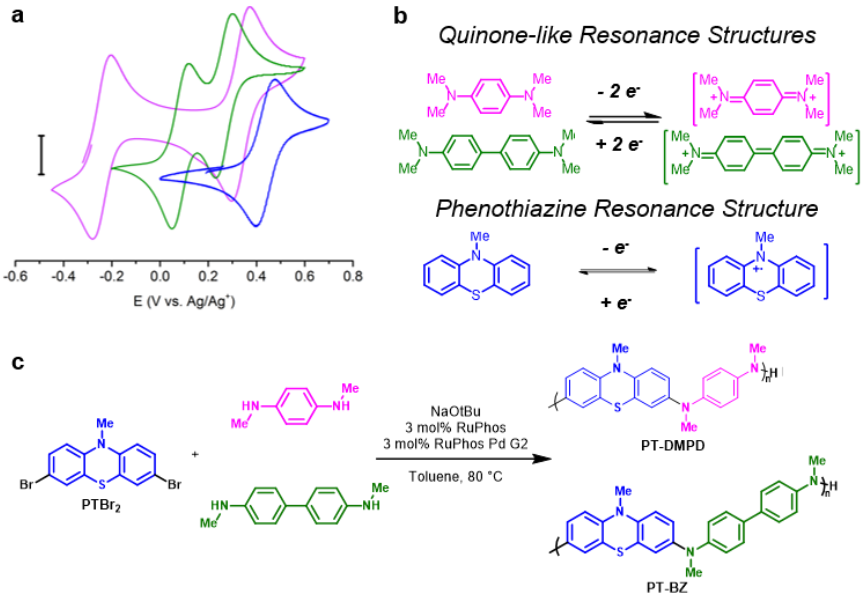

Figure 6-1. a) Monomer scans of TMPD (pink), BZ (green) and PT (blue) at 1 mM in 0.1 M TBAP/MeCN at 20 mVs^{-1}(scale bar 5 µA). b) Origin of chemical stability of TMPD, BZ and PT upon oxidation. c) The facile synthesis of PT-TMPD and PT-BZ polymers via Buckwald-Hartwig coupling polymerization.

into polymer backbone has been the focus of designing high-energy redox-active polymers. PT has recently gained attention in both electroluminescence and solar cell applications.[1-6] It exhibits a highly reversible redox couple at 0.4 V vs. Ag/Ag^+ (Figure 6-1a, 6-S1f), making it a highly promising candidate for such applications. On the other hand, TMPD and BZ have been studied as redox-active moieties previously[7-10], and both species are known to exhibit two chemically and electrochemically reversible redox couples at ca. 3.0 – 4.0 V vs. Li/Li^+ (Figure 6-S1c and d) as they undergo a quinoidal resonance structure during oxidation (Figure 6-1b).

When designing cathode materials with high energy density, we attempt to minimize molecular weight while enabling access to multiple electrons. Direct incorporation of PT with either TMPD or BZ into a polymer main-chain satisfies both criteria, yielding optimal theoretical energy densities. The resulting PT-DMPD and PT-BZ polymers were expected to exhibit up to three-electron oxidations per repeating unit (Figure 6-2b), reflected in theoretical capacities as high as 233 $mAhg^{-1}$ (233 $mAhg^{-1}$ for PT-DMPD and 191 $mAhg^{-1}$ for PT-BZ). Additionally, as all three of the redox components undergo oxidation between 3.0 – 4.0 V vs. Li/Li^+, the energy density of the polymers approaches 815 Whg^{-1}, assuming a working voltage of 3.5 V, yielding one of the highest energy densities for organic electrodes.[11]

PT-DMPD and PT-BZ were synthesized via facile Buchwald-Hartwig coupling of 3,7-Dibromo-*N*-methylphenothiazine with *N,N'*-dimethylphenylenediamine or *N,N'*-dimethylbenzidine (Figure 6-1c). [12, 13] During polymerization, polymer chains became insoluble in the reaction solvent and precipitated from solution, and the resulting polymers collected were insoluble in

conventional organic solvents. Elemental analysis estimated the average molecular weight of the PT-DMPD based on a percent bromide end-groups of 2.05%. Assuming a stochastic distribution of polymer end groups, this corresponds to an average molecular weight of 3.8 kg/mol, which corresponds to a degree of polymerization of about 12.

Synthesis was performed in xylene and mesitylene at higher reaction temperatures in an attempt to increase the degree of polymerization, yet as concluded by elemental analysis, no change in molecular weight was observed. Attempts to solubilize the polymer by incorporating *N*-alkyl side-chains to the PT in the polymer yielded a still stiff, rubbery and insoluble polymer, inaccessible for further processing.

6-3. Solid-State Electrochemical Characterization

As solution-phase molecular characterization proved difficult, solid-state electrochemical characterization was performed on these polymers. The bulk polymers were processed into slurry inks, and slurry pastes of polymers were mixed with Super P carbon and polyvinylidene fluoride (PVDF) to form a homogeneous ink/paste in *N*-methylpyrollidone (NMP). The ink was then dropcast onto a clean glassy carbon (GC) electrode (Figure 6-2a).

The resulting slurry paste of the bulk polymer was characterized using cyclic voltammetry (CV). Slurries of the powder polymer exhibit extraordinary electrochemical properties in CV, as multiple redox couples appeared for both PT-DMPD and PT-BZ bulk polymers in 0.1 M tetrabutylammonium perchlorate/acetonitrile (TBAP/MeCN) electrolyte (Figure 6-2c and 6-2d,

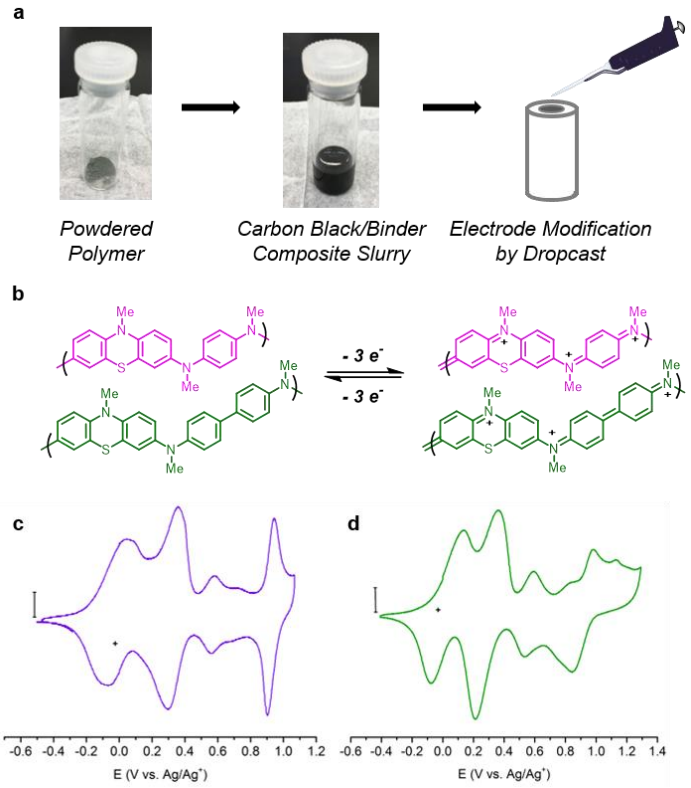

Figure 6-2. a) Schematic of the preparation of slurry inks of bulk polymers. b) Stable resonance structures of PT-TMPD and PT-BZ bulk polymers undergoing oxidation; these structures show that the maximum number of electrons exchanged per repeating unit is three electrons. c) Slurry CV of PT-TMPD (scale bar 10 µA) PT-BZ (scale bar 25 µA) in 0.1 M TBAP/MeCN at 20 mVs^{-1}.

respectively). In fact, the CV profiles of both polymers are in good agreement, indicating a highly similar electronic environment in these polymers during their respective redox reactions.

Three main redox couples were observed between –0.5 and 1.0 V in both polymers voltammograms (Figure 6-2c and 6-2d); a large amount of charge was involved with each redox activity, suggesting potentially high-energy cathode materials. In both CV profiles, the redox couple at the lowest potential exhibited the most diffusive characteristics, typical of the transition between neutral and charged states of a redox-active material. The additional redox couples had much smaller ΔE_{pk} values, typical of transitions between further charged states. Three redox couples present in the CV are in good agreement with our hypothesis of the resonance structures of the polymers when fully oxidized (Figure 6-2b).

As synthesized PT-DMPD and PT-BZ bulk polymers are proposed as cathode materials for EES. Calculating their theoretical capacities and understanding their redox mechanisms are paramount for assessing the stability and properties of such materials. A central question in elucidating their redox behaviors relates to how many electrons were exchanged per repeat unit. While device performance metrics are important, it is also paramount that we answer these questions and elucidate the redox mechanisms of this class of materials.

6-4. Model Compound for PT-DMPD

Main-chain polymers exhibiting complicated redox behaviors are ubiquitous, and researchers have used various strategies to elucidate the redox mechanisms of

main-chain polymers in attempt to identify and assign redox functionalities.[14-18] One way is to observe the convergence of electrochemical behaviors from monomer to polymer.[17, 19] We studied the electrochemical behavior of PT-DMPD assuming a generalization of small molecule electrochemistry to their polymer equivalent.[16] By analyzing electronic absorption patterns of the model compound of PT-DMPD during its redox activity, we were able to characterize the redox-active moiety associated with reach redox state, approximating the redox activity in PT-DMPD polymers.

A small molecule analogue of PT-DMPD was synthesized, PT-$(TMPD)_2$, and the CV of this small molecule exhibited a remarkable set of five observable redox couples over the potential window from – 0.5 to 1.1 V (Figure 6-3b). Furthermore, we spectrochemically characterized the discrete oxidized species via *in situ* measurements, assigning each redox couple with a set of electronic absorptions (Figure 6-3c). Spectroscopic results suggest that between the six distinct redox states of this model compound, a set of distinct electronic absorption pattern can be assigned to each of them. At neutral state, PT-$(TMPD)_2$ exhibits absorption at 263 and 328 nm, an absorption pattern similar to those of phenothiazine derivatives rather than phenylenediamines.[2, 20-22] Absorptions at 270, 288 and 975 nm were present for the monocation radical of PT-$(TMPD)_2$. This cation radical exhibits low-energy absorption characteristic of cation radical (500-1000 nm)[23, 24], and is unlikely to be attributed to phenylenediamine moieties as phenylenediamine monocation radicals generally exhibit low-energy absorptions between 500-900 nm.[20, 21] The +2 and +3 states of PT-$(TMPD)_2$ shows identical electronic absorption patterns at 263, 329, 377

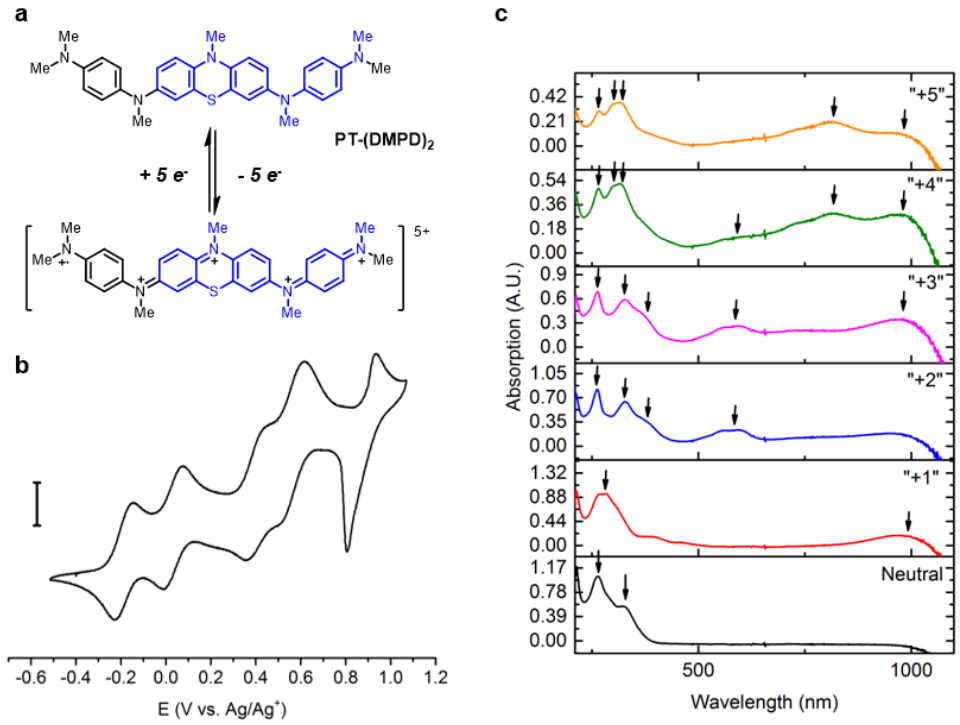

Figure 6-3. a) Stable resonance structure of PT-$(TMPD)_2$ during oxidation. As shown, the maximum number of electrons extracted is five for this monomer, suggesting that three is the maximum number of electrons that can be extracted from the PT-TMPD polymer per repeating unit. b) CV showing the redox behavior of 0.5 mM PT-$(TMPD)_2$ in 0.1 M TBAP in 1:1 MeCN/DCM at 20 mVs^{-1} (scale bar 5 uA). c) Spectroelectrochemistry of the electronic absorption pattern of PT-$(TMPD)_2$ during oxidation at each redox state. Arrows indicate the major absorptions at that redox state.

and 578 nm; the lowest energy absorption is similar to the monocation absorption pattern of phenylenediamine derivatives at long wavelengths.[20, 21] The absorption pattern of +4 and +5 occurs at 266, 300, 321, and 851 nm; of which the low-energy absorption again shows similarity to that in phenylenediamine dications.[20, 21] Based on the above observations, electronic absorption patterns of PT-$(TMPD)_2$ suggests that in this model compound, the similar absorption at +2/+3 and +4/+5 could be due to the oxidation of the symmetric phenylenediamine units on the 2, 7-position of the phenothiazine. In adition, the phenothiazine moiety is likely the first redox center to be oxidized, which is then closely followed by the consecutive oxidation of phenlyenediamine moiety to its monocation then to its dication.

6-5. *Electropolymerization of Thin-Film PT-BZ and End-Group Analysis*

While we used model compound to model the redox activity of PT-TMPD, a different strategy was employed to study the parent polymer, PT-BZ. The electrochemical dimerization of aniline into benzidine has been well-documented and extensively utilized in thin-film formation of benzidine-containing polymers.[8, 18] Using the same principle, a PT-BZ thin-film polymer was electropolymerized from a phenothiazine-aniline (PT-$(Ani)_2$, Figure 6-4a) monomer, allowing for thin-film characterization methods for the study of PT-BZ polymers. The electropolymerzation mechanism of PT-$(Ani)_2$ into thin-film PT-BZ was characterized spectro- and electrochemically. The monomer exhibited two highly reversible waves at 0.00 and 0.25 V, and polymerization occured when the monomer was triply oxidized at ca. 1.3 V (Figures 6-4a, b). The coupled (oligomerized) species was detected by CV at low

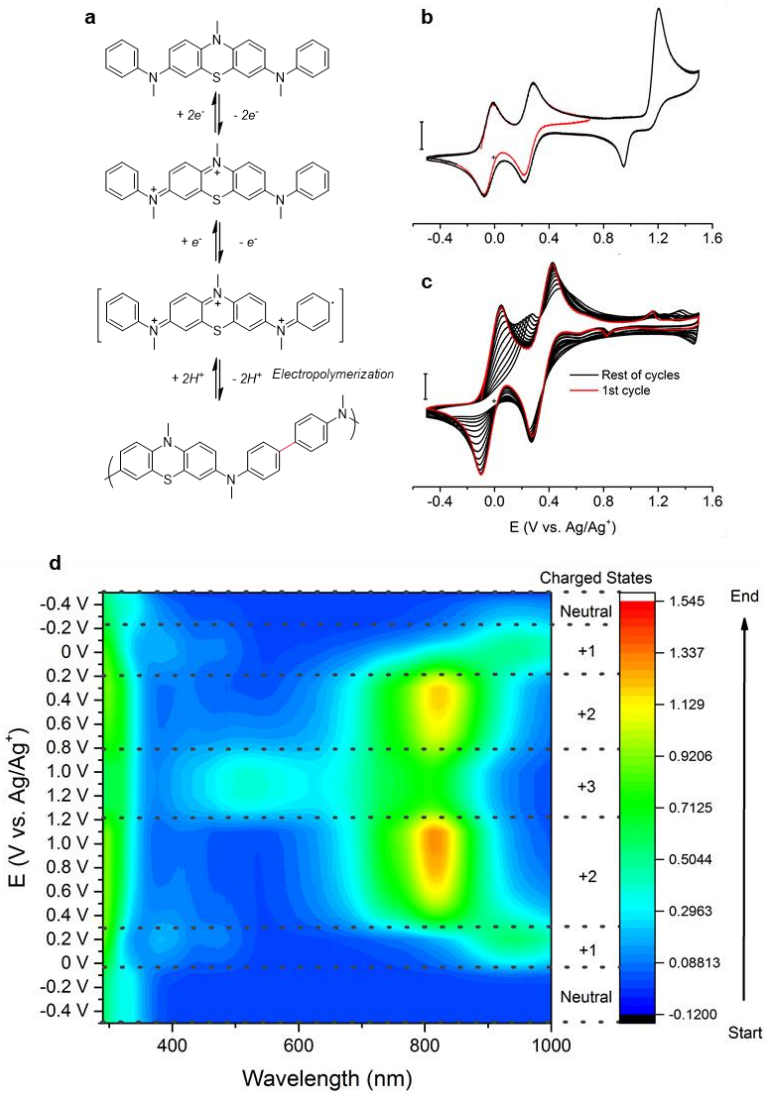

Figure 6-4. a) Proposed mechanism of electropolymerization of PT-$(Ani)_2$ to form thin-film PT-BZ polymer. b) CV profile of PT-$(Ani)_2$ at 0.5 mM in 0.1 M TBAP/MeCN (scale bar 10 uA); small window (red) vs. full window (black). c) Electropolymerization of PT-$(Ani)_2$ at 10 mM in 1 M TBAP/DCM at 50 mVs-1 on a GC electrode (scale bar 20 µA). The peak at ca. 1.2 V appear adsorptive compared to that in MeCN at much lower concentration. The continuous increase in current provides clear evidence of deposition on the GC surface. d) Electronic absorptions of each of the redox states of PT-$(Ani)_2$. As the spectra clearly show, the chemically coupled species that occur between the voltage of 1.2 and 0.8 V show a distinct pattern compared to the other redox states. All absorption patterns correspond with the redox states indicated in the simultaneous CV

monomer concentrations in acetonitrile (MeCN) (Figure 6-4b), while in dichloromethane, adsorptive behavior was observed at high concentrations (above 10 mM). Electropolymerization could occur and deposition on substrates could be monitored as the number of electropolymerization cycles increased (Figure 6-4c). The coupling reactions could also be monitored spectroscopically. The neutral, 1+ and 2+ states of the monomer can be clearly seen at potentials before 1.2 and after 0.8 V (Figure 6-4d), and the coupled species was observed between 1.2 – 0.8 V, which was in excellent agreement with the simultaneously recorded CV.

The resulting thin-film PT-BZ polymer exhibit a CV profile that strongly resembles that of the bulk PT-BZ polymer (Figures 6-2d and 6-5c). For example, common to both bulk and thin-film, there were three sets of redox couples at –0.1, 0.25 and 0.9 V, and smaller amplitude redox couples were found near 0.6 – 0.9 V in both forms. From this experiment, we are confident that the electropolymerized thin-film PT-BZ resembles the chemical structure of bulk PT-BZ to a high degree.

A discrepancy in redox behaviors for 0.6 – 0.9 V between the bulk and thin-film PT-BZ called for a deeper analysis of these redox processes. Both bulk PT-DMPD and bulk PT-BZ exhibited two redox couples over this potential region, while thin-film PT-BZ exhibited only one redox couple (Figure 6-5). As two types of redox-active end-groups are present in PT-DMPD and PT-BZ polymers (bromo-end-group and TMPD/BZ-end-group) but one type of end-group is present in thin-film PT-BZ (aniline-end-group), there is a corresponding number of redox couples cover the respective potential windows (Figures 6-5b, c). This qualitative observation is in good agreement with the hypothesis that the small redox couples at 0.6 – 0.9 V can be

attributed to redox-active end-groups in both the bulk polymers and the thin-film polymers.

Having the redox behaviors fully assigned to the respective functionalities, the thin-film dynamics, involving ion incorporation with PT-BZ, using the electrochemical quartz crystal microbalance (*EQCM*), was studied in detail to elucidate the number of electrons involved in the observed redox couples and potential changes in solvation.

6-6. Electrochemical Quartz Crystal Microbalance (EQCM) Studies on PT-BZ

The *EQCM* can monitor mass changes associated with ion movements in a thin-film during electrochemical processes.[13] Many studies have used this method to elucidate transport dynamics in thin-film materials. [25-27] Specifically in our studies, we were interested in separating electrochemical processes from mass changes, as a result the number of electrons, associated with the redox couples could be calculated.

The *EQCM* experiments were divided into two parts: electropolymerization and film cycling, where the first part establishes the mass of polymer film and the second part measures mass of ions incorporated during cycling. Attempts to determine the film's mass by comparing the frequency changes of the QCM electrode under dry conditions as reported previously[28] was proven unsuccessful. Polymer film mass was established by the frequency difference of the QCM electrode in solution, with stabilization before and after the electropolymerization. For twenty cycles of electropolymerization, 2-6 μg of film were usually deposited in a typical electropolymerization experiment (Figure 6-6a). Typically, a film generated by twenty

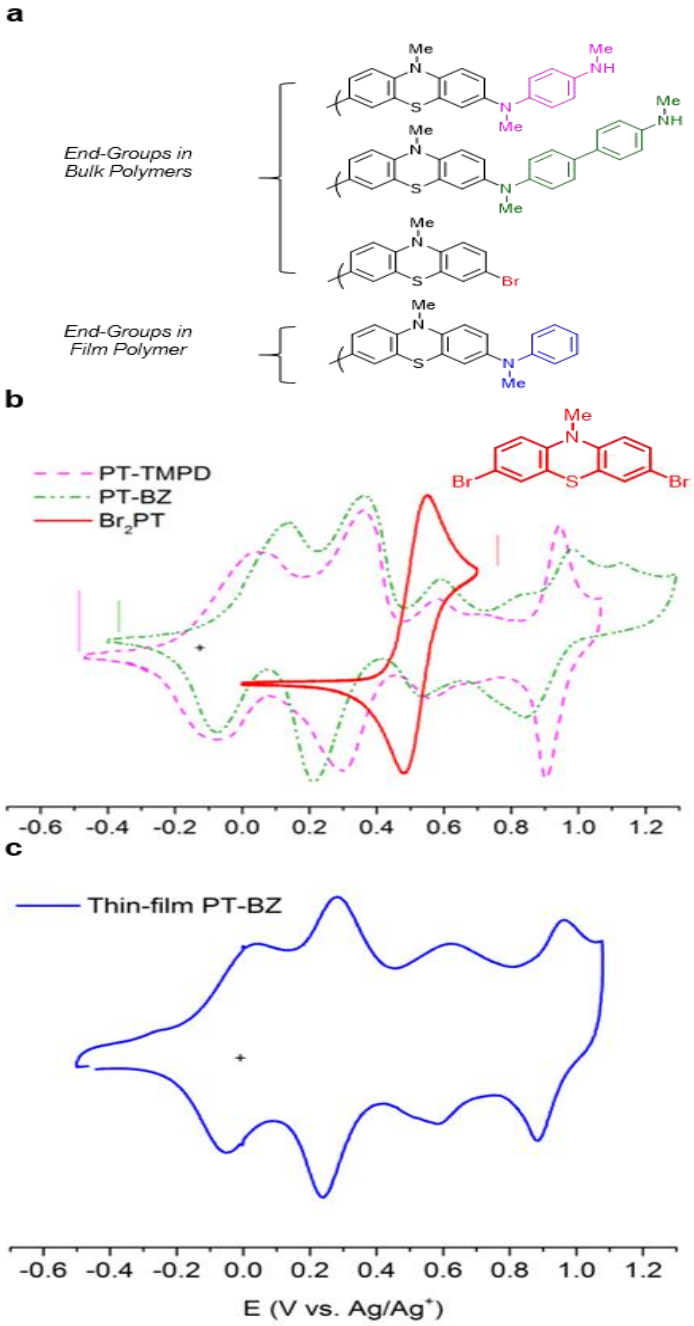

Figure 6-5. a) The possible end-groups in bulk PT-TMPD, PT-BZ and thin-film PT-BZ. b) Superimposed with PT-TMPD (scale bar 20 µA) and PT-BZ 20 µA) bulk polymers, PT-Br_2 (scale bar 2.5 µA) monomer shows a redox couple at 0.55 V, within the window of the small redox shoulders. c) CV of thin-film PT-BZ polymer in 0.1 M TBAP/MeCN.

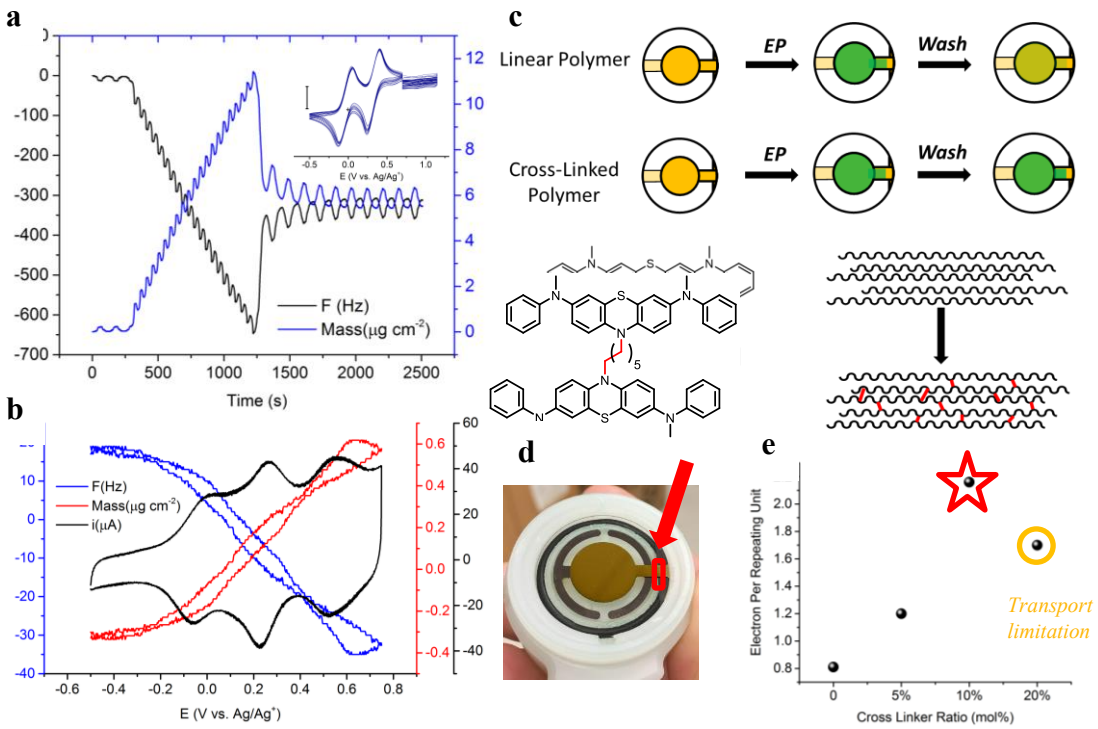

Figure 6-6. a) The frequency and mass change during electropolymerization of PT-$(Ani)_2$ on QCM Au electrode. Inset shows the CV profile during the electropolymerization (10 mM PT-$(Ani)_2$ in 1 M TBAP/DCM, 500 uA). b) The simultaneous change in frequency and mass during cycling of thin-fiilm PT-BZ in 0.1 M TBAP/MeCN at 20 mVs^{-1}. c) Schematic demonstrating the hypothesis that, for a linear polymer, it might be more prone to washing during film and electrode cleaning after electropolymerization, hence lowing the mass of polymer deposited. By having a cross-linked network, the film might adhere better to the electrode, retaining most of the thin-film deposited. d) Thin-film PT-BZ deposition on a Au QCM electrode; red square indicates the edge of the film and electrode. e) The number of electron exchanged during film cycling as a function of the amount of cross-linker added during electropolymerization. The optimal amount of cross-linker is shown to be 10%, as it shows the highest number of electron exchanged.

cycles of electropolymerization yields a film-thickness of approximately 40 – 50 nm and 100 nm for fifty cycles.

The dynamics of electropolymerization were also monitored by the EQCM. While currents corresponding to the first two redox couples were pronounced, the large frequency decrease accompanying the third redox couple confirmed electropolymerization and film deposition (Figure 6-6a). During the elecropolymerization cycles, the third redox process was repeatedly cycled, leading to a speedy and rapid increase of mass on the QCM (Figure 6-6a), indicative of steady film deposition.

Following the completion of electropolymerization, the thin-film PT-BZ was subjected to potential cycling in blank electrolyte. During film cycling, frequency and mass changes are associated with anion movements across the polymer film (Figure 6-6b). Simultaneous resistance measurements indicated that the viscoelastic properties were not significantly altered during film cycling (within 5 Ω range with no particular parttern), confirming the rigid film properties of the resulting polymer film, allowing for the direct application of the Sauerbrey equation.

One key limitation of this technique in this specific case was the use of Au electrode. Since potentials higher than 0.8 V cause Au oxidation, hence the accessible potential window was limited to -0.5 – 0.75 V, thus we could only study the first two redox couples and end-groups while extrapolotaing the last redox couple. Initial tests indicated that only about 0.8 electrons per repeat unit were exchanged within the above mentioned potential window (Figure 6-6e). This result is in contrast with the two electrons exchanged over the same potential window as suggested by CV analysis.

Film cycling with ferrocene as a screening redox shuttle showed no signs of unclogging and improvement of film accessibility (Figure 6-S5), indicating that the polymer film was not charged-trapped nor electrochemically unaccessible. The other possibility was that, washing the films with solvents could part of the film from the substrate. This would lead to an underestimation of electrons per repeat unit by overestimating film mass.

In order to mitigate polymer film film dissolution, a cross-linker was employed at small percentages (Figure 6-6c). Upon incorporation of cross-linkers in the EQCM experiments, no differences were noted during electropolymerization or film cycling (Figure 6-6c). With incremental additions of the cross-linker into the electropolymerization solution, the number of anions intercalated peaked at 10 mol% cross-linker, showing 2.17 electrons exchanged per repeating unit. However, it dropped dramatically at higher cross-linker concentration (20 mol%), likely due to counter ion transport limitation from the highly cross-linked network (Figure 6-6e). This is evidence that for the first two redox couples and end-group, a set of two electrons are exchanged, and extrapolating to the full potential window, we can confidently expect three electrons per repeating unit.

6-7. Conclusion

In this manuscript, we have elucidated the redox mechanism of a class of high energy-density polymeric cathode materials for EES applications. PT-DMPD and PT-BZ, as redox-active main-chain polymers, were shown to be insoluble in conventional organic solvents. Solid-state slurry pastes of these polymers indicate three main redox

events between 3.0 – 4.5 V vs. *Li/Li*$^+$, implying extraordinary energy density. A small molecule model compound of PT-DMPD showed a maximum number of three redox processes within the potential window probed, per repeating unit. EQCM experiments of PT-BZ thin-film indicated a set of two redox processes between 3.0 – 4.2 vs. Li/Li$^+$, with an estimated additional redox event at up to 4.5 V. This study has presented convincing evidence to establish the redox mechanism of PT-DMPD and PT-BZ films that are in close agreement with their practical performance obtained at device level characterization. The results validate our rational approach to design, characterization and testing of new polymeric materials. Our studies revealed exceptional insights and understanding of the promise of these materials for EES applications.

REFERENCES

1. Z. Gomurashvili and J. V. Crivello, *Macromolecules*, 2002, **35**, 2962-2969.
2. X. Kong, A. P. Kulkarni and S. A. Jenekhe, *Macromolecules*, 2003, **36**, 8992-8999.
3. F. Fungo, S. A. Jenekhe and A. J. Bard, *Chemistry of Materials*, 2003, **15**, 1264-1272.
4. A. A. Golriz, T. Kaule, M. B. Untch, K. Kolman, R. Berger and J. S. Gutmann, *ACS Applied Materials & Interfaces*, 2013, **5**, 2485-2494.
5. A. A. Golriz, T. Suga, H. Nishide, R. Berger and J. S. Gutmann, *RSC Advances*, 2015, **5**, 22947-22950.
6. Y.-J. Cheng, S.-H. Yang and C.-S. Hsu, *Chemical Reviews*, 2009, **109**, 5868-5923.
7. S. Conte, G. G. Rodriguez-Calero, S. E. Burkhardt, M. A. Lowe and H. D. Abruna, *RSC Advances*, 2013, **3**, 1957-1964.
8. T.-T. Truong, G. W. Coates and H. D. Abruna, *Chemical Communications*, 2015, **51**, 14674-14677.
9. H. Yang, D. O. Wipf and A. J. Bard, *Journal of Electroanalytical Chemistry*, 1992, **331**, 913-924.
10. T. Mizoguchi and R. N. Adams, *Journal of the American Chemical Society*, 1962, **84**, 2058-2061.
11. T. B. Schon, B. T. McAllister, P.-F. Li and D. S. Seferos, *Chemical Society Reviews*, 2016, **45**, 6345-6404.
12. B. P. Fors, D. A. Watson, M. R. Biscoe and S. L. Buchwald, *Journal of the American Chemical Society*, 2008, **130**, 13552-13554.
13. B. P. Fors, N. R. Davis and S. L. Buchwald, *Journal of the American Chemical Society*, 2009, **131**, 5766-5768.
14. H. Etori, T. Kanbara and T. Yamamoto, *Chemistry Letters*, 1994, **23**, 461-464.
15. P. Nguyen, P. Gómez-Elipe and I. Manners, *Chemical Reviews*, 1999, **99**, 1515-1548.

16. K. Naka, T. Uemura and Y. Chujo, *Macromolecules*, 2000, **33**, 6965-6969.
17. R. Rulkens, A. J. Lough and I. Manners, *Journal of the American Chemical Society*, 1994, **116**, 797-798.
18. D. Wei, C. Kvarnström, T. Lindfors, L. Kronberg, R. Sjöholm and A. Ivaska, *Synthetic Metals*, 2006, **156**, 541-548.
19. R. Rulkens, A. J. Lough, I. Manners, S. R. Lovelace, C. Grant and W. E. Geiger, *Journal of the American Chemical Society*, 1996, **118**, 12683-12695.
20. K. Yuan Chiu, T. Xiang Su, J. Hong Li, T.-H. Lin, G.-S. Liou and S.-H. Cheng, *Journal of Electroanalytical Chemistry*, 2005, **575**, 95-101.
21. S. J. Yeh, C. Y. Tsai, C.-Y. Huang, G.-S. Liou and S.-H. Cheng, *Electrochemistry Communications*, 2003, **5**, 373-377.
22. A. P. Kulkarni, P.-T. Wu, T. W. Kwon and S. A. Jenekhe, *The Journal of Physical Chemistry B*, 2005, **109**, 19584-19594.
23. M. Burgess, E. Chénard, K. Hernández-Burgos, G. Nagarjuna, R. S. Assary, J. Hui, J. S. Moore and J. Rodríguez-López, *Chemistry of Materials*, 2016, **28**, 7362-7374.
24. J. C. Barnes, A. C. Fahrenbach, S. M. Dyar, M. Frasconi, M. A. Giesener, Z. Zhu, Z. Liu, K. J. Hartlieb, R. Carmieli, M. R. Wasielewski and J. F. Stoddart, *Proceedings of the National Academy of Sciences*, 2012, **109**, 11546.
25. R. Borjas and D. A. Buttry, *Chemistry of Materials*, 1991, **3**, 872-878.
26. A. R. Hillman, D. C. Loveday and S. Bruckenstein, *Langmuir*, 1991, **7**, 191-194.
27. J. John, K. M. Hugar, J. Rivera-Meléndez, H. A. Kostalik, E. D. Rus, H. Wang, G. W. Coates and H. D. Abruña, *Journal of the American Chemical Society*, 2014, **136**, 5309-5322.
28. D. Orata and D. A. Buttry, *Journal of the American Chemical Society*, 1987, **109**, 3574-3581.

SUPPORTING INFORMATION

Materials and Reagents:

Toluene, dichloromethane (DCM), and tetrahydrofuran (THF) were purchased from J.T. Baker and was purified by vigorous purging with argon for 2 h, followed by passing through two packed columns of neutral alumina under argon pressure. BrettPhos (96%), BrettPhos Pd G3 (95%), RuPhos (95%), RuPhos Pd G2, sodium *tert*-butoxide (NaO*t*Bu), potassium *tert*-butoxide (KO*t*Bu), methylamine (40% in water), hydrazine (anhydrous), 4,4-dibromobiphenyl, 4-Bromo-*N,N'*-dimethylaniline (97%), methylaniline, 1,4-dibromobenzene (98%), and copper powder (99%) were purchased from Sigma Aldrich. 4,4'-dibromobiphenyl (98%), 1,4-dibromobutane (99%), phenothiazine (98%+), iodomethane (99.5%), and methylamine (2M in THF) were purchased from Alfa Aesar, and used as received. Anhydrous magnesium sulfate was purchased from EMD Chemicals. *N*-Bromosuccinimide (NBS) was purchased from Oakwood Chemicals and recrystallized from DI water before use. Sodium Sulfite was purchased from Fischer Scientific. Tetrabutylammonium perchlorate was purchased from TCI American (>98%), recrystallized from ethyl acetate three times to obtain white crystals. Acetonitrile (ACS Grade), from Fischer Scientific, was dried over activated 4 Å molecular sieves. 1-Methyl-2-pyrrolidinone (NMP, anhydrous, 99.5%) was purchased from Sigma Aldrich and used without further purification.

General Analytical Methods:

Nuclear magnetic resonance (NMR) spectra were recorded on a Mercury 300 MHz, a Varian 400 MHz or a Bruker 500 MHz. Monomer characterization and electropolymerization of PT-$(Ani)_2$ performed on GC were performed on a Hokuto Denko HABF1050m potentiostat/galvanostat controlled by LabView program. The results of electrochemical experiments on UV-vis spectroelectrochemistry and electrochemical quartz crystal microbalance (EQCM) were recorded on a VersaSTAT 3 processed with VersaStudio software. All UV-vis spectroscopy experiments were carried out using an Agilent/HP 8453 UV-visible spectroscopy system. Spectroelectrochemistry experiments were carried out in a SEC-C thin layer quartz

glass spectroelectrochemical cell with 0.5 mm cell length from BASi. Pt mesh working electrode was homemade using platinum mesh and was anchored to a platinum wire. Teflon was used to wrap platinum wire beyond the platinum mesh to avoid further reactions during electrochemical experiment. All frequency, mass and resistance data were measured on a Model QCM 200 Quartz Crystal Microbalance Digital Controller from Stanford Research Systems, processed by a SRS LabVIEW program. The temperature of the electrochemical system of interest was controlled by a Fisher Scientific thermostat (Model No. 9101). 5 MHz AT-cut quartz crystals sputtered with polish Au were obtained from Maxtek, with a front electrode area of 1.37 cm^2.

All electrochemical measurements were performed in a three-neck glass cell with frit. A Ag/Ag^+ reference electrode and a Pt wire counter electrode were used unless otherwise specified. All potential references are made in reference to Ag/Ag^+ reference electrode, which is 0.50 V vs. NHE. Glassy carbon (GC) electrodes were homemade, in which GC slug was wrapped with Teflon casing. Prior to experiment, solutions were subjected to 10 minutes of degassing by Ar or N_2 to prevent undesirable side-reactions and oxygen reduction in the applied potential window.

The following procedure was taken to clean GC electrodes before use. Electrodes were sonicated in ethanol for 30 seconds before polishing with diamond paste and fluid. Following polishing, the electrodes were sonicated in ethanol again for 30 seconds and dried with IR lamp.

The following procedure was taken to clean Au QCM electrode before use. Any residual organic material was removed using a fine swab that does not scratch surfaces with acetone. The Au electrode was then cycled in 0.1 M $HClO_4$ between – 0.2 – 1.4 V vs. Ag/AgCl at 200 mVs^{-1} until a clean and stable Au profile is obtained.

Li half-cells were assembled in a CR 2032 coin cell, with a lithium foil and Celgard as anode and separator, respectively. Cathodes were prepared by mixing active material with super P and PVDF in a 3:6:1 ratio, and the resulting slurry was casted onto a carbon paper as current collector. Coin cells were tested on an Arbin battery tester.

Monomer Electrochemistry (CV)

The following monomers (as listed in Table 6-S1) were subjected to CV to examine their electrochemical properties. Conditions of respective experiments are specified in the following tables.

Table 6-S1. CV Parameters and Conditions of Monomers Tested

Species	[monomer]	Solvent/electrolyte	Potential window
TMPD	1 mM	0.1 M TBAP/MeCN	-0.5 – 0.6 V
BZ			-0.2 – 0.6 V
PT			0.0 – 0.7 V
PT-(TMPD)$_2$	0.5 mM	0.1 M TBAP/(1:1 MeCN/DCM)	-0.5 – 1.1 V
PT-Br$_2$	1 mM	0.1 M TBAP/MeCN	0.0 – 0.7 V
PT-(Ani)$_2$	1 mM	0.1 M TBAP/DCM	-0.5 – 1.4 V

Table 6-S2. CV Analysis of Monomers Tested

	E^o *(V vs. Ag/Ag$^+$)*	D_{ox} *(cm^{2}s^{-1} × 10^{-5})*
TMPD	-0.2	2.22
	0.35	5.33
BZ	0.12	4.04
	0.30	9.32
PT	0.43	1.92
PT-Br$_2$	0.50	2.22
PT-(TMPD)$_2$	-0.20	1.11
	0.05	1.85
	0.40	3.92
	0.55	5.75
	0.85	9.46
PT-(Ani)$_2$	-0.02	1.6
	0.25	3.52

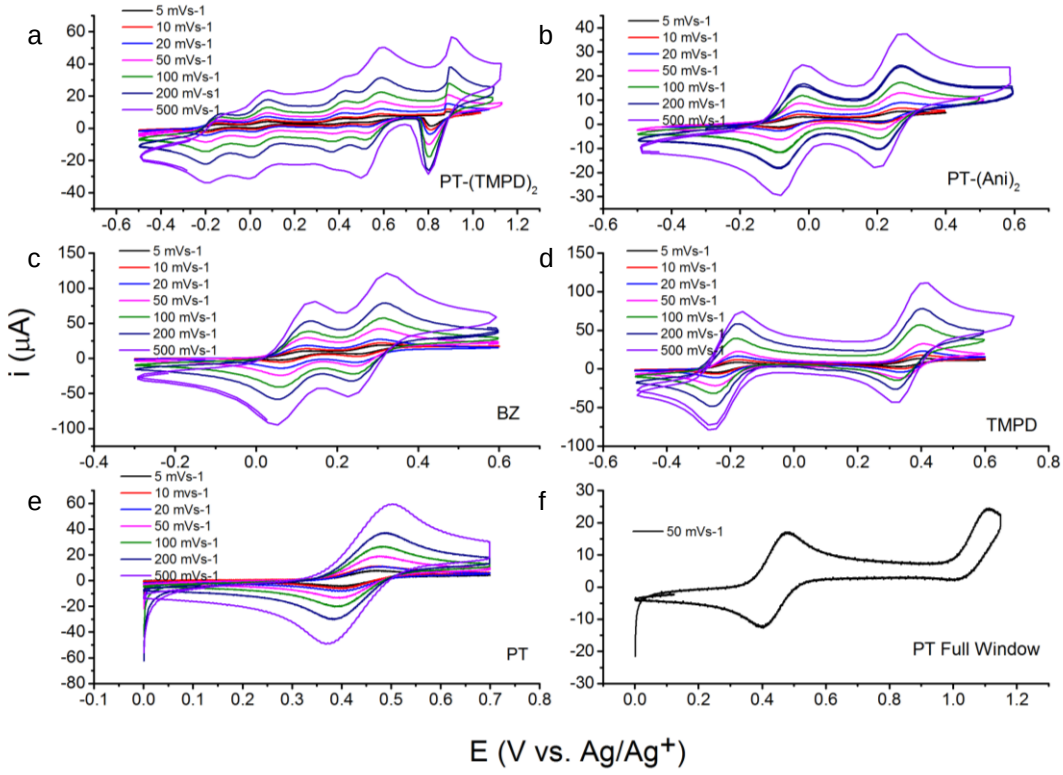

Figure 6-S1. Monomer scan of PT-$(TMPD)_2$ (a), PT-$(Ani)_2$ (b), BZ (c), TMPD (d), PT (e), and full window of PT (f). (a) was taken in 0.1 M TBAP in 1:1 MeCN/DCM with 0.5 mM of monomer. (b) – (f) used 1 mM of monomer and 0.1 M TBAP/MeCN as electrolyte solution and the respective scan rates are specified.

Slurry/Ink Preparation

2.0 mg of bulk polymer, 2.5 mg of carbon black and 0.5 mg of PVDF were mixed in a 5 mL vial with 1 mL NMP. Such composition gives a composite loading of 5 mg mL^{-1}. The mixture was sonicated for at least 1 hr until the mixture is homogenously dispersed in solvent, 10 μL of ink was dropcasted onto GC surface to create a polymer loading of 57 μg cm^{-2}.

Even though the powder polymers were insoluble in conventional organic solvents, when oxidized the polymers become highly soluble, as the slurry on GC dissolves as the materials became oxidized. As materials were lost during cycling, scan rate dependence and other quantitative analysis can not be obtained from CVs of slurries.

UV-Vis Spectroelectrochemistry

Blank spectrum was taken using 0.1 M TBAP/(1:1 MeCN/DCM). 0.5 mM PT-$(TMPD)_2$ in the same electrolyte solution was used to fill the spectroelectrochemistry cell. CV was taken at 10 mVs-1, and UV-vis spectra were taken every 10 s (1 spectrum per 100 mV).

The same procedure was used to record the spectroelectrochemistry of PT-$(Ani)_2$ coupled chemical reaction. 1 mM PT-$(Ani)_2$ in 0.1 M TBAP/MeCN was used as monomer solution, and CV was taken at 10 mVs-1 and UV-vis spectra were taken every 10 s (1 spectrum per 100 mV).

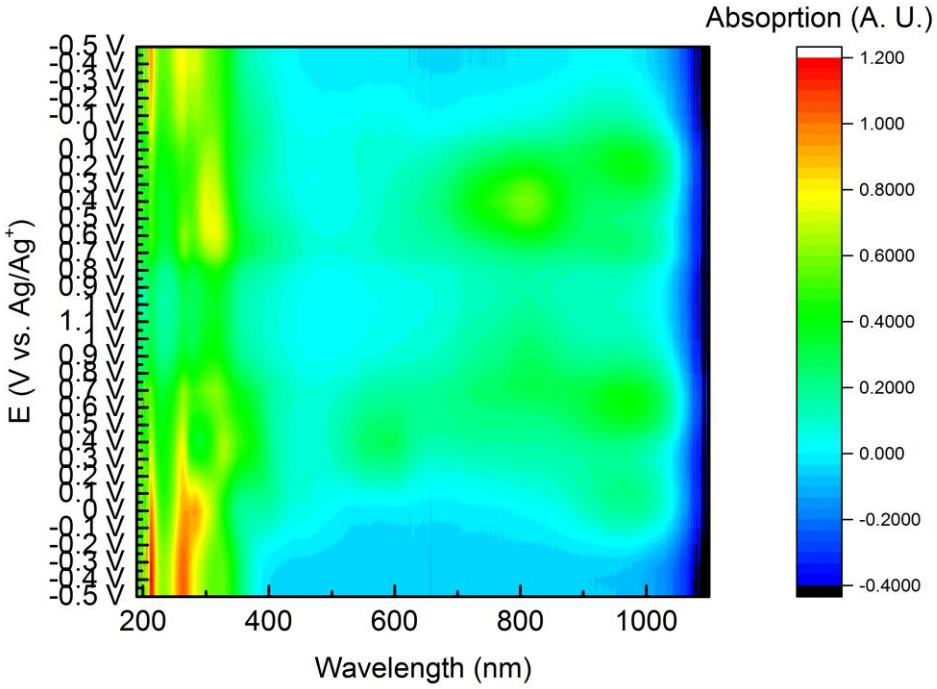

Figure 6-S2. UV-vis spectroelectrochemistry contour plot of PT-$(DMPD)_2$ at 0.5 mM in 0.1 M TBAP electrolyte solution in 1:1 MeCN/DCM.

Electropolymerization of PT-(Ani)$_2$

Electropolymerization of PT-(Ani)$_2$ on GC electrode was carried out in a three-neck glass cell. 10 mM monomer in 1 M TBAP/DCM was used as monomer solution; 1 M electrolyte concentration is required in order to minimize solution resistence as the monomer becomes triply charged using electropolymerization.

CV was the main method of electropolymerization, and there are two modes of electropolymerization. As shown in Fig. 4c, polymerization can be performed by cycling between the full window of electropolymerization, -0.5 – 1.4 V, for a desired number of polymerization cycles. Since a larger potential window is cycled, this method takes longer for the polymerization process to finish. On the other hand, for faster polymerization, as shown in Fig. 6a inset, we can speed up the polymerization process by only cycling the third redox couple, where polymerization occurs. As a result, the overall time of polymerization will be decreased, while the film quality remains the same as the essential mechanism of the polymerization process is retained.

Upon completion of electropolymerization, all thin-film samples were, first, rinsed with DCM and, then, acetone to wash away any residual monomer and mobile oligomers on the electrode surface. Subsequently, the clean thin-films were subjected to electrochemical characterization in blank electrolytes.

Electrochemical Quartz Crystal Microbalance

The electrochemical cell used during EQCM experiments are shown in Figure 6-S3. A custom-made one chamber electrochemical cell was used, with temperature control. A Teflon lid fitted to the chamber and electrodes and QCM sensors was employed to ensure air-free experimental condition.

The main objective for the use of EQCM in this manuscript is to confirm two quantities: mass of deposited film and the mass of ions that intercalate through such film. As a result, it is paramount that we determine these quantities with consistency and accuracy.

System stabilization was achieved with a one-chamber temperature control glass cell; a stir bar was equipped to maintain the homogeneity of the solution. O-rings in contact with monomer solution was made of Kalrez, which is highly resistant to swelling to organic solvents. Pre-polymerization stabilization is usually established within two hours of waiting period.

Electropolymerization in QCM starts with a two-cycle stabilization cycle, where potential is swept between -0.5 – 0.5 V, accessing the first two redox couples in the monomer. While significant current is observed for these stabilization cycles, we observed minimal but regular variation in mass and frequency, due to slight capacitive behaviors as monomers becomes oxidized and reduced. Upon establishment of such dynamic stabilization, electropolymerization was carried to the third redox couple between 0.70 – 1.15 V. As Au is used and results obtained from blank electrolyte solution in electropolymerization condition, potential more positive than 1.15 V cannot be accessed during electropolymerization. By only cycling at the third redox couple, mass increase and frequency decrease dramatically as the number of polymerization increases. For twenty cycles of electropolymerization, the increase of mass approaches linear relationship with cycle number; for more than twenty cycles of electropolymerization, mass increase starts to slowly down after twentieth cycle, due to significant deposition on electrode.

Upon completion of electropolymerization, thin-film sample were cleaned as described in previous section; thin-film sample is rinsed with DCM then acetone until

a visibly clean and smooth film is obtained. Subsequently, the film is subjected to cycling in 0.1 M TBAP/MeCN. Stabilization pre-cycling was performed as described for the electropolymerization using QCM until a stable frequency is observed for the system. During cycling, polymer film was cycled between -0.5 – 0.75 V, as more positive potential leads to overoxidation of the thin-film on Au substrate, and mass and frequency changes were recorded.

Resistance was recorded along with mass and frequency as EQCM experiments were performed. In no cases, did we observe resistance change larger than ten ohms over the course of all experiments, indicating that the deposition of thin-film and that the resulting film behave as rigid films without significant viscoelastic changes during these processes. This observation allows for the direct application of the Sauerbrey equation correlating frequency changes to mass changes.

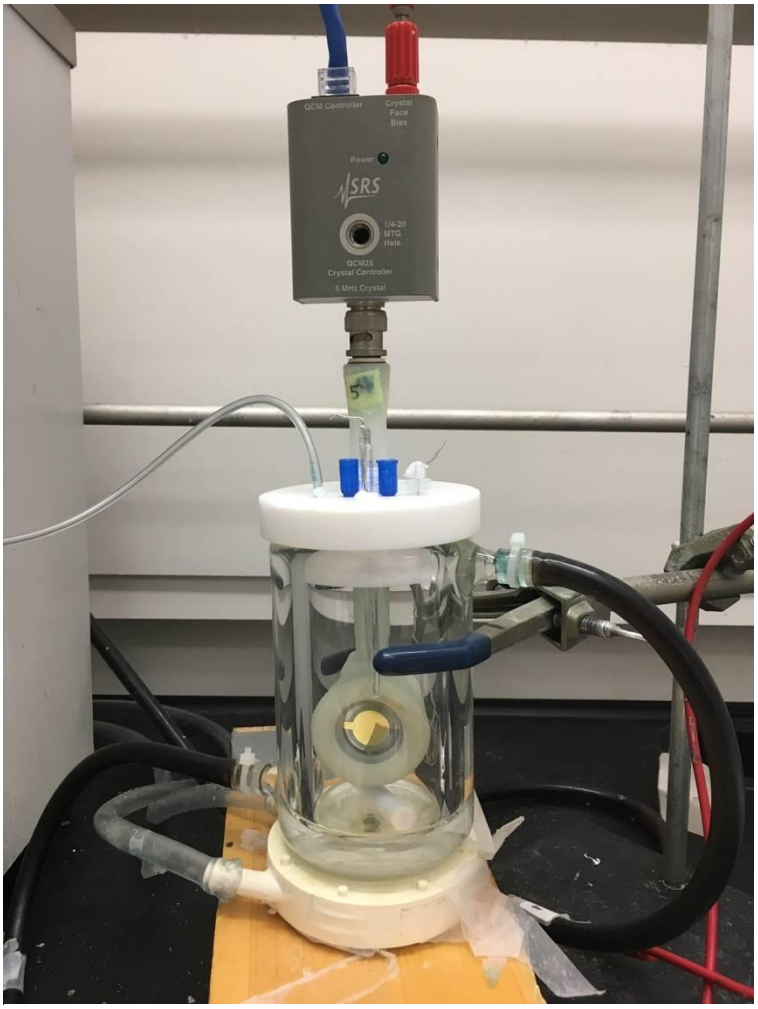

Figure 6-S3. EQCM setup for electropolymerization and film cycling of thin-film PT-BZ.

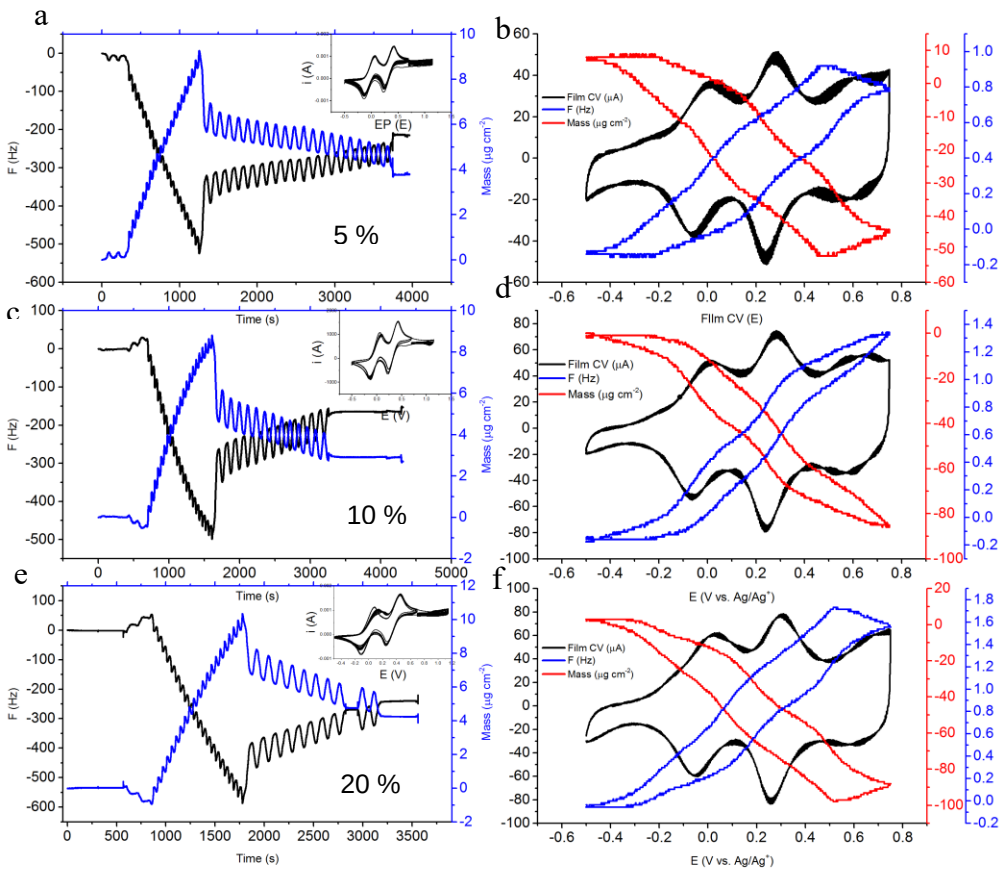

Figure 6-S4: Electropolymerization and the resulting film cycling CV and QCM traces with 5 (a, b), 10 (c, d) and 20 % (e, f) cross-linker. For 10 and 20 % cross-linker experiments, drift in frequency is observed during electropolymerization, possibly due to the adsorption of small oligomers adsorbing to Au from 2nd and 3rd-time used monomer solution. Despite drift, stabilization of system is established before and after electropolymerization, as shown in c and e before and after CV cycling started. Mass difference was taken between the stabilized frequencies in those trials.

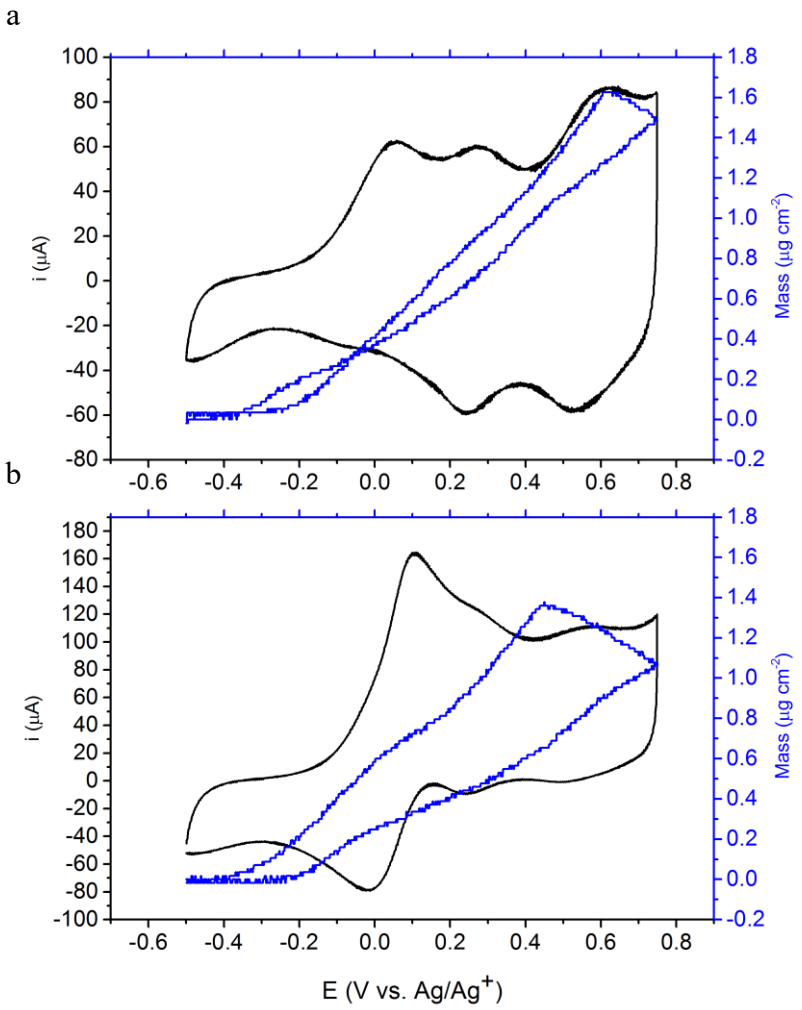

Figure 6-S5. Cycling of thin-film PT-BZ without (a) and with (b) 1 mM of Ferrocene (Fc) as a redox shuttle to unclog potentially unaccessible film. The CV trace in b shows very different behavior as that in a, as the response of Fc is confounding the response from the thin-film PT-BZ. However, as we can see, the QCM traces in a and b do not differ significantly, especially in terms of magnitude (mass change). With Fc in solution, it appears the film expel some species towards the end of oxidation (decrease in mass between 0.4 – 0.75 V), and this could be due to the incorporation of Fc during oxidation at lower potentials, and as the film becomes more oxidized, they are expelled to accommodate the charge neutrality within the film.

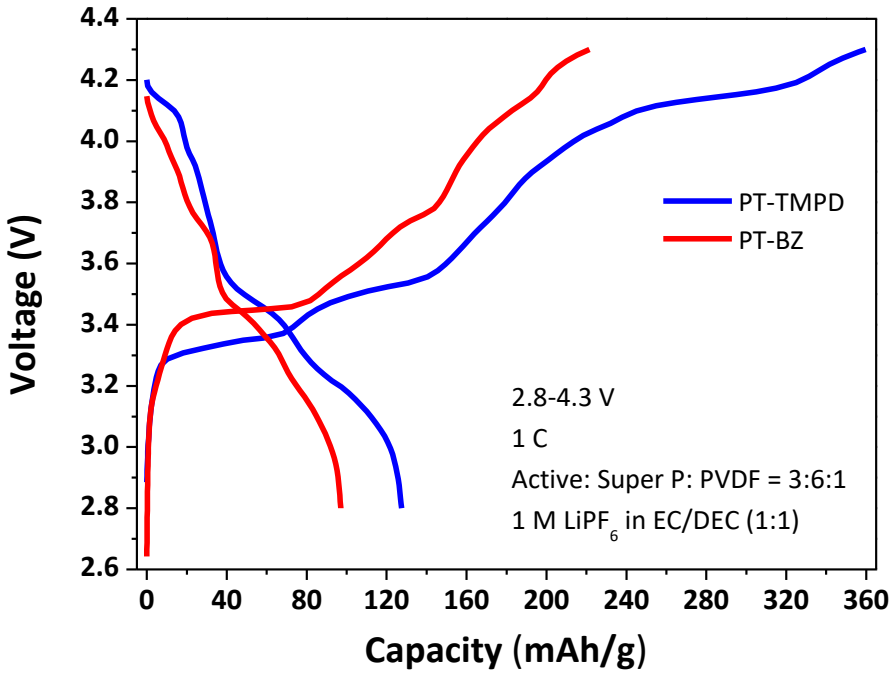

Figure 6-S6. Li half-cell of PT-TMPD and PT-BZ as cathodes testing practical capacities of the materials. The coin cells were cycled at 1 C from 2.8 – 4.3 V vs. Li/Li^+ in 1 M $LiPF_6$ EC/DEC (1:1). Active material loading in both cases are 30 %, with 60 % super P as conducting additive and 10 % PVDF as binder.

CHAPTER 7

SUPERIOR ENERGY AND POWER DENSITY OF A COVALENT ORGANIC FRAMEWORK CONDUCTING POLYMER HYBRID[xi]

7-1. Introduction

As the demand for high performing materials increases, new materials with various structures, forms, and/or properties are constantly being invented and studied.[1] One of the fastest growing fields in materials design and implementation is the realization of two-dimensional (2D) macromolecules. These materials exhibit interconnected networks of repeating functional moieties that can perform specific functions and their attributes largely propelled the advancement of this class of materials. In their structures, 2D macromolecules can exhibit an ordered pattern on a surface and this ordered layer can give rise to stacking, forming another ordered (3rd) dimension.[2] This type of structural arrangement largely resembles the structure of a crystal, rendering the 2D macromolecules crystallinity that is detectable by X-ray powder diffraction (XRD). On the other hand, it can provides the network with porosity, rendering them as molecular hosts.[3] Because of their unique structural and chemical properties, 2D macromolecules have been applied to areas that take advantage of these properties, such as gas molecule storage by their mesoporous structure, energy storage by their interconnected repeating network, and have shown great promise in both fields of application.[4]

A 2D macromolecule, where metal ions are involved, is generally called a metal organic framework (MOF) and one without any metal ions is called a covalent

[xi] This chapter is reproduced in part with permission from *ACS Cent. Sci.* **2016**, *2*,

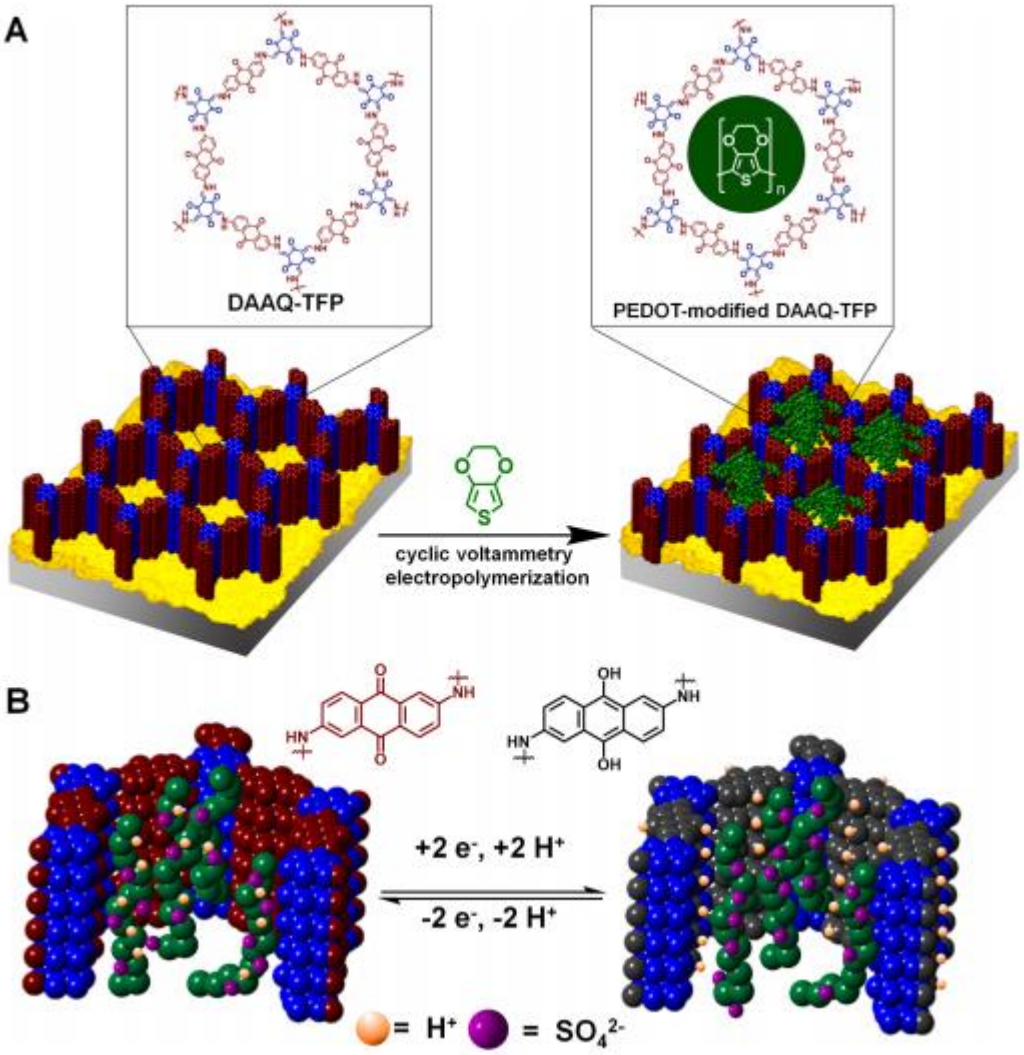

Figure 7-1. Incorporation of PEDOT within a DAAQ-TFP COF film. (A) Depiction of modification of DAAQ−TFP films by electropolymerization of 3,4-ethylenedioxythiophene (EDOT). Schematic depicts what may occur within one COF crystallite. (B) Schematic of the cross-section of a pore following the oxidation and reduction of the DAAQ moieties

---

667-673.

organic framework (COF). An attractive way to envision COF and MOF as energy storage materials is by incorporating redox-active units into their macromolecular network, and that each repeating unit will be composed of redox-active groups. As a result, a redox-active MOF or COF will be a 3D crystalline material with compact redox-active units embedded in the network, stacked together layer by layer in an orderly fashion.[1-4] In addition, from an electrochemical energy storage (EES) design standpoint, an ideal electrode material should be lightweight in order to maximize energy density, and naturally, COFs have an advantage over MOFs in this respect. Moreover, the crystallinity inherent to COFs also provides it with chemical stability no less than that observed for MOFs and, for those reasons, COF materials have attractive properties to be promising materials for electrochemical energy storage (EES) applications.

As they were briefly discussed in Chapter 1 as a redox-active moiety, anthroquinones are highly desirable for their stable redox chemistry and performance. Anthroquinones have shown high capacity retention with thousands of cycles in battery testing and therefore represents a molecule of choice when a proof-of-concept experiment or device is called for. By improving on the boronate ester-linkages employed in some of the early COF literature, 2,6-diaminoanthraquinone (DAAQ) was successfully incorporated into a 3D COF by *β*-ketoenamine linkages, rendering the DAAQ-triformylphloroglucinol (TFP) hydrolytically and oxidatively stable during electrochemical testing conditions. [5] As a result, the DAAQ-TFP COF showed promising two electron redox behaviors from the anthraquinone unit in sulfuric acid solution with high cycling stability (5000 cycles)[5], making it a highly promising EES

material.

However, it was also well-known that 3D COFs and MOFs are generally electronically insulating in nature, especially in the direction perpendicular to the 2D the layers of the materials.[6, 7] As a result, in the case of DAAQ-TFP, it was found that, thin-films of DAAQ-TFP could exhibit significant the redox propagation rates[6], up to film thicknesses of about 200 nm, before redox accessibility started to dramatically fade below 50 % of all redox-active units. With most films in realistic devices requiring in thicknesses of microns or even hundreds of microns, the insulating nature of COFs represented a clear impediment to the practical use of chemically robust DAAQ-TFP as a promising material for EES.

One of the most direct and efficient ways to enhance electronic conductivity was to incorporate a conducting polymer into the network. The use of conducting polymers represents a promising method for relaying electrons and improving electronic conductivities in many types of electrode materials. For example, polyaniline[8], polypyrrole and PEDOT[9] have been used to make conformal surface coatings onto sulfur particles to increase electronic conductivity while mitigating polysulfide dissolution during the charge-discharge process. Using conducting polymers in a similar fashion, we were optimistic that they would be able to boost the electronic conductivity and redox accessibility of the redox-active COF, DAAQ-TFP, at more realistic film thickness, and to enhance the usability of DAAQ-TFP for device testing.

7-2. Results and Discussions

The conducting polymer poly(3,4-ethylenedioxythiophene) (PEDOT) was

chosen as the conducting additive for its chemical stability in a wide range of solvent conditions and for its high conductivity which would, in turn, improve the electronic conductivity of DAAQ-TFP COFs (Figure 7-1). Previous studies have shown that PEDOT, as a conducting polymer, exhibits high conductivities in both aqueous media at various pH values[10-13] as well as organic solvents[14, 15]. This broad compatibility and robustness is highly desirable for DAAQ-TFP COFs, as it would make anthraquinone moieties to be accessed over a broad range of conditions. In addition, the versatility of synthetic methods [16-18] to polymerize EDOT allowed various types of DAAQ-TFP samples to be modified and analyzed.

According to a previous report, DAAQ-TFP COF was prepared by the slow deposition of the COF onto a Au substrate, and various film thickness were achieved by employing different DAAQ concentrations. The composition of the resulting film on Au was characterized by Fourier transform infrared (FT-IR), X-ray photoelectron spectroscopy (XPS), scanning electron microscopy (SEM) and grazing incidence X-ray diffraction (GIXD). All characterizations confirmed that the films of various thickness used in this report were chemically consistent with the thin films used in previous reports (all characterizations are included in original manuscript).

One of the most intriguing question regarding the PEDOT-modified DAAQ-TFP is: where does the PEDOT reside in the ordered network of DAAQ-TFP? When we electropolymerize PEDOT onto a DAAQ-TFP sample using cyclic voltammetry (CV), the expectation is to have PEDOT growing throughout the pores of the COF

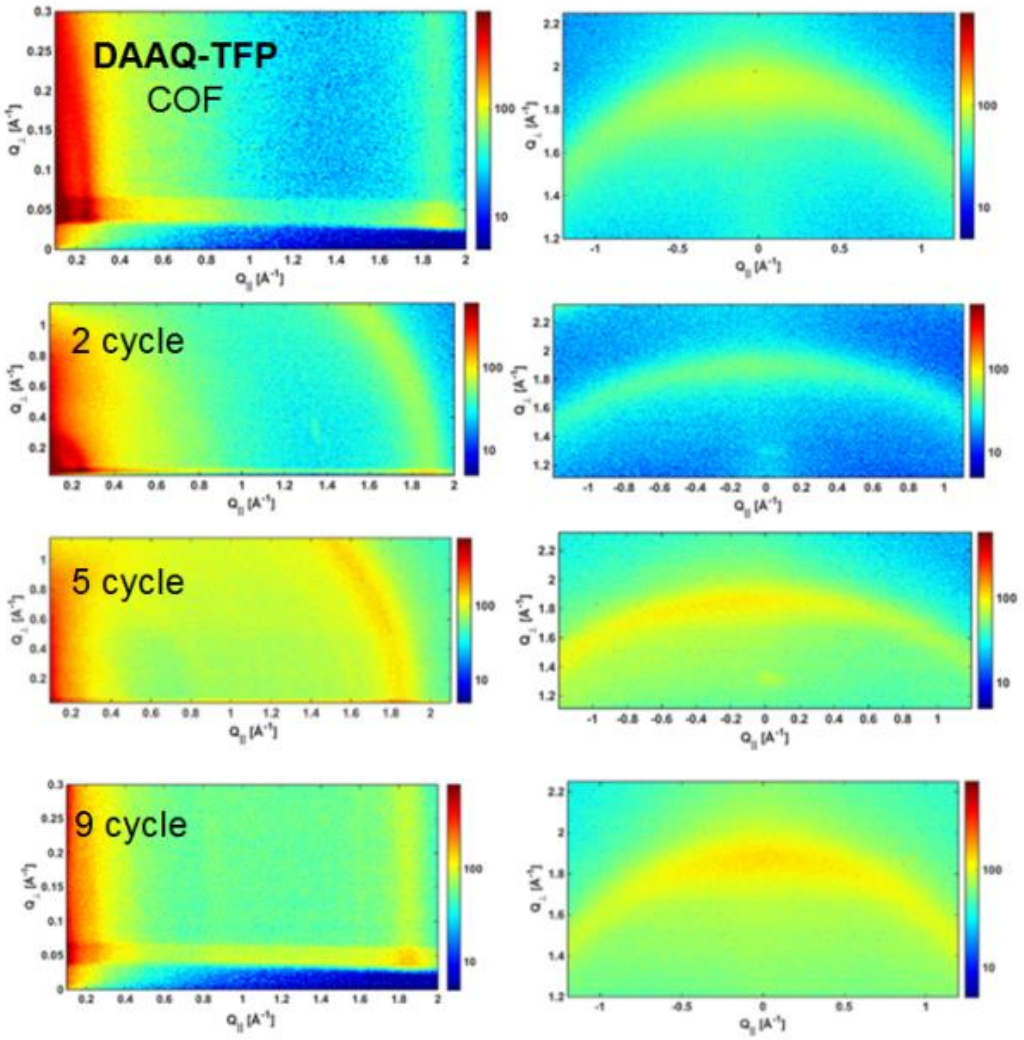

Figure 7-2. Representative GIXD of DAAQ-TFP films on Au substrates. The top row corresponds to a DAAQ-TFP COF film prior to electropolymerization. Subsequent rows correspond to 2, 5, and 9 electropolymerization cycles, respectively.

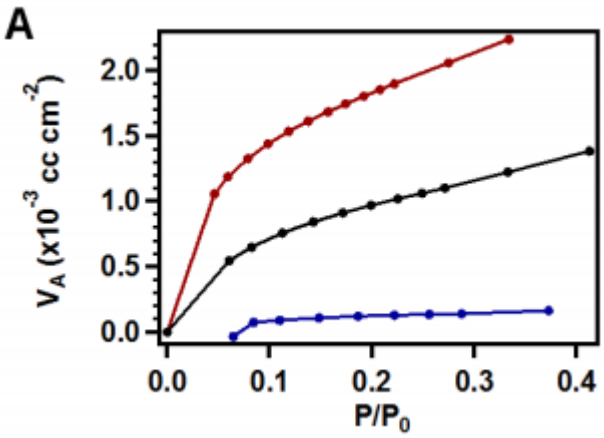

Figure 7-3. Kr gas adsorption isotherm for DAAQ-TFP COF without PEDOT (red), 2 cycle polymerization PEDOT / DAAQ-TFP COF (black), and 9 cycle polymerization PEDOT / DAAQTFP COF (blue).

network as the monomer EDOT has to make contact with the Au substrate in order to electropolymerize. This would suggest that PEDOT grows from inside the pores of the COF towards the outside. Both GIXD experiments and Kr adsorption experiments are in accordance with this hypothesis (Figure 7-2 and Figure 7-3). The crystallinity of DAAQ-TFP gradually disappeared with increasing PEDOT electropolymerization, indicating that the more deposition of amorphous PEDOT through DAAQ-TFP, the less crystallinity of COF can be observed, suggesting the growth of PEDOT starts from inside the pores. A similar trend was observed when the surface area of DAAQ-TFP decreases from 73 to 40, then to 6 cm^2 cm^{-2} as the amount of PEDOT deposited ranges from none, two cycles to nine cycles of electropolymerization. Both sets of experiments suggest that the electropolymerization of EDOT starts from the Au substrate, at the base of the COF pores, and grows outwards throughout the interconnected COF network.

Based on the data and interpretation suggesting that PEDOT electronically wires the redox-active units in the DAAQ-TFP COF by filling the pores in the network, we can reasonably expect a significant boost in the accessibility of redox-active moieties in DAAQ-TFP films thicker than 200 nm. Figure 7-4 compares the accessibility of redox moieties in DAAQ-TFP before and after PEDOT modification for a 1 μm thick film. For an unmodified DAAQ-TFP film, only about 3 % (0.230 mC) of the available anthraquinones are accessed at 20 mVs^{-1} in 0.5 M H_2SO_4, while, after nine cycles of electropolymerization of PEDOT, 9.3 mC of charge were accessed, corresponding to a 40-fold increase in accessibility of the redox moieties. The same dramatic improvement in conductivity was also observed when scanning at

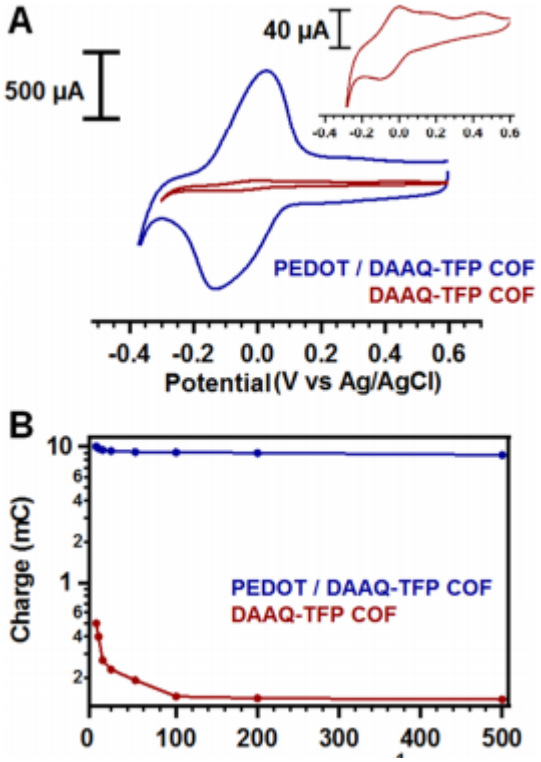

Figure 7-4. Electrochemical performance of a PEDOT-modified and assynthesized DAAQ−TFP COF film. (A) CV response at 20 mV s−1 in 0.5 M H2SO4 of a PEDOT-modified DAAQ−TFP film, 1 µm-thick (blue), and the same as-synthesized DAAQ−TFP film before EDOT polymerization (red). The inset presents the cyclic voltammetric response for the unmodified film using an expanded current scale. (B) The integrated charge associated with the oxidative wave of a PEDOTmodified DAAQ−TFP COF film (blue) and unmodified DAAQ−TFP COF film (red) recorded over various scan rates indicate that the PEDOT-modified films store more charge and tolerate faster scan rates than the unmodified films.

various scan rates. While unmodified DAAQ-TFP film accessed charges less than 5 mC from 5-500 mVs^{-1}, PEDOT-modified DAAQ-TFP maintained high accessibility at all scan rates at about 10 mC. These observations clearly outlined the drastic improvement of electronic conductivity within the DAAQ-TFP network via PEDOT wiring, largely improving the practical usability of COF as electrode material.

To highlight the dramatically improved electronic conductivity of the DAAQ-TFP COF, galvanostatic measurements were carried out. In a three-electrode setting (Figure 7-5), from 10 to 1000 C, unmodified DAAQ-TFP shows only 20 F cm^{-3} at 10 C, and it continues to decrease further at higher C-rates. On the other hand, the PEDOT-modified DAAQ-TFP, exhibits much higher accessibility by retaining more than 80 % of its capacitance from 10 to 100 C, and still retaining 50 % at ultra-high C-rates of 1600 C (2.25 s). The PEDOT-modified DAAQ-TFP also showed impressive stability over 10,000 cycles at 100 C with no distinct degradation or capacity fade within the duration of the test.

In order to further highlight the practicability of PEDOT-modified DAAQ-TFP, two-electrode setup and a proof-of-concept light emitting diode device was used. As larger amount of samples are required to perform such tests, PEDOT was modified onto DAAQ-TFP using a co-precipitation method by chemically polymerizing EDOT in a suspension of DAAQ-TFP polycrystalline powder. Characterizations of capacitor device (Figure 7-5) shows that the resulting composite has the same properties as the thin-film form of PEDOT-modified DAAQ-TFP. Both two-electrode setup and proof-of-concept device were assembled as a capacitor in a coin cell to hold all components in place (Figure 7-5). To avoid corrosion of current collector, a Ti foil was used as

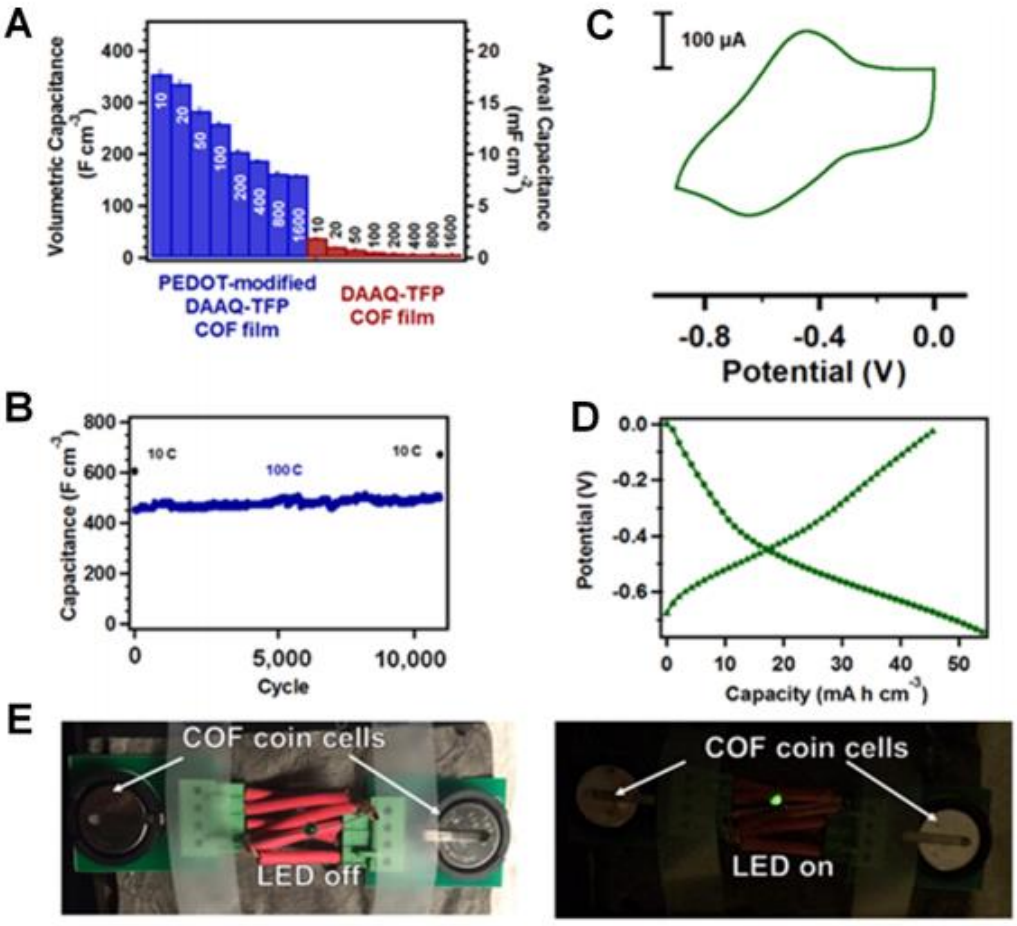

Figure 7-5. Charge storage performance and device integration of a PEDOT-modified DAAQ−TFP film. (A) Average capacitances calculated from 10 cycles of galvanostatic charge−discharge experiments at various C rates (error bars show ±1 standard deviation). (B) Extended cycling of a PEDOT-modified DAAQ−TFP film showing stability over 10 000 cycles. First three cycles are at a rate of 10 C, then over 10 000 cycles at a rate of 100 C, followed by another three cycles at 10 C showing no loss in capacitance over the cycles. (C) CV in a two-electrode device configuration, in which the counter is a highsurface area carbon electrode. (D) A potential/capacity plot obtained in a two-electrode experiment exhibits well-defined voltage plateaus at the formal potential of the DAAQ moieties. (E) A PEDOT-modified DAAQ−TFP COF working device powering a green LED.

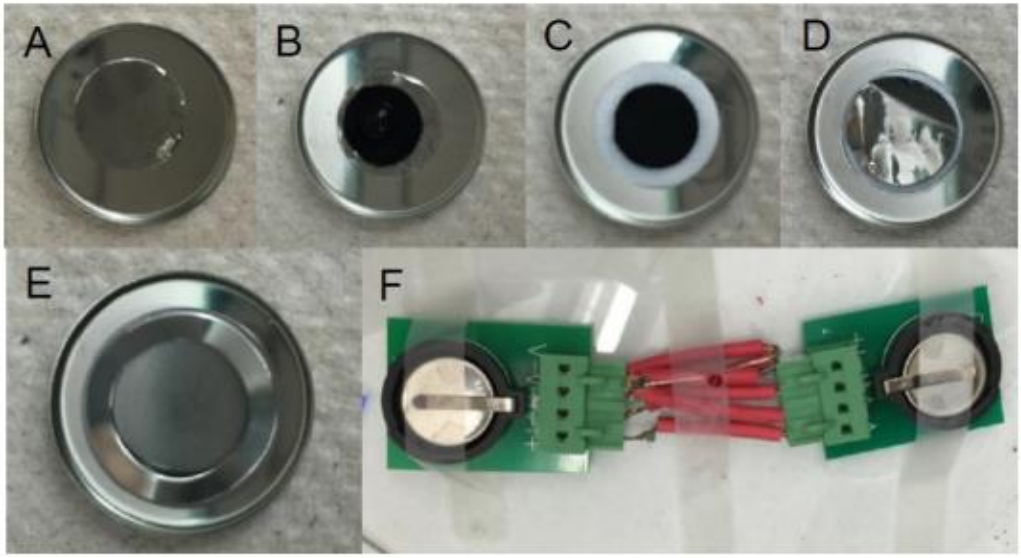

G

Component	Ti current collector	PEDOT / DAAQ-TFP COF (1:1)	Anode	Separator
Diameter (in)	7/16	5/16	5/16	1/2

Figure 7-6. Assembly of a cell. Starting from the cathode, (A) Ti current collector, (B) PEDOT / DAAQ-TFP COF, (C) separator and activated carbon, (D) Ti current collector, (E) stainless steel piece and spring, and (F) shows two cell connected in series using Arbin channels connected by wires with the LED attached to the setup.(G) Specification of cell components.

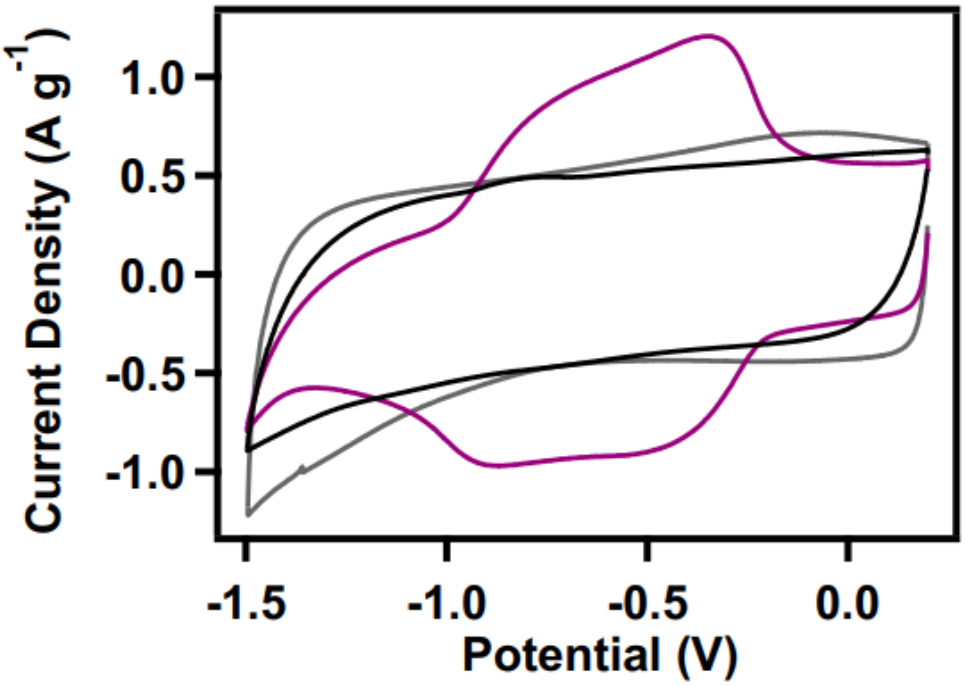

Figure 7-7. CV response for a coin cell fabricated from PEDOT-modified DAAQ-TFP COF powder where the PEDOT to COF mass ratio is 1:1 (purple) and similarly fabricated coin cells with only activated carbon (grey) or with PEDOT only as the active material (black). The mass used in the normalization is the combined active electrode and counter electrode mass.

current collector for the cathode and glass fiber paper was used as the proton-permeable membrane. Dimensions of all electrode components were shown in Figure 7-6G for reference, and the device was assembled under ambient conditions.

Characterization of the bulk PEDOT-modified DAAQ-TFP composite was carried out with the same methods for the thin-film PEDOT-modified DAAQ-TFP. In Figure 7-7, the voltage window was shifted from ± 0.5 V vs. Ag/Ag^+ to – 0.9 – 0.0 V and this was due to the use of a carbon counter/reference electrode in the two-electrode setup. In addition, due to the much thicker film and less facile ion diffusion, a wider peak-to-peak separation is observed in CV with cycled while a well-defined redox couple at ca. -0.5 V suggests the redox property of the thin-film PEDOT-modified DAAQ-TFP was retained in the powder form. Thicker electrodes also impeded the rate performance of the device as shown in Figure 7-6 that the spread of capacitance is wider for a two-electrode system than the three-electrode system. To illustrate the practical applicability of PEDOT-modified DAAQ-TFP, 1:1 PEDOT/COF composite was synthesized and assembled into capacitor devices. By serially connecting two of such cells, discharge of the serial device successfully powered the illumination of a green LED for 30 s (Figure 7-5E).

7-3. Conclusions

Prior to this study, COF materials had only shown promise for EES in thin-film forms (~50 nm) due to low electronic conductivity. Conducting polymer wiring using PEDOT in DAAQ-TFP showed that by filling the pores of COF with conducting polymer, the redox-active moieties in the DAAQ-TFP network were electronically

connected and showed quantitative accessibility for films thicker than 1 μm even at high scan (C) rates. This quantitative accessibility of redox-active moieties in DAAQ-TFP yielded greatly improved capacity retention over the range of 10 – 1600 C when compared to unmodified DAAQ-TFP at the same thickness. By assembling two-electrode cells and capacitor modeling device, we successfully use COF materials to power the illumination of LED device demonstrating that these materials can be used in practical, real-life EES device.

REFERENCES

1. Feng, X.; Ding, X.; Jiang, D. *Chemical Society Reviews* **2012,** *41* (18), 6010-6022.

2. Ding, S.-Y.; Wang, W. *Chemical Society Reviews* **2013,** *42* (2), 548-568.

3. Colson, J. W.; Dichtel, W. R. *Nature Chemistry* **2013,** *5*, 453.

4. Côté, A. P.; Benin, A. I.; Ockwig, N. W.; Keeffe, M.; Matzger, A. J.; Yaghi, O. M. *Science* **2005,** *310* (5751), 1166.

5. DeBlase, C. R.; Silberstein, K. E.; Truong, T.-T.; Abruña, H. D.; Dichtel, W. R.. *Journal of the American Chemical Society* **2013,** *135* (45), 16821-16824.

6. DeBlase, C. R.; Hernández-Burgos, K.; Silberstein, K. E.; Rodríguez-Calero, G. G.; Bisbey, R. P.; Abruña, H. D.; Dichtel, W. R. *ACS Nano* **2015,** *9* (3), 3178-3183.

7. Xu, F.; Jin, S.; Zhong, H.; Wu, D.; Yang, X.; Chen, X.; Wei, H.; Fu, R.; Jiang, D. *Scientific Reports* **2015,** *5*, 8225.

8. Zhou, W.; Yu, Y.; Chen, H.; DiSalvo, F. J.; Abruña, H. D. *Journal of the American Chemical Society* **2013,** *135* (44), 16736-16743.

9. Li, W.; Zhang, Q.; Zheng, G.; Seh, Z. W.; Yao, H.; Cui, Y. *Nano Letters* **2013,** *13* (11), 5534-5540.

10. Kong, F.; Liu, C.; Song, H.; Xu, J.; Huang, Y.; Zhu, H.; Wang, J. *Synthetic Metals* **2013,** *185-186*, 31-37.

11. Bobacka, J.; Lewenstam, A.; Ivaska, A. *Journal of Electroanalytical Chemistry* **2000,** *489* (1), 17-27.

12. Tamburri, E.; Orlanducci, S.; Toschi, F.; Terranova, M. L.; Passeri, D. *Synthetic Metals* **2009,** *159* (5), 406-414.

13. Du, X.; Wang, Z. *Electrochimica Acta* **2003,** *48* (12), 1713-1717.

14. Kim, Y. H.; Sachse, C.; Machala, M. L.; May, C.; Müller-Meskamp, L.; Leo, K. *Advanced Functional Materials* **2011,** *21* (6), 1076-1081.

15. Kim, J. Y.; Jung, J. H.; Lee, D. E.; Joo, J. *Synthetic Metals* **2002,** *126* (2), 311-316.

16. Selvaganesh, S. V.; Mathiyarasu, J.; Phani, K. L. N.; Yegnaraman, V. *Nanoscale Research Letters* **2007,** *2* (11), 546.

17. Zhang, X.; Lee, J.-S.; Lee, G. S.; Cha, D.-K.; Kim, M. J.; Yang, D. J.; Manohar, S. K. *Macromolecules* **2006,** *39* (2), 470-472.

18. Damlin, P.; Kvarnström, C.; Ivaska, A. *Journal of Electroanalytical Chemistry* **2004,** *570* (1), 113-122.

SUPPORTING INFORMATION

Materials and Instrumentation. All reagents were purchased from commercial sources and used without further purification. N,N-dimethylformamide was purchased from Sigma Aldrich and purified using a custom-built alumina column-based solvent purification system. All electrochemical measurements were performed in a three-neck glass cell with frit. A Ag/AgCl reference electrode (for organic systems) or a Ag/Ag^+ (for aqueous systems) and a Pt wire counter electrode were used unless otherwise specified. All potential references are made in reference to Ag/Ag^+ reference electrode, which is 0.50 V vs. NHE. Glassy carbon (GC) electrodes were homemade, in which GC slug was wrapped with Teflon casing. Prior to experiment, solutions were subjected to 10 minutes of degassing by Ar or N_2 to prevent undesirable side-reactions and oxygen reduction in the applied potential window.

Device Preparation/Assembly

PEDOT modified DAAQ-TFP COF powder for coin cell preparation The 10:1 and 1:1 PEDOT/COF composites were synthesized via chemical oxidation of EDOT in the presence of DAAQ-TFP COF powder. A 43 mg portion of EDOT was added into a mixture COF powder (30 mg) in methanol (MeOH) at 0 °C. After 15 minutes of mixing, $Fe(ClO_4)_3$ (0.214 g) was dissolved in MeOH and slowly added to the mixture of COF and EDOT. After stirring for 6 hours, dark blue powder was obtained. The polymer was extensively washed using MeOH to remove traces of $Fe(ClO_4)_3$ and dried at 90 °C overnight. Coin-shaped electrodes of both cathode (PEDOT/COF) and anode (activated carbon, AC) were prepared by adding 90 mg of material (for cathode, 80 mg of PEDOT/COF + 10 mg Super P carbon, for anode 90 mg of activated carbon) to a scintilation vial that is equipped with a stir bar and 10 mg of polytetrafluoroethylene (PTFE) as a binder. Less than 1 mL of ethanol was added and the mixture was allowed to vigorously mix at 60 °C until the mixture is almost dry.

The gels were rolled into a thin film and was allowed to dry at 60 °C overnight. Cell Assembly and Working A lithium-ion battery CR2032 cell was used as the device chamber, and was assembled, by stacking a Ti-foil, PEDOT/COF (cathode), separator, activated carbon, Ti-foil, stainless steel, spring and a cap. CV characterization of single coin cell device was tested by contact using Cu tape. After individual cells were confirmed to be working, two cells were connected in series using Arbin channels connect by wires. In order to charge a 2.2 V LED, the setup was charged to 2.2 V for 10 s, then was allowed to relax until the LED dimmed completely (about 30 s).

CHAPTER 8

FUTURE DIRECTION OF ORGANIC ELECTRODES FOR EES APPLICATION

8-1. Novel Oxidative Redox-Active Pendant

In this dissertation, I have investigated numerous oxidative redox-active moieties for EES applications. From these studies, I explored new molecular architectures for specific molecular designs, and "revived" redox-active moieties that were gems buried under the rubble. As an electrochemist that centers on materials design and testing, the discovery of a new class of promising materials can provide an opportunity for a whole series of investigations on the details of their design, synthesis, characterization and the subsequent device performance. Variations in their performance will lead to mechanistic studies and insights, looking deeply into the reasons behind the success or failure of these new materials. From an academic standpoint, we have ample motivation to keep innovating and designing new materials for EES applications.

For example, we studied in detail phenothiazine-derivatized polymers, which have been received increasing attention as EES cathode materials. Indeed, based on their redox behaviors, they showed great promise as a high-energy cathode in characterization as well as device performance. To continue exploring related materials, our attention can be shifted to structurally similar phenazine-derivatives[1-3] and phenoxazine-derivatives[4-6] (Figure 8-1). These two molecules include two molecular substitution at the S site in phenothiazine, and can show quite different redox activity. From an electrochemistry and synthetic standpoint, phenazine and phenoxazine can be used quite differently. Phenoxazine and phenothiazine are similar

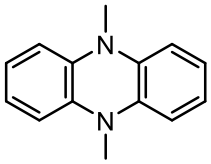

5,10-dimethyl-5,10-dihydrophenazine

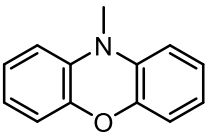

10-methyl-10*H*-phenoxazine

Figure 8-7. Phenazine and phenoxazine redox-active units.

structurally, therefore, dibromo-phenoxazine at the 2, 7-position should be easily synthesized as a coupling partner to carry out coupling reactions with an amine. On the other hand, phenazine can act as an amine partner synthetically, as dibromo-phenazine can be proven to be difficult to synthesize. In addition to coupling these three redox-active moieties with the respective coupling partners, they could potentially be coupled to each other, forming a new class of redox-active main-chain polymers.

8-2. Redox-Active Covalent-Organic Framework

I was able to install redox-active moieties into polymer architectures, both in thin-film and in bulk polymers forms. There are other forms of molecular architectures that are of potential interest. In the past, we have enjoyed success with incorporating redox-active moieties into covalent-organic framework (COF) materials (Chapter 7) as capacitor materials.

However, the characteristics of COF was yet to be fully explored. To fully explore COF's potential as EES electrode material, capacity needs to be elevated [refs] while retaining the full accessibility to redox-active moieties with the aid of conducting additives or molecular "wiring". The chemical stability of COFs should make them superior in the most common problem confronted by organic electrodes: dissolution. Exploiting the chemical stability of COF materials, we should explore their practical applicability in lithium-ion battery as cathode materials by incorporating oxidative redox-active moieties into the network. By exhibiting cyrstallinity within its macromolecular network, COF materials should exhibit

superior electrochemical stability as electrode materials in device level testing compare to current polymeric materials.

8-3. Polymer Dissolution

As discussed in the last section, dissolution is one of the most common problems experienced by organic electrode materials. Generally described by a chemical saying “like dissolves like”, organic electrodes naturally are more likely to dissolve in organic systems, which are the solvent systems generally used in lithium-ion batteries, than aqueous systems. Furthermore, this problem could arise at different stages of discharge since they can dissolve as neutral and/or at charged species. As one of the biggest problems precluding the practical applications of organic electrodes, it is a problem that desperately needs attention and solution (no pun intended).

As a potential strategy, we can borrow literature and experience from sulfur electrode protection in Li-S batteries.[7-9] During charge and discharge, polysulfides in Li-S battery can be highly soluble in the electrolyte system, and numerous methods and materials have been employed to mitigate this problem to improve cyclability and stability. Various host materials have been studied, and carbon-based materials are the most common for its cost and potential high-surface application. Mesoporous carbon materials can adsorb the soluble polysulfide into their nm-scale pores and as a result, trapping these soluble species from dissolving into the electrolyte. Another types of materials include using coating sulfur particles with another materials to form a physical barrier to confine the sulfur.

For organic materials, we could employ carbon-based mesoporous host as well to attempt to decrease dissolution. For example, CMK-3 carbon has been used previously as a part of the conducting additives in small molecule electrodes and showed dramatic improvement in cyclability when compare to composite without CMK-3 carbon.[10, 11] In practice, this subsitution is usually done by substituting a

portion of the carbon black with mesoporous carbon during electrode fabrication. By using these carbon-based trapping materials, it is very likely that they will be able to adsorb the small soluble oligomers dissolving from current collector during device cycling, hence, improving cycling stability of future organic electrode materials at a practical level.

Another strategy would require more chemical intuition. We could exploit the specific interactions between different atoms/functional groups to improve cyclability. Using the phenothiazine polymers as an example, the S in the molecule is a "handle" for such interaction, and we can envision using NiO or Fe_2O_3 as host materials to attempt to minimize dissolution. Ni^{II} and Fe^{III} should be very good metal centers to coordinate to S/S^- and the bond is formed very favourably. Using this type of specific interaction between atoms and functional groups, we might be able to come up with hosts that are highly effective and low cost.

8-4. Chemical Stability of Potential Window

The last aspect that I will discuss in future directions is also one of the most important. As we are pushing high-energy cathodes, on the one hand, we are trying every functionality in our tool box to design materials with higher and higher capacities. On the other hand, we are also exploring redox-active processes that are higher and higher in potentials vs. Li/Li^+ to increase energy density of our materials. While much progress has been made, the higher in voltage, the more likely the electrode material will undergo chemical degradation. One of the main caveat from Chapter 5 is that, we were unable to access the utilization of the highest redox couple, effectively lowering the capacity from near 200 mAh/g to 150 mAh/g. Therefore,

while we desire redox processes at high potentials, we also need to be aware of the limitations in terms of chemical stabilities of our materials and our systems.

This means that we are considering stability from two perspectives: electrode material stability and device stability. Electrode material stability is basically if your materials are stabled on its own and compatible with the device, and in most material design and primary device characterization, we will be able to assess this information. But another important criterion to consider is that, if the device is stable enough to support these redox processes. For the current lithium-ion battery solvent/electrolyte system, the upper limit of potential window is ~ 4.5 V and the use of higher potential cathode requires the use of specialty solvent/electrolyte systems or additives to stabilize them.[12] From a material design standpoint, the design of materials with redox processes near the vicinity of that upper limit potential is likely to result in compromised safety.

As concluding remarks, I have presented data and evidence showing both thin-film and bulk redox-active polymers have favourable electrochemical properties as cathode materials for EES applications. From these studies, I have been able to derive deep mechanistic insights on the polymers redox properties and behaviors leading to both their success and failure modes. As described in this closing chapter, there are still issues that need to be solved before organic electrodes can take a big leap towards practical applicability. However, as we can see, there are wide possibilities and strategies to us scientists to take these potentials into realities. The lessons that we learnt from studying these classes of materials will become the basis and fundamentals

of future designs and studies of ever better organic electrodes for EES application.

REFERENCES

1. Chiba, K.; Ohsaka, T.; Ohnuki, Y.; Oyama, N., Electrochemical preparation of a ladder polymer containing phenazine rings. *Journal of Electroanalytical Chemistry and Interfacial Electrochemistry* **1987,** *219* (1), 117-124.

2. Sawyer, D. T.; Komai, R. Y., Electrochemistry of phenazine at a platinum electrode in aprotic solvents. *Analytical Chemistry* **1972,** *44* (4), 715-721.

3. Nelson, R. F.; Leedy, D. W.; Seo, E. T.; Adams, R. N., Anodic oxidation of 5,10-dihydro-5,10-dimethylphenazine. *Fresenius' Zeitschrift für analytische Chemie* **1966,** *224* (1), 184-196.

4. Krikstopaitis, K.; Kulys, J.; Tetianec, L., Bioelectrocatalytical glucose oxidation with phenoxazine modified glucose oxidase. *Electrochemistry Communications* **2004,** *6* (4), 331-336.

5. Nowakowska-Oleksy, A.; Sołoducho, J.; Cabaj, J., Phenoxazine Based Units-Synthesis, Photophysics and Electrochemistry. *Journal of Fluorescence* **2011,** *21* (1), 169-178.

6. Kulys, J.; Krikstopaitis, K.; Scheller, F. W.; Wollenberger, U., Electrochemical Parameters of Phenoxazine Derivatives in Solution and at Monolayer-Modified Gold Electrodes. *Electroanalysis* **2004,** *16* (3), 183-189.

7. Peled, E.; Sternberg, Y.; Gorenshtein, A.; Lavi, Y., Lithium-Sulfur Battery: Evaluation of Dioxolane-Based Electrolytes. *Journal of The Electrochemical Society* **1989,** *136* (6), 1621-1625.

8. Mikhaylik, Y. V.; Akridge, J. R., Polysulfide Shuttle Study in the Li/S Battery System. *Journal of The Electrochemical Society* **2004,** *151* (11), A1969-A1976.

9. Diao, Y.; Xie, K.; Xiong, S.; Hong, X., Shuttle phenomenon – The irreversible oxidation mechanism of sulfur active material in Li–S battery. *Journal of Power Sources* **2013,** *235*, 181-186.

10. Zhang, K.; Guo, C.; Zhao, Q.; Niu, Z.; Chen, J., High-Performance Organic Lithium Batteries with an Ether-Based Electrolyte and 9,10-Anthraquinone (AQ)/CMK-3 Cathode. *Advanced Science* **2015,** *2* (5), 1500018.

11. Guo, C.; Zhang, K.; Zhao, Q.; Pei, L.; Chen, J., High-performance sodium batteries with the 9,10-anthraquinone/CMK-3 cathode and an ether-based electrolyte. *Chemical Communications* **2015,** *51* (50), 10244-10247.
12. Hu, M.; Pang, X.; Zhou, Z., Recent progress in high-voltage lithium ion batteries. *Journal of Power Sources* **2013,** *237*, 229-242.